OCEAN ENGINEERING GROUP

Numerical Techniques for the Design and Prediction of Performance of Marine Turbines and Propellers

Wei Xu

August 2010

REPORT No.

10-06

ENVIRONMENTAL AND WATER RESOURCES ENGINEERING
DEPARTMENT OF CIVIL, ARCHITECTURAL AND ENVIRONMENTAL ENG.
THE UNIVERSITY OF TEXAS AT AUSTIN
AUSTIN, TX 78712

This report consists an enhanced version of the MS Thesis of Wei Xu, Ocean Engineering Group, The University of Texas at Austin, August 2010.

In particular, the results and content of Chapter 5 have been considerably improved.

The Thesis Committee for Wei Xu
Certifies that this is the approved version of the following thesis:

Numerical Techniques for the Design and Prediction of Performance of Marine Turbines and Propellers

APPROVED BY
SUPERVISING COMMITTEE:

Supervisor: ______________________________
Spyros A. Kinnas

Reader: ______________________________
Lance Manuel

Numerical Techniques for the Design and Prediction of Performance of Marine Turbines and Propellers

by

Wei Xu, B.S.

Thesis

Presented to the Faculty of the Graduate School of
The University of Texas at Austin
in Partial Fulfillment
of the Requirements
for the Degree of

Master of Science in Engineering

The University of Texas at Austin
August 2010

Dedicated to my parents and my sister

Acknowledgements

Although this thesis bears my name, it would not have been possible to complete this work without the guidance and encouragement of many individuals. First and foremost, I would like to express my greatest appreciation and gratefulness to my advisor, Professor Spyros A. Kinnas. Over the last two years, he has been a thoughtful teacher on my research and a patient mentor on my life.

I would also like to express my deepest gratitude to Dr. Vimal Vinayan and Dr. Yi-Hsiang Yu for their invaluable advice and endless support. I am also indebted to Mr. Lei He, Mr. Shu-hao Chang and all other members in our lab.

A special thanks goes to Professor Yin Lu Young, Professor Kinnas's former student, who provided me with a turbine geometry for my research.

I would also like to thank all my friends at UT Austin for their friendship and assistance.

Finally, I would like to thank Phase V Members of the "Consortium on Cavitation Performance of High Speed Propulsors" for their support on the part of my research that relates to propulsors. The consortium includes the following members : American Bureau of Shipping, Daewoo Shipbuilding and Marine Engineering Co. Ltd., Kawasaki Heavy Industry Ltd., Rolls-Royce Marine AB, Rolls-Royce Marine AS, Samsung Heavy Industries Co. Ltd., SSPA AB, Andritz Hydro GmbH, Wärtsilä Propulsion Netherlands B.V., Wärtsilä Propulsion Norway AS, Wärtsilä Lips Defense S.A.S., and Wärtsilä CME Zhenjiang Propeller Co. Ltd.

Numerical Techniques for the Design and Prediction of Performance of Marine Turbines and Propellers

by

Wei Xu, M.S.E.

The University of Texas at Austin, 2010

Supervisor: Spyros A. Kinnas

The performance of a horizontal axis marine current turbine is predicted by three numerical methods, vortex lattice method MPUF-3A, boundary element method PROPCAV and a commercial RANS solver FLUENT. The predictions are compared with the experimental measurements for the same turbine model. A fully unsteady wake alignment is utilized in order to model the realistic wake geometry of the turbine. A lifting line theory based method is developed to produce the optimum circulation distribution for turbines and propellers and a lifting line theory based database searching method is used to achieve the optimum circulation distribution for tidal turbines. A nonlinear optimization method (CAVOPT-3D) and another database-searching design method (CAVOPT-BASE) are utilized to design the blades of marine current turbines and marine propellers.

A design procedure for the tidal turbine is proposed by using the developed methods successively. Finally, an interactive viscous/potential flow method is utilized to analyze the effect of nonuniform inflow on the performance of tidal turbines.

Table of Contents

List of Tables xi

List of Figures xii

Nomenclature xvii

Chapter 1 Introduction 1
- 1.1 Fossil energy and renewable Energy 1
- 1.2 Tidal energy 2
- 1.3 Tidal turbines 4
- 1.4 Propellers and turbines..8
- 1.5 Objective 9
- 1.6 Organization..9

Chapter 2 Literature Review 11
- 2.1 VLM and BEM 11
  - 2.1.1 Vortex-lattice method 11
  - 2.1.2 Boundary element method 12
- 2.2 Propeller design method 13
- 2.3 Performance prediction and design of tidal turbines 13

Chapter 3 Methodology 16
- 3.1 Actuator Disk Theory 16
- 3.2 Lifting line theory 18
  - 3.2.1 Lifting line theory based optimization (LLOPT)........................18
  - 3.2.2 Circulation database searching method (LLOPT-BASE)...........22
  - 3.2.3 Generation of base blade geometry based on the optimum circulation distribution 23
- 3.3 Vortex Lattice Method (VLM) 23
  - 3.3.1 Blade Geometry 24
  - 3.3.2 Unsteady wake alignment 26
- 3.4 Boundary Element Method (BEM)..28

3.5 NS-3D and FLUENT 30
    3.5.1 Introduction to NS-3D 30
    3.5.2 Introduction to FLUENT 32
3.6 Database-searching method (CAVOPT-BASE) 33
3.7 Nonlinear optimization method (CAVOPT-3D) 35
    3.7.1 B-spline blade geometry 35
    3.7.2 Design method 36

Chapter 4 Results for Turbines 40
4.1 Optimum circulation distribution..40
    4.1.1 Single turbine 40
    4.1.2 Contra-rotating turbine...44
        4.1.2.1 Comparison between a single turbine and a contra-rotating turbine 44
        4.1.2.2 Convergence analysis of tanβ_i 46
        4.1.2.3 Efficiencies of a contra-rotating turbine for different Tip Speed Ratios...48
        4.1.2.4 Analysis of the Ratio of TSR between two components 50
4.2 Hydrodynamic Analysis of marine current turbines 51
    4.2.1 The experiment 51
    4.2.2 Performance predictions and wake geometries..........................54
        4.2.2.1 Predictions of performance and wake geometry for the 0 yaw angle turbine-uniform inflow 54
        4.2.2.2 Predictions of performance and wake geometry for the turbine with non-zero yaw angle.......................................68
        4.2.2.3 Prediction of cavitation for the 0 yaw angle turbine-uniform inflow 72
    4.2.3 Marine current turbine subject to non-uniform current 74
4.3 Examples of Blade Design for turbines 79
    4.3.1 Database-searching method (CAVOPT-BASE) 79
        4.3.1.1 Fully wetted turbine design..80
        4.3.1.2 Cavitating turbine design 81

4.3.2 Nonlinear optimization method (CAVOPT-3D) 85

4.3.3 The complete design procedure 90

4.3.3.1 Determining the optimum circulation distribution 91

4.3.3.2 Generation of base geometry 91

4.3.3.3 Geometry refinement by CAVOPT-BASE.....................94

Chapter 5 Results of Design Methods for Propellers..96

5.1 Optimum circulation distribution..96

5.2 Application of CAVOPT-BASE to propellers..98

5.2.1 Fully wetted case...99

5.2.1 Fully wetted at lower cavitation number 102

5.3 Application of CAVOPT-3D to propellers 105

5.3.1 Non-skewed propeller design 106

5.3.2 Skewed propeller design 113

Chapter 6 Conclusions and Recommendations...125

6.1 Conclusions...125

6.2 Recommendations...127

Appendix A Influence coefficients for the lifting line theory...........................129

Appendix B Lifting line optimization method for contra-rotating turbines 132

B.1 Optimum method for a contra-rotating turbine 132

B.2 Procedures of circulation distribution calculation for a contra-rotating turbine 135

Appendix C Data for the section that is used in the design procedure 137

References..139

Vita 143

List of Tables

Table 4.1 Parameters and results for a single turbine and two components (front and back) of a contra-rotating turbine 45
Table 4.2 Efficiencies of the contra-rotating turbine for different *TSR*s (3 blades and 0.2 hub radius) 48
Table 4.3 Efficiencies of the contra-rotating turbine for different *TSR* ratios (Z=3 and $\delta=0.1R$) 51
Table 4.4 Chord, pitch and thickness distribution for the blade of the marine current turbine (source:(Bahaj, Molland, et al., 2007)) 53
Table 4.4 Three design cases by CAVOPT-BASE 85
Table 5.1 Efficiencies with different discretization number (*m*) at different *J* 97
Table 5.2 Two design cases by CAVOPT-BASE (for propellers) 105
Table 5.3 Four propeller design cases by CAVOPT-3D coupled with MPUF-3A (v3.0) 124

List of Figures

Fig. 1.1 Aerial view of the La Rance Tidal Power Plant (Source: Electricite de France) .. 4
Fig. 1.2 A typical 3-blade wind turbine (source:http://owensoundbeat.files.wordpress.com/2010/03/wind-turbine.jpg) 5
Fig 1.3 Two horizontal axis tidal turbines in New York's East River for Verdant Power's prototype tidal energy project (source: http://www.ens-newswire.com/ens/apr2009/20090409_tidalturbines.jpg) 6
Fig. 1.4 a model of vertical axis tidal turbine 7
(Source:http://www.esru.strath.ac.uk/EandE/Web_sites/0506/marine_renewables/technology/assets/VAMCT.jpg) 7
Fig. 1.5 2.5m diameter contra-rotating tidal turbine (Source: (Clarke, Connor, Grant, Johnstone, & Ordonez-Sanchez, 2008)) 8
Fig. 3.1 Actuator disk, stream-tube and the variation of velocities. 16
Fig. 3.2 Combined velocity and force diagram on blade section at radius r for turbines . 18
Fig. 3.3 Algorithm of lifting line optimization method (LLOPT) 21
Fig. 3.4 Coordinate systems and geometrical notations in VLM (MPUF-3A), from (Greeley & Kerwin, 1982) 25
Fig. 3.5 Schematic diagram of the calculation of the induced velocity, from (L. He, 2010). The left part is the blade and the right part is the wake. 27
Fig. 3.6 Turbine subject to a general inflow. (Note: x, y, z is a system of coordinates which rotates with the turbine and x_s, y_s and z_s is the inertial system of coordinates, also called the "ship fixed system" in the case of propellers) 29
Fig. 3.7 Procedure of the viscous/potential flow method 31
Fig. 3.8 Rotationally periodic boundary (source: FLUENT manual) 33
Fig. 3.9 Cubic B-spline surface. 4×4 vertex polygon net and 10×9 grid blade surface in MPUF-3A, from (Mishima & Kinnas, 1996) 36
Fig. 3.10 Initial B-spline polygon vertices, design variables, and vertex movement (4×4 vertices), from (Mishima & Kinnas, 1996)... 37
Fig. 4.1 Convergence history for tanβ_i of the single turbine design via LLOPT 41
Fig. 4.2. Circulation distributions from LLOPT and LLOPT-BASE for a 3-blade turbine 41
Fig. 4.3 Efficiency contour plot from LLOPT-BASE (3-blade turbine; *J*=0.5236) 42
Fig. 4.4 Comparison of the efficiency from LLOPT and LLOPT-BASE for different Z and *J* 43
Fig. 4.5 Comparison of the axial induced velocity from LLOPT and LLOPT-BASE and actuator disk theory 43
Fig. 4.6 Optimum circulation distribution for both single turbine and contra-rotating turbine (Note: the direction of Γ for the back turbine is opposite to that of the front. In this figure, both of them are plotted positive) 46

Fig. 4.7 Convergence history for tanβ_i of the front turbine for the contra-rotating turbine 47
Fig. 4.8 Convergence history for tanβ_i of the back turbine for the contra-rotating turbine 48
Fig. 4.9 Total efficiencies of a contra-rotating turbine for different Advance Ratios (J) . 50
Fig. 4.10 Cavitation tunnel with a marine current turbine, from (Bahaj, Molland, et al., 2007). 52
Fig. 4.11 Photograph of the blade and hub component (source: (Bahaj, Molland, et al., 2007)) 53
Fig. 4.12 Blade geometry modeled by boundary element method 55
Fig. 4.13 First 4 blade sections from the boundary element method 56
Fig. 4.14 Geometry and mesh of the fluid domain in the FLUENT. 57
Fig. 4.15 Geometry and mesh of the turbine blade in FLUENT (Notice that the root part of the blade in the FLUENT is extended (to the hub) for 0.02R with decreasing chord length and thickness distributions) 58
Fig. 4.16 Comparison of thrust coefficient (*CT*) from different numerical methods with the experimental measurements 59
Fig. 4.17 Comparison of power coefficient (Cpow) from different numerical methods with the experimental measurements 60
Fig. 4.18 Wake geometry from BEM using blade pitch wake alignment (*TSR*=6.0) 61
Fig. 4.19 Converged wake geometry from VLM using unsteady wake alignment (*TSR*=6.0). 62
Fig. 4.20 y-z view of the final converged wake geometry from VLM using unsteady wake alignment (*TSR*=6.0). 63
Fig. 4.21 Wake geometry from FLUENT (visualized by streamlines) 64
Fig. 4.22 A Tip streamline from FLUENT viewed in a *y-z* plane (wake expansion effect) 65
Fig. 4.23 Streamlines around the tip part viewed in a *y-z* plane (tip roll up phenomenon is observed) 65
Fig. 4.24 Comparison of Pressure coefficients (C_p) at Y=0.3 between FLUENT and PROPCAV (*TSR*=6.0, 25^0 hub pitch and 0^0 yaw angle). 66
Fig. 4.25 Comparison of Pressure coefficients (C_p) at Y=0.5 between FLUENT and PROPCAV (*TSR*=6.0, 25^0 hub pitch and 0^0 yaw angle). 67
Fig. 4.26 Comparison of Pressure coefficients (C_p) at Y=0.8 between FLUENT and PROPCAV (*TSR*=6.0, 25^0 hub pitch and 0^0 yaw angle). 67
Fig. 4.27 Definition of yaw angle for the marine current turbine 69
Fig. 4.28 Comparison of thrust coefficient (*CT*) from MPUF-3A at different inflow yaw angles (15^0 and 30^0) with the experimental measurements 69
Fig. 4.29 Comparison of thrust coefficient (C_{pow}) from MPUF-3A at different inflow yaw angles (15^0 and 30^0) with the experimental measurements 70
Fig. 4.30 Final converged wake geometry in yz plane for 15^0 yaw angle 71
Fig. 4.31 Final converged wake geometry in xz plane with 15^0 yaw angle 72

Fig. 4.32 The cavity pattern of the model turbine in the experiment (TSR=7.5 and σ_n=3.9), from (Bahaj, Molland, et al., 2007) 73
Fig. 4.33 Pressure contour and cavity patterns for a same turbine (TSR=7.5 and σ_n=3.9) 74
Fig. 4.34 Tidal profile and location of turbine in NS-3D 75
Fig. 4.35 Mesh of the computational domain of NS-3D 76
Fig. 4.36 Inflow velocity contour (x=-5.0) 76
Fig. 4.37 Effective wake axial velocity contour (x=-0.1R) (The circumferential and radial views of the grid are also shown) 77
Fig. 4.38 Total axial velocity contour and grid at xy-plane when z=0 (the turbine is located at x=0) 77
Fig. 4.39 Comparison of the effective mean velocity with the nominal mean velocity ... 78
Fig. 4.40 Comparison of C_{pow} between uniform velocity case and tidal velocity case 78
Fig. 4.41 Pressure distribution of the original cavitation case at different radii for Cavitating Case 1, σ_n=5. 82
Fig. 4.42 Pressure distribution of the design turbine at different radii for Cavitating Case 1 82
Fig. 4.43 Projected Blade geometry and cavity patterns at various angular positions for the original turbine (Cavitating Case 2) 83
Fig. 4.44 Projected Blade geometry and cavity patterns at various angular positions for the design turbine (Cavitating Case 2) 84
Fig. 4.45 4×4 vertex polygon net for the B-spline turbine geometry 86
Fig. 4.46 Initial turbine geometry (utilized in CAVOPT-3D) 87
Fig. 4.47 Designed projected turbine geometry from CAVOPT-3D 88
Fig. 4.48 Designed pitch (P/D), chord (c/D) and camber (f/c) distributions for the designed turbine 89
Fig. 4.49 Convergence history for the design of turbine 89
Fig. 4.50 Flow chart of design procedure 91
Fig. 4.51 Comparison of the circulation distribution form MPUF-3A and LLOPT-BASE 93
Fig. 4.52 Power coefficient (inviscid) for the base turbine over a range of TSR. 93
Fig. 4.53 Comparison of the section profiles at r=0.2R 95
Fig. 5.1 Distribution of circulation with different advance ratio J when C_T=0.512, should be compared directly with Fig. 45 of (J. E. Kerwin, 2001). Note: IR_NORM is the normalized circulation, which has same definition as $\overline{\Gamma}$) 97
Fig. 5.2 Variation of propeller efficiency with advance ratio J (m=10 & m=100), should be compared with Fig. 46 of (J. E. Kerwin, 2001) 98
Fig. 5.3 Initial geometry for the propeller design in CAVOPT-BASE 100
Fig. 5.4 Pressure distributions at different radii for the base geometry of turbine subject to uniform inflow 101
Fig. 5.5 Design geometry of propeller for the fully wetted case 101
Fig. 5.6 Pressure distribution at different radii for the propeller geometry designed by CAVOPT-BASE, subject to uniform inflow. 102

Fig. 5.7 Pressure distribution at different radii for the initial geometry of propeller in the fully wetted case at low cavitation number (σ_n=2.5). 103
Fig. 5.8 Initial blade geometry of propeller and the corresponding cavity patterns for the fully wetted case at low cavitation number (σ_n=2.5). 104
Fig. 5.9 Pressure distribution at different radii for the propeller geometry designed by CAVOPT-BASE. 104
Fig. 5.10 Designed projected blade geometry and cavity pattern at different time steps for the cavitating case (uniform inflow, 0 skew, CA≤0.3) 108
Fig. 5.11 Designed pitch (P/D), chord (c/D) and maximum camber (f/c) distributions for the cavitating case (uniform inflow, 0 skew, CA≤0.3) 109
Fig. 5.12 Convergence history for the cavitating case (uniform inflow, 0 skew, CA≤0.3) 110
Fig. 5.13 Velocity contour of the non-uniform inflow 110
Fig. 5.14 Designed projected blade geometry and cavity pattern at different time steps for the cavitating case (non-uniform inflow, 0 skew, CA≤0.3).................................. 111
Fig. 5.15 Designed pitch (*P*/*D*), chord (*c*/*D*) and maximum camber (*f*/*c*) distributions for the cavitating case (non-uniform inflow, 0 skew, CA≤0.3).................................. 112
Fig. 5.16 Convergence history for the cavitating case (non-uniform inflow, 0 skew, CA≤0.3) 113
Fig. 5.17 Converged key blade geometry and trailing wake for the skewed propeller design (uniform inflow, K_T=0.35, CA≤0.3) 115
Fig. 5.18 Designed projected blade geometry and cavity patterns at different time steps for the cavitating skewed propeller case (Uniform inflow, K_T=0.35, CA≤0.3) 116
Fig. 5.19 Designed pitch (*P*/*D*), chord (*c*/*D*) and maximum camber (*f*/*c*) distributions for the cavitating skewed propeller. (Uniform inflow, K_T=0.35, CA≤0.3).................. 117
Fig. 5.20 Convergence history for the design of a cavitating skewed propeller by using CAVOPT-3D coupled with MPUF-3A (v3.0) (Uniform inflow, K_T=0.35, CA≤0.3) 117
Fig. 5.21 Designed projected blade geometry and cavity patterns at different time steps for the cavitating skewed propeller case (Non-uniform inflow, K_T=0.35, CA≤0.3)118
Fig. 5.22 Designed pitch (*P*/*D*), chord (*c*/*D*) and maximum camber (*f*/*c*) distributions for the cavitating skewed propeller. (Non-uniform inflow, K_T=0.35, CA≤0.3) 119
Fig. 5.23 Convergence history for the design of a cavitating skewed propeller by using CAVOPT-3D coupled with MPUF-3A (v3.0) (Non-uniform inflow, K_T=0.35, CA≤0.3) 119
Fig. 5.24 Designed projected blade geometry and cavity patterns at different time steps for the cavitating skewed propeller with high CA (Uniform inflow, K_T=0.35, CA≤0.6) 120
Fig. 5.25 Designed pitch (*P*/*D*), chord (*c*/*D*) and maximum camber (*f*/*c*) distributions for the cavitating skewed propeller. (Uniform inflow, K_T=0.35, CA≤0.6).................. 121

Fig. 5.26 Convergence history for the design of a cavitating skewed propeller by using CAVOPT-3D coupled with MPUF-3A (v3.0) (Uniform inflow, K_T=0.35, CA≤0.6) 121
Fig. 5.27 Designed projected blade geometry and cavity patterns at different time steps for the cavitating skewed propeller with high CA (Non-uniform inflow, K_T=0.35, CA≤0.6) 122
Fig. 5.28 Designed pitch (*P*/*D*), chord (*c*/*D*) and maximum camber (*f*/*c*) distributions for the cavitating skewed propeller. (Non-uniform inflow, K_T=0.35, CA≤0.6) 123
Fig. 5.29 Convergence history for the design of a cavitating skewed propeller by using CAVOPT-3D coupled with MPUF-3A (v3.0) (Non-uniform inflow, K_T=0.35, CA≤0.6) 124
Fig. A.1 Discritized vortex horseshoes of the wake for the key blade 130
Fig. B.1 Combined velocity and force diagram for a component of a contra-rotating turbine 133
Fig. C.1 Data for NACA Mean Line a=0.8 137
Fig .C.2 NACA Mean Line a=0.8 camber form 138

Nomenclature

Latin Symbols

A	turbine sweep area, $A=\pi R^2$
A_d	area of the actuator disk, $A=\pi R^2$
c	blade chord length
C_{DV}	sectional drag coefficient
C_pow	power coefficient, $C_{pow}=Q\omega/0.5\rho V^3A$
C_p	pressure coefficient, $C_p=(p\text{-}p_0)/\rho n^2D^2$ for MPUF-3A, $C_p=(p\text{-}p_0)/0.5/\rho n^2D^2$ for PROPCAV
C_{Pmin}	maximum negative C_p, $C_{Pmin}=max(-C_p)$
C_L	lift coefficient
CT	thrust coefficient in MPUF-3A and BEM, $CT=T/0.5\rho V^2A$
C_T	thrust coefficient in lifting line theory, $C_T=2T/(\rho V^2A_0)$
$CPMIN$	maximum allowed C_{Pmin}
$d_\mathrm{i,j}$	B-spline control points
D	turbine diameter
f	camber (in CAVOPT-3D, it is an objective function)
f_max	sectional maximum camber
f_0	ideal maximum camber
Fr	Froude number, $Fr=n^2D/\mathrm{g}$
g	linear function for adjusting the circulation distribution
g_i	inequality constraints in CAVOPT-3D
h	value of function $g(x,k,h)$ when $x=0.5(R\text{-}r_h)$
h_i	equality constraints in CAVOPT-3D

h_1, h_2	lower and upper bounds for h
J	advance ratio ($J = V/nD$)
k	slope of the linear function g
k_1, k_2	lower and upper bounds for k
K_T	thrust coefficient, $K_T = T/\rho n^2 D^4$
K_Q	torque coefficient, $K_Q = Q/\rho n^2 D^2$
K_{T0}	design thrust coefficient in CAVOPT-3D
L	lift force
M	discretization number for one blade in lifting line theory
$N_{\mathrm{i},4}$	B-spline basis of order 4
N_{u}	B-spline control points in *u*-direction
N_{w}	number of B-spline control points in *w*-direction
n	rotational frequency
P	pitch
p_0	far upstream pressure
Q	turbine or propeller torque
Q_B	magnitude of line sources representing blade thickness
Q_C	magnitude of line sources representing cavity thickness
r_h	hub radius
$\overline{r}_m$	nondimensional radius of section m
R	radius of tidal turbine (m)
Re	Reynolds number, $Re = VD/\nu$
t	blade thickness
T	turbine or propeller thrust
TSR	tip speed ratio, $TSR = \omega R/V = \pi/J$

$\boldsymbol{v}_{\Gamma}$	velocity vectors induced by unit strength of line source
$\boldsymbol{v}_{Q}$	velocity vectors induced by unit strength of vortex loop
V	current speed (m/s)
V^{*}	total inflow velocity (m/s)
u_a^{*}	axial turbine-induced velocity (m/s)
u_t^{*}	tangential turbine-induced velocity (m/s)
$\bar{u}_a$	axial vortex-horseshoe-induced velocity (m/s)
$\boldsymbol{U}_w$	non-axisymmetric inflow in BEM
U_{in}	total inflow velocity in BEM
x_m	rake
x, y, z	turbine or propeller fixed coordinates
x_s, y_s, z_s	inertial system of coordinates or ship fixed coordinates
Z	blades number

Greek Symbols

α_0	ideal angle of attack
β	initial inclined angle, $\tan\beta = V/\omega R$
β_i	inclined angle including the induced velocity $\tan\beta_i = (V - u_a^*)/(\omega R + u_t^*)$
η	turbine efficiency, same definition as C_{pow}
σ_n	cavitation number, $\sigma_n = (p_0 - p_v)/(0.5\rho n^2 D^2)$
θ	skew
ϕ	pitch angle in the definition of turbine geometry
ϕ_p	potential at point p
$\Delta\phi_w$	potential jump across the wake surface
ε	tolerance for the convergence of optimum circulation
Δr	radius interval in the lifting line theory
$\Delta\bar{r}$	nondimensional radius interval in the lifting line theory
ρ	current density
ω	turbine or propeller angular velocity
ν	kinematic viscosity of water
Γ	Circulation
Γ_m	sectional circulation, at section m
$\bar{\Gamma}_m$	Non-dimensional circulation, at section m
$\boldsymbol{\Gamma_B}$	constant strength of bound vortex
$\boldsymbol{\Gamma_W}$	constant strength of free shed vortex

Acronyms

BEM	boundary element method
VLM	vortex-lattice method
NACA	National Advisory Committee for Aeronautics

Computer Program Names

MPUF-3A	cavitating propeller potential flow solver based on VLM
PROPCAV	cavitating propeller potential flow solver based on BEM
NS-3D	finite volume method based viscous flow solver
LLOPT	lifting line theory based optimization
LLOPT-BASE	circulation database searching method
CAVOPT-BASE	database-searching method for the design of propeller
CAVOPT-3D	nonlinear optimization method for propeller design

Chapter 1

Introduction

1.1 FOSSIL ENERGY AND RENEWABLE ENERGY

Fossil fuels or mineral fuels are energy sources such as coal, oil and natural gas, which are derived from living matter that existed in the early stages of the previous geologic time period. Almost 85% of the energy we use today comes from fossil fuels. Actually it would take millions of years to completely restore the fossil fuels that we have used in a few thousand. With levels of these fuels constantly decreasing and pollution due to the usage of fossil fuels gradually increasing, we should act now to become less dependent on fossil fuels.

While fossil fuel power systems and nuclear reactors continue to cause considerable environmental problems, clean renewable energy sources have offered a more efficient alternative to generate electricity, thus have become a great magnet for scientists and engineers. Renewable energy is any natural source that can replenish itself automatically over a comparatively short period of time. Renewable energy comes from common resources such as wind, wave and water current, solar power, and geothermal energy. Wind has become the fastest growing renewable energy technology in the past decades. It is generally considered the most economical source of renewable energy and, under certain circumstances, cheaper than fossil-fuel-produced electricity. According to the statistics from the Community Environmental Council, good sites of wind farms can produce wind power at eight to ten cents per kilowatt-hour (kWh), in comparison to the cost of electricity from a new natural gas plant in California is ten to eleven cents per kWh. The ocean is another resource that shows potential for developing renewable energy. Covering 70% of the earth surface, ocean is the largest solar collector that holds tremendous energies, a small portion of which would be able to cover the energy need of the entire world. There are two types of ocean energy: the thermal energy from the sun's heat and the mechanical energy from the waves and water currents. The sun's heat warms the surface of the ocean, resulting in temperature difference between deep and shallow waters, which creates the thermal energy. The thermal energy is utilized by converting fluid into steam, which could drive generator-connected turbines to produce electricity. Mechanical ocean energy is quite different from the thermal energy. Collecting of ocean mechanical energy involves mechanical devices. There are three systems which can convert the wave energy to electricity: float systems that drive hydraulic pumps, channel systems that funnel the waves into reservoirs and oscillating water column systems that use the waves to compress air within a container. Tidal current is one type of water current that can be exploited for electricity. Tides are the rise and fall of sea levels caused by the combined effects of the rotation of the earth and the gravitational forces exerted by the moon and the sun. The tides occur at an interval of approximately 12 and half hours, so it is more predictable than wind, which highly depends on the weather.

1.2 TIDAL ENERGY

People took advantage of the phenomenon of tides and tidal current long before the Christian era. Small tidal hydro-mechanical devices were built then to pump water, make watermills and for other applications while large tidal waterwheels weren't invented until recent times. For example, large waterwheels were employed to pump sewage in Hamburg and Germany in the nineteenth century. Capable of generating electricity by forcing tidal current through turbines, barrage, or dam represents an important conventional device that collects and converts tidal energy. Built in 1966, the largest tidal power station in the world (and the only one in Europe) is in the Rance estuary in northern France, near St. Malo (Fig. 1.1).

Tidal energy, like wind and solar energies, is distributed across large areas, and therefore is difficult to collect. The conventional tidal power devices, including massive dams in the open ocean, are inefficient, complicated and very expensive for low-head tidal power application. Besides, dams may block fish migration, and ultimately result in drastic fish population decline.

Due to the aforementioned environmental and economic concerns, scientists and engineers are compelled to create an alternative device to massive dams for tidal energy collecting and converting. The new device is an unconventional propeller-like tidal turbine that can efficiently extract the kinetic energy from the tidal currents. Some types of turbines will be described in the next section.

Fig. 1.1 Aerial view of the La Rance Tidal Power Plant (Source: Electricite de France)

1.3 TIDAL TURBINES

Around the world, wind turbines with various sizes have become a familiar sight (Fig. 1.2). Their purpose is to collect energy from wind currents. A wind turbine resembles its forerunner windmill in appearance, yet, windmills are typically used to directly power machinery such as a pump or a grinder for grain. Due to the cost reduction of installation and progressive government policies, wind turbine industry has become a key component of the power production industry in the world.

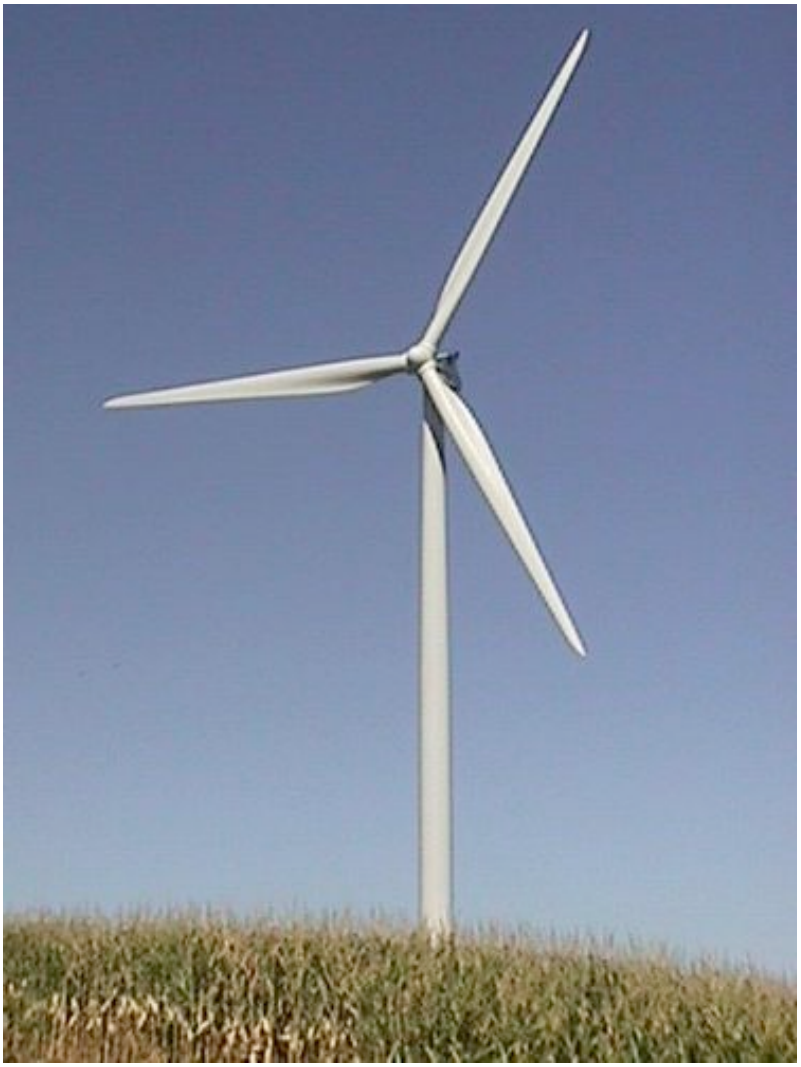

Fig. 1.2 A typical 3-blade wind turbine
(source:http://owensoundbeat.files.wordpress.com/2010/03/wind-turbine.jpg)

A tidal turbine acts underwater in a very similar way to a wind turbine operates in the air. Instead of extracting energy from the air, a tidal turbine could collect kinetic energy from the water, which is some 800 times denser than air, and so even slow moving tides can carry significantly larger energy than wind. Therefore, a tidal turbine has smaller diameter than a wind turbine of the same power output, resulting in lower cost of manufacture and transportation. Furthermore, it is believed that environmental impact of tidal turbines is negligible due to their slow rotation rates of only 10-30 revolutions per minute (10 times slower than that of ship's propellers). Nowadays, many tidal turbines are being tested around the world, such that the New York tidal turbine project, which has undertaken the construction of a $20 million 200-300 turbine 10MW tidal turbine farm in the East River.

As mentioned in the previous section, there are generally two types of tidal turbines, the horizontal axis tidal turbine and the vertical axis tidal turbine, which are shown in Fig.1.3 and Fig. 1.4, respectively.

Fig 1.3 Two horizontal axis tidal turbines in New York's East River for Verdant Power's prototype tidal energy project (source: http://www.ens-newswire.com/ens/apr2009/20090409_tidalturbines.jpg)

In Fig. 1.3, the horizontal axis tidal turbines have almost identical geometry as that of wind turbines, except that they are in smaller size. The tidal current drives the turbine blades to rotate, which can in turn feed a generator kinetic energy to produce electricity. The vertical axis turbine differs from the horizontal axis turbine in an obvious way - its blades are attached to a central vertical shaft rather than a horizontal one. Vertical axis turbines tend to be easier to build and transport and safer to operate. However, they have a low torque and they take twice the time to produce efficient energy from tides. The decision of which type to choose in a turbine farm project depends on the tidal current velocity and the topography of the site. The main factor that confines the development of the tidal turbine industry is the cost of maintaining tidal turbines is relatively higher than that for having wind turbines.

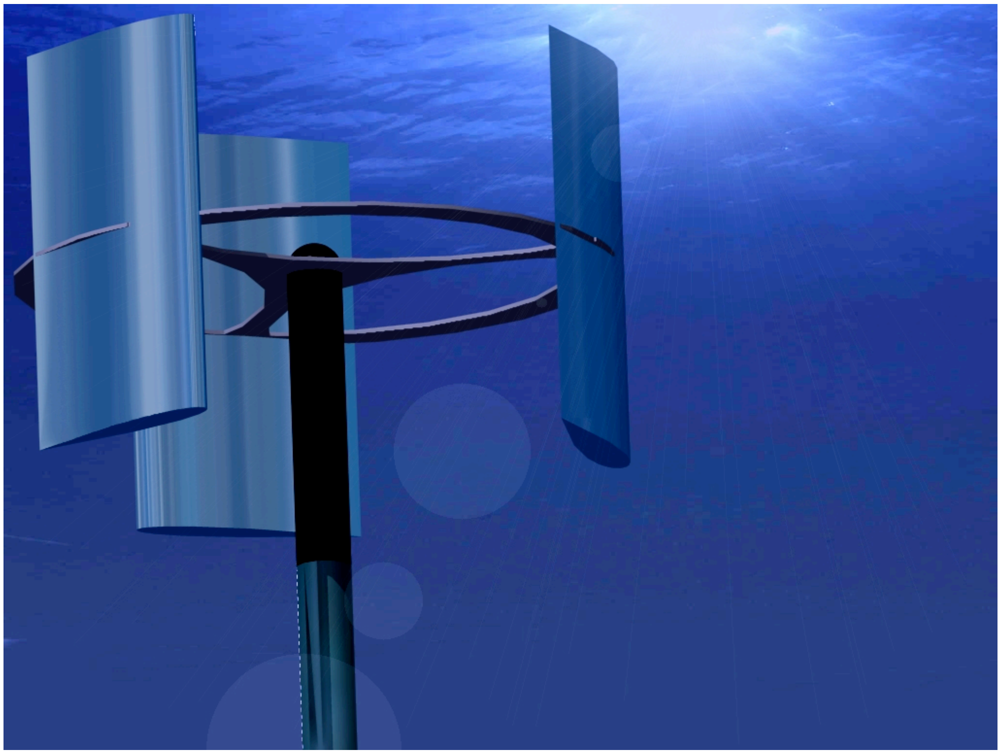

Fig. 1.4 a model of vertical axis tidal turbine
(Source:http://www.esru.strath.ac.uk/EandE/Web_sites/0506/marine_renewables/technology/assets/VAMCT.jpg)

For the horizontal axis tidal turbines, some particular types, such as contra-rotating tidal turbines and ducted tidal turbines, have been developed in order to increase the produced power. The contra-rotating turbine works in a similar way as a contra-rotating propeller, which consists of a front and a back propeller components. The idea of ducted turbines comes from the ducted propellers, which could improve the efficiency by confining the passing water current. A photo of a contra-rotating turbine is shown in Fig. 1.5.

Fig. 1.5 2.5m diameter contra-rotating tidal turbine (Source: (Clarke, Connor, Grant, Johnstone, & Ordonez-Sanchez, 2008))

1.4 PROPELLERS AND TURBINES

The horizontal axis tidal turbine looks similar to an underwater propeller, which transmits engine power by converting rotational motion into propulsive force (thrust), thus the propeller can generate kinetic energy from electrical or mechanical energy while the turbine converts kinetic energy into electricity. Almost all the principles and methods that work for propellers can be applied to turbines. This research is based on the work of propeller analysis and design in the Ocean Engineering Group at The University of Texas at Austin.

In regard to underwater propellers and turbines, cavitation can have a significant effect on their operating performance. Cavitation is defined as the formation of vapor regions inside of a flowing liquid due to a decrease in the local pressure, which is due to an increase of velocity. Cavitation is undesirable because it may cause extensive erosion to the rotating blades. In addition, extra noise and significant efficiency reduction may occur due to cavitation.

1.5 OBJECTIVE

The objective of this research is to develop computational methods to design more efficient horizontal axis tidal turbines, which can increase the output power, as well as reduce or eliminate cavitation. The turbine performance prediction tools, which include a vortex lattice method, a boundary element method and a commercial RANS solver are applied first, and some of them are utilized in the turbine design process. The same design methods are also used to design propellers in order to minimize the torque and to eliminate or reduce the cavitation for a specific thrust coefficient.

1.6 ORGANIZATION

This thesis is organized into six parts: introduction (Chapter 1), literature review (Chapter 2), methodology (Chapter 3), results for turbines (Chapter 4), results for propellers (Chapter 5), and conclusions and recommendations (Chapter 6). A review of previous analysis and design methods for both propellers and turbines is presented in Chapter 2. In Chapter 3, all methods that are used in this research are introduced. The results from the application of the methods are shown in Chapter 4 (for turbines) and

Chapter 5 (for propellers). Finally, the overall conclusions and recommendations for future work are presented in Chapter 6.

Chapter 2

Literature Review

A Vortex Lattice Method (VLM), a Boundary Element Method (BEM), and a commercial Reynolds-Averaged Navier-Stokes(RANS) solver are used to analyze the performance of tidal turbines in this research. Two lifting line optimization methods (LLOPT and LLOPT-BASE), a database-searching method (CAVOPT-BASE) and a nonlinear optimization method (CAVOPT-3D) are utilized to design turbine geometries. The first section of this chapter discusses work done in the past on the development of VLM and BEM. Section 2.2 introduces the development of two design methods for turbine blades. The final section reviews the work done for the design and analysis of tidal turbines.

2.1 VLM AND BEM

2.1.1 Vortex-lattice method

A vortex-lattice method was introduced for the analysis of fully wetted propeller flows by (J.E. Kerwin & Lee, 1978). The method was extended later to treat unsteady sheet cavitating flows by (C. S. Lee, 1979) and (Breslin, Van Houten, Kerwin, & Johnsson, 1982). The code name was PUF-3. In (Kinnas & Fine, 1989), a robust arrangement of singularities and control point spacing was employed to produce accurate results. In order to account for the defect of linear cavity solution near a round leading edge, a leading edge correction was incorporated into the VLM (Kinnas, 1991). The corresponding code name became PUF-3A. The thickness-loading coupling (Kinnas, 1992) was also included to improve the results of linear theory. Then, the method was extended to analyze the super-cavitating propellers subject to steady flow by (Kudo & Kinnas, 1995). After implementing the ability of searching for the mid-chord cavitation (Kinnas, Griffin, Choi, & Kosal, 1998), the name of the VLM-based code was renamed from PUF-3A to MPUF-3A. In (Kinnas & Pyo, 1999), the effect of hub and wake alignment, including the effect of shaft inclination, was added into MPUF-3A. Most recently, the unsteady wake alignment was developed in order to determine the accurate location of the wake (L. He, 2010; L. He & Kinnas, 2009).

2.1.2 Boundary element method

Boundary element method has been proved to be very effective in solving potential flows around propellers. (J. E. Kerwin, Kinnas, Lee, & Shih, 1987; J.-T. Lee, 1987) introduced a perturbation potential based panel method for the analysis of non-cavitating propeller performance in steady flows. Then, several BEM cavitation models were developed by (N. E. Fine & Kinnas, 1993; Kinnas & Fine, 1993; Kinnas & Hsin, 1992), which could analyze flows around cavitating hydrofoils and cavitating propellers. This method was named as PROPCAV. After that, (Young & Kinnas, 2003) introduced a method to work for supercavitating and surface-piecing propellers. (H. S. Lee & Kinnas, 2005a) included the tunnel effects in PROPCAV and (H. S. Lee & Kinnas, 2006) expanded the method to work for ducted propellers.

More advanced methods had also been developed for the two most important issues in the potential flow method, the wake alignment and the viscous effects. (H. S. Lee & Kinnas, 2004, 2005a, 2005b) developed a fully unsteady wake alignment method, including a tip vortex core, in order to determine the accurate wake location for propellers. (Sun, 2008; Sun & Kinnas, 2008) included the viscous effects via coupling with a boundary layer solver (XFOIL) and extended the method to apply to water-jet with a rotor and stator stage.

2.2 PROPELLER DESIGN METHOD

In 1993, Kinnas proposed a new approach for propeller blade design. The objective of this approach was to design the shape of a propeller blade via optimization techniques, which provides a specified mean thrust with minimum torque when subject to the actual *non-axisymmetric* inflow. The optimization method was used to couple with the vortex lattice method (MPUF-3A), and the wetted and cavitating conditions were considered by adding constraints in the optimization. Therefore, in (Mishima & Kinnas, 1996, 1997), a numerical nonlinear optimization method named (CAVOPT-3D) was developed in which the propeller characteristics were determined through a Taylor expansion of results from MPUF-3A. (Griffin, 1998; Griffin & Kinnas, 1998) improved the propeller analysis and design methods (CAVOPT-3D) by including more design constraints, i.e. one variable quadratic skew distribution and minimum pressure constraint. In (Deng, 2005; Kinnas, Lee, Gu, & Deng, 2005), an extension of the method, named CAVOPT-BASE, was developed by using constrained nonlinear optimization, which was based on a performance database of a propeller family. The database was constructed by repeatedly running MPUF-3A.

2.3 PERFORMANCE PREDICTION AND DESIGN OF TIDAL TURBINES

An experimental study on a 3-blade horizontal tidal turbine was performed in a cavitation tunnel and also in a towing tank (Bahaj, Molland, Chaplin, & Batten, 2007), and the corresponding power and thrust coefficients were presented for a range of tip speed ratios. The experimental data provides very useful information for the design of tidal turbines and for the validation of numerical models. A turbine is basically a propeller operating in a reverse rotational direction, and most of the theories and methods originally developed for propellers can be applied to turbines. Several numerical methods were applied to analyze the performance of the same tidal turbine presented in (Bahaj, Molland, et al., 2007), including a blade element method by (Bahaj, Batten, & McCann, 2007; Batten, Bahaj, Molland, & Chaplin, 2008; Batten, Bahaj, Molland, Chaplin, & Sustainable Energy Res, 2007) and a boundary element method by (Baltazar & de Campos, 2008, 2009; Young, Motley, & Yeung, 2010), which also considered the 3-dimensional effects.

All the abovementioned studies were focused on the prediction of the turbine performance. On the other hand, the blade design is also essential since the output power can be maximized via changing the blade geometry. Several numerical methods were applied for turbine designs. A preliminary design method via using lifting line theory was presented in (Epps, Stanway, & Kimball, 2009).

In this thesis, a lower order potential based boundary element method (PROPCAV), a vortex lattice theory based method (MPUF-3A) and a fully viscous commercial RANS solver (FLUENT) are used to predict the performance of the tidal current turbine studied in (Bahaj et al. ,2007). In MPUF-3A, the fully unsteady wake alignment is utilized to improve the prediction and to capture the expansive effects and roll up phenomenon of the wake. The cavity pattern of the turbine subject to uniform inflow is also predicted by PROPCAV. The numerical results are compared with the experimental measurements.

CAVOPT-BASE was modified to work for turbines to search for the optimal geometry by using a PROPCAV-based performance database. The turbine geometry in the experiment is considered as the base geometry. Pitch, chord length, and camber distributions along the span are the variables for the database. Design examples for fully wetted turbines and cavitating turbines are presented. By setting a constraint, which requires the minimum pressure on the blades to be larger than the vapor pressure, a cavitating turbine can be designed to be fully wetted via adjusting the blade geometry.

Moreover, the design method CAVOPT-3D is also modified for the design of marine current turbines. The objective in CAVOPT-3D is changed to maximize the output power coefficient when applying an inequality constraint on the thrust. More details of CAVOPT-BASE and CAVOPT-3D will be addressed in Chapter 3.

Chapter 3

Methodology

3.1 ACTUATOR DISK THEORY

The presence of the turbine causes the approaching current to gradually slow down such that the velocity of the current is already lower than the free-stream speed. The stream tube expands as a result of the slowing down of the current. As the current passes through the turbine, there is a drop in the static pressure. The current then proceeds downstream with a reduced velocity and static pressure, which forms the wake region. Eventually, far downstream, the static pressure of the wake region needs to return to the ambient level. The rise of the pressure causes a further slowing down of the current. By considering the energy extraction process, the turbine that carries out this task is called an actuator disk (Fig. 3.1). It should be noted that there is no swirl in the wake region in the actuator disk theory

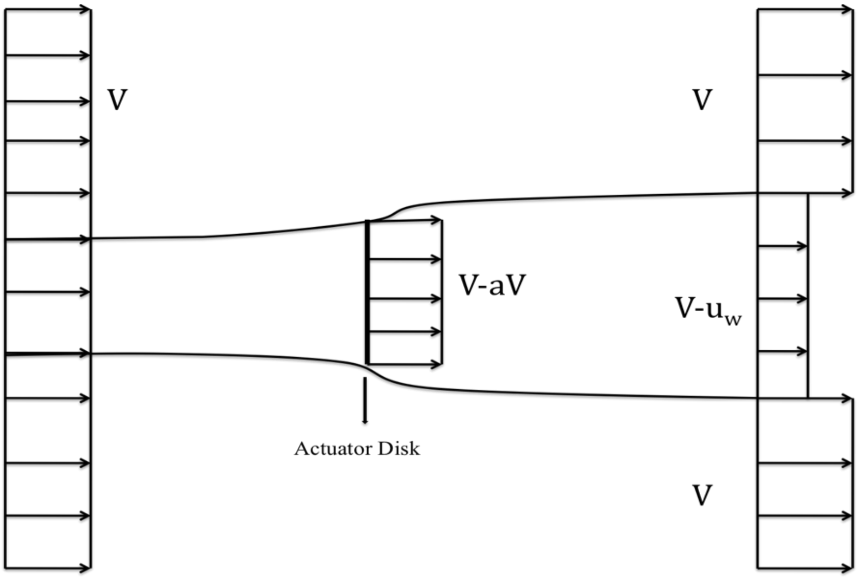

Fig. 3.1 Actuator disk, stream-tube and the variation of velocities.

In Fig. 3.1, V is the inflow velocity, a is the coefficient of velocity reduction when the current go through the actuator disk, u_w is the velocity difference between the downstream and the inflow.

A power coefficient is defined as

$$C_{pow} = \frac{Power}{\frac{1}{2}\rho V^3 A_d} \tag{3.1}$$

where the denominator represents the power available in the current, in the absence of the actuator disk. A_d is the area of the disk, ρ is the current density. In other literatures, the turbine efficiency (η) is defined as

$$\eta = \frac{\text{power produced by turbine}}{\text{power of wind through the turbine disk}} \tag{3.2}$$

where the power of wind through the turbine disk is $1/2\rho V^3 A_d$. Thus,

$$\eta = C_{pow} \tag{3.3}$$

By applying the momentum theory (Burton, Sharpe, Jenkins, & Bossanyi, 2001), the power extraction from the current is given by

$$Power = 2\rho A_d V^3 a(1-a)^2 \tag{3.4}$$

Therefore,

$$C_{pow} = 4a(1-a)^2 \tag{3.5}$$

The maximum value of C_{pow} can be reached by requiring:

$$\frac{dC_{pow}}{da} = 4(1-a)(1-3a) = 0 \tag{3.6}$$

which gives a value of a=1/3 and max(C_{pow})=0.593. The maximum achievable value of the power coefficient is known as the Betz limit after the German aerodynamicist Albert Betz (Betz, 1920). To date, no turbine has been designed to be capable of exceeding this limit.

3.2 LIFTING LINE THEORY

The maximum efficiency of turbines can be achieved by using Actuator Disk Theory, in which a turbine is replaced by a permeable disk with vanishing thickness in the *x*-direction. From the previous section, we know the maximum power coefficient (Betz limit) is 0.593.

3.2.1 Lifting line theory based optimization (LLOPT)

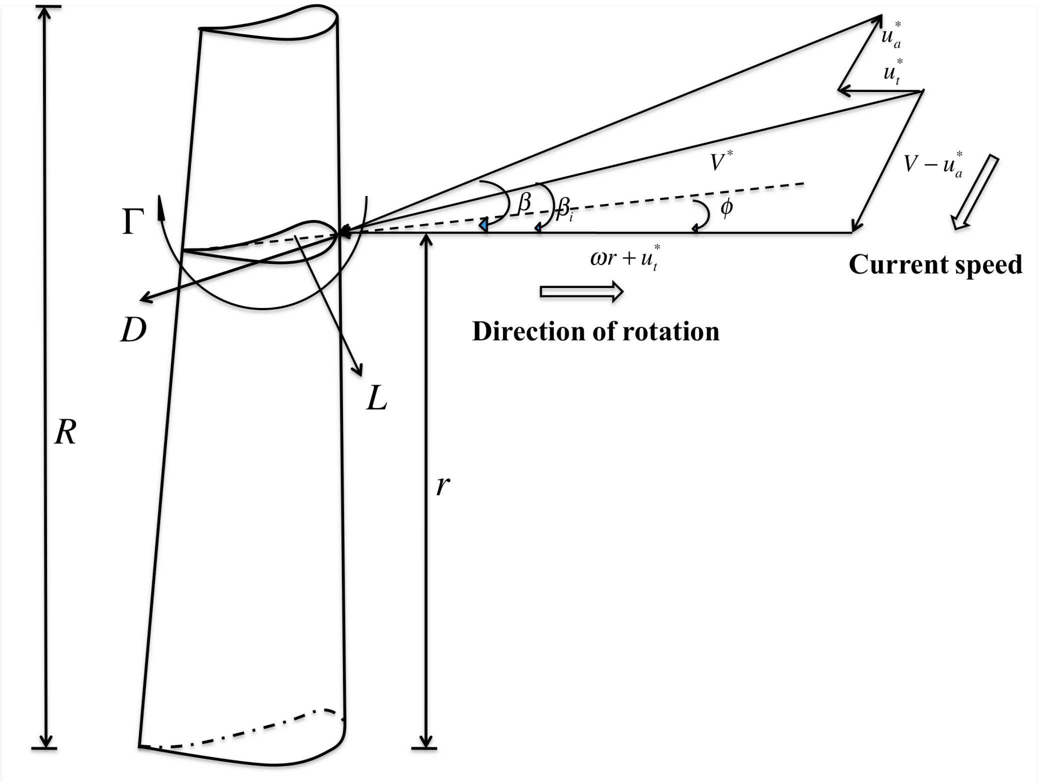

Fig. 3.2 Combined velocity and force diagram on blade section at radius r for turbines

In the lifting surface theory, each turbine blade is considered as a lifting surface with a distribution of bound and free vortex sheet strength. When the chord length vanishes, the bound vortex sheet reduces to a single concentrated vortex, known as lifting line. The wake of the turbine is also considered as a free vortex sheet. Under circumferentially uniform flow, only one blade, designated as "key" blade, need to be analyzed since all blades have the same circulation distribution[1]. Fig. 3.2 shows a combined velocity and force diagram at radius r on the key lifting line. The total inflow velocity $V^*(r)$ is obtained by combining the axial and tangential components of the induced velocity (u_a^* and u_t^*), due to the interaction with other sections and other blades, with the current speed V and the rotational speed ωr. $V^*(r)$ is oriented at an angle β_i with respect to the plane of rotation. ϕ is the blade pitch angle. The differential torque dQ can be expressed by the lift force L and the drag force D:

$$\begin{aligned}
&dQ = (L\sin\beta_i dr - D\cos\beta_i dr)r, \\
&L = \rho V^*\Gamma,\ \ D = \frac{1}{2}\rho(V^*)^2 cC_{DV}, \\
&\left(V^*\right)^2 = \left(V - u_a^*\right)^2 + \left(\omega r + u_t^*\right)^2, \\
&\tan\beta_i = \frac{V - u_a^*(r)}{\omega r + u_t^*(r)}
\end{aligned} \tag{3.7}$$

where c is the sectional chord length, C_{DV} is the sectional drag coefficient, ρ is the fluid density. By integrating over the blade, we can get the total torque as follows:

$$\begin{aligned}
Q &= \rho Z\int_{r_h}^{R}\left[V^*\Gamma\sin\beta_i - \frac{1}{2}\left(V^*\right)^2 cC_{DV}\cos\beta_i\right] rdr \\
&= \rho Z\int_{r_h}^{R}(V - u_a^*)\Gamma\ rdr - \frac{1}{2}\rho Z\int_{r_h}^{R}\left(V^*\right)^2 cC_{DV}\cos\beta_i rdr
\end{aligned} \tag{3.8}$$

where Z denotes the number of blades, R denotes the radius of the turbine, r_h is the hub radius. In this research, lifting line theory is only applied to the inviscid cases (C_{DV} =0) and the torque can be expressed as follows:

---

[1] The effects of the other blades are included in the analysis of the key blade.

$$Q = \rho Z \int_{r_h}^{R} \left[\left(V - u_a^* \right) \Gamma \right] r dr \tag{3.9}$$

By discretizing the blade into M sections, the torque can be written in a discretized form:

$$Q = \rho Z V^2 R^3 \sum_{m=1}^{M} \left[1 - \frac{u_a^*(m)}{V} \right] \Delta\bar{r}\ \bar{r}_m\ \bar{\Gamma}_m$$
$$\Delta\bar{r} = \frac{\Delta r}{R},\ \bar{r}_m = \frac{r_m}{R},\ \bar{\Gamma}_m = \frac{\Gamma_m}{VR} \tag{3.10}$$

where r_m indicates the radius at the m^{th} section, Γ_m is the sectional circulation, and Δr represents the radius interval. Since

$$\frac{u_a^*(m)}{V} = \sum_{n=1}^{M} \bar{\Gamma}_n \bar{u}_a(m,n) \tag{3.11}$$

Eq. (4) becomes

$$Q = \rho Z V^2 R^3 \sum_{m=1}^{M} \left[1 - \sum_{n=1}^{M} \bar{\Gamma}_n \bar{u}_a(m,n) \right] \Delta\bar{r}\ \bar{r}_m\ \bar{\Gamma}_m \tag{3.12}$$

where $\bar{u}_a(m,n)$ is the axial velocities induced at the m^{th} control point by a helical "horseshoe" vortex surrounding the n^{th} control point. $\bar{u}_a$ is computed using the formulas of (Wrench, 1957) for a constant-pitch helical vortex line (Appendix A). In order to find the maximum value of Q, the first-order necessary condition is applied,

$$\frac{\partial Q}{\partial \bar{\Gamma}_i} = 0 \tag{3.13}$$

The following assumption is made to solve the system,

$$\frac{\partial \bar{u}_a(m,n)}{\partial \Gamma_i} = 0,\ i=1,\ldots,M. \tag{3.14}$$

Under this assumption, the differential system of Eq. 3.13 becomes linear (Zan, 2008), and takes the following form:

$$\sum_{m=1}^{M}\left[\overline{r}_m\overline{u}_a(i,m)\overline{\Gamma}_m+\overline{r}_i\overline{u}_a(m,i)\overline{\Gamma}_m\right]=\overline{r}_i,\ i=1,\ldots,M. \tag{3.15}$$

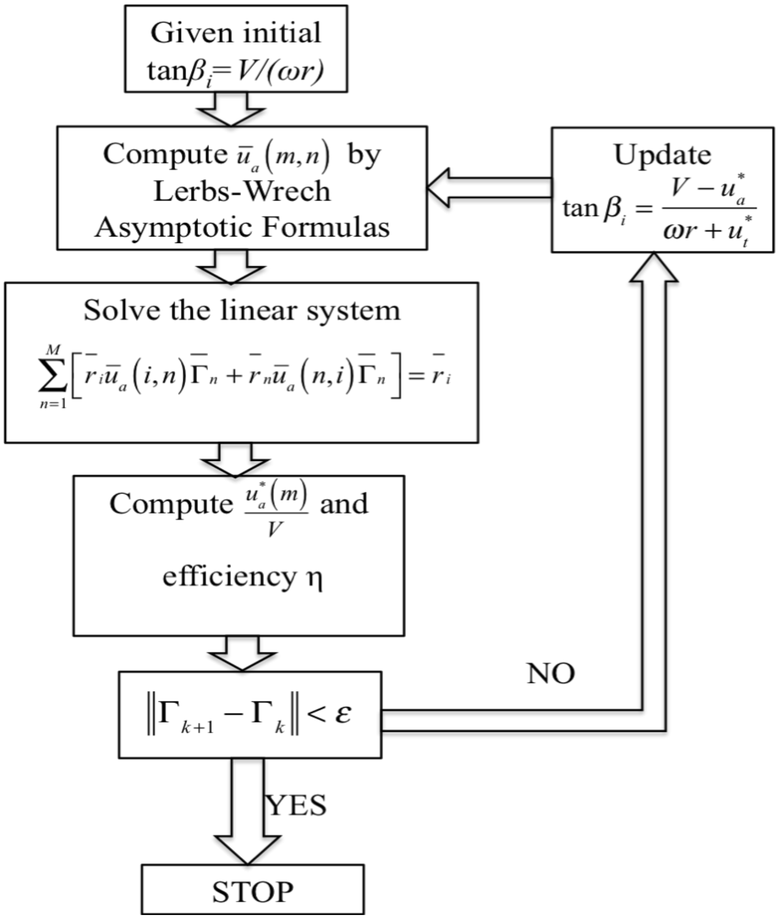

Fig. 3.3 Algorithm of lifting line optimization method (LLOPT)

The optimization solution is obtained by solving this linear system. More details about this optimization method can be found in (Zan, 2008). Fig. 3.3 shows the algorithm of LLOPT, where the efficiency η is defined as:

$$\eta=\frac{Q\omega}{0.5\rho\pi R^2V^3} \tag{3.16}$$

The formulations for the application of LLOPT to a contra-rotating turbine can be found in Appendix B.

3.2.2 Circulation database searching method (LLOPT-BASE)

As will be shown in Chapter 4, the circulation distribution generated in LLOPT is not the global optimum solution due to the assumption that is made in equation (3.14). In order to maximize the torque, a circulation database searching method, named LLOPT-BASE, is applied to search for an improved circulation distribution. The result from LLOPT is used as the input circulation shape to create a circulation database. It is anticipated that the final optimum circulation distribution is almost constant or of constant slope except close to the root and tip where it should be zero. Thus the database is constructed by multiplying the circulation distribution from LLOPT with a linear function $g(x,k,h)$, where k is the slope of the function, and h is the value of function $g(x,k,h)$ when x=0.5(R-r_h). The expression of the function and the range for the variables are given as follows:

$$\begin{gathered} g(x,k,h) = kx + h - 0.5k(R - r_h), \\ r_h \le x \le R,\ k_1 \le k \le k_2,\ h_1 \le h \le h_2 \end{gathered} \tag{3.17}$$

where k_1, k_2 and h_1, h_2 are the lower and upper limits for k and h, respectively. The new circulation distribution becomes:

$$\Gamma(x) = \Gamma_{base}(x) \times g(x,k,h) \tag{3.18}$$

The efficiency of the turbine for a specified circulation distribution is achieved by updating $\tan\beta_i$ until it converges, i.e., by applying what is commonly called wake alignment procedure. The maximum efficiency for a certain base circulation shape is obtained via searching the circulation database. More details about the method are described in (Xu, 2009).

3.2.3 Generation of base blade geometry based on the optimum circulation distribution

The pitch and camber distributions are determined by specifying a circulation distribution, a chord distribution and a blade section profile. The equations for determining the pitch angle ϕ and the sectional maximum camber $f_{\max}$ are given as:

$$\begin{aligned}
&\phi(i) = \beta_i(i) - \alpha_i(i) \\
&\alpha_i(i) = \alpha_0 C_L(i) \qquad , \qquad i = 1,\ldots,M \\
&f_{\max}(i) = f_0 C_L(i) \\
&C_L(i) = \frac{L(i)}{0.5\rho V^*(i)c(i)} = \frac{2\Gamma(i)}{V^*(i)c(i)},
\end{aligned} \tag{3.19}$$

where C_L represents the lift coefficient, α_0 and f_0 are the ideal angle of attack and ideal maximum camber for a certain section when C_L=1.0, and $c(i)$ is the chord length for the section i. In order to produce a base blade geometry, the same chord distribution as that of the experimental turbine is utilized. The final optimum chord distribution will be determined by using CAVOPT-BASE.

3.3 VORTEX LATTICE METHOD (VLM)

The presence of a turbine is represented by the distribution of singularities (vortices and sources) on the blade mean camber surface and its assumed wake surface. The vortex distribution is employed to represent the jump of the tangential velocity both at the camber surface and in the trailing wake sheet. The source distribution is utilized to represent the blade thickness. The vorticity is a vector lying on the mean camber surface, which can be resolved into two arbitrarily assigned components on the surface. Thus, on the turbine blade surface, the vortex distribution will be resolved into spanwise and chordwise components. The chordwise component that sheds into the wake is termed as "trailing vorticity". The unknown strength of the singularities is determined by applying the kinematic and dynamic boundary conditions at some appropriate control points. The kinematic and dynamic boundary conditions will be addressed in the boundary element method. More details of the vortex lattice method can be found in (C. S. Lee, 1979)

3.3.1 Blade Geometry

The vortex lattice method was originally developed for marine propellers. Therefore, the turbine blade geometry in the VLM is defined in a same way as that of propellers. The coordinate systems and the propeller geometrical notation are shown in Fig. 3.4. The three dimensional coordinate system is defined with the positive x being the downstream direction. The y axis is normal to the x axis and is attached to the key blade. The z axis follows the right hand system. The cylindrical coordinate is defined as follows:

$$\begin{aligned} x &= x \\ r &= \sqrt{y^2 + z^2} \\ \theta &= \tan^{-1}\frac{z}{y} \end{aligned} \tag{3.20}$$

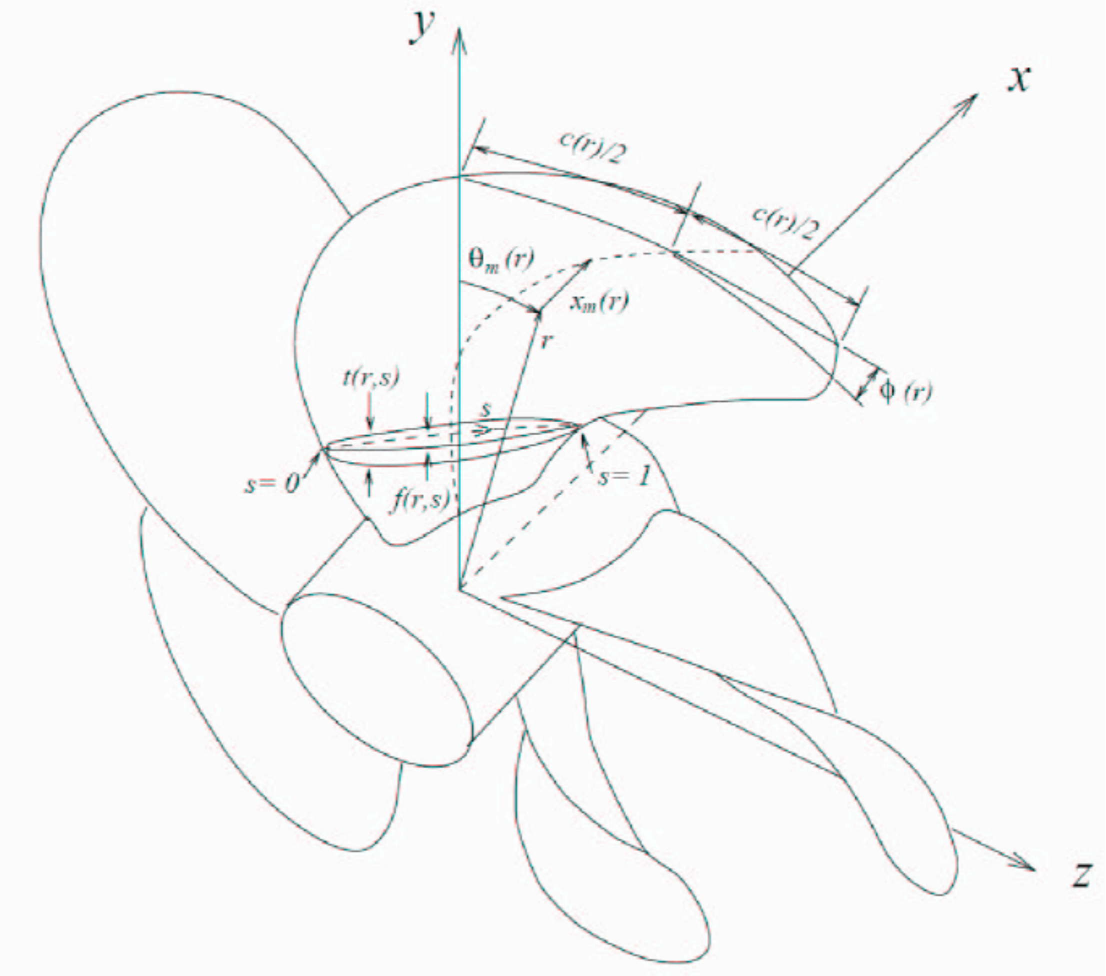

Fig. 3.4 Coordinate systems and geometrical notations in VLM (MPUF-3A), from (Greeley & Kerwin, 1982)

As illustrated in Fig. 3.4, the mid-chord line of the propeller or turbine blade is defined by the radial distributions of skew, $\theta_m(r)$, and rake, $x_m(r)$. The coordinates of the leading and trailing edges are constructed by passing a helix of pitch angle $\phi(r)$ through the mid-chord line.

$$\begin{aligned} x_{l,t}(r) &= x_m(r) \mp \frac{c(r)}{2}\sin\phi(r) \\ \theta_{l,t}(r) &= \theta_m(r) \mp \frac{c(r)}{2}\cos\phi(r) \\ y_{l,t}(r) &= r\cos\theta_{l,t}(r) \\ z_{l,t}(r) &= r\sin\theta_{l,t}(r) \end{aligned} \tag{3.21}$$

where $c(r)$ is the chord length at radius r, and the subscripts l and t denote the leading and trailing edges, respectively.

The camber distribution $f(r,s)$ is defined as the normal distance between the sectional mean line and the nose-tail helix on the cylindrical surface of radius r, where s is the chordwise coordinate with 0 at the leading edge and 1 at the trailing edge. The thickness $t(r,s)$ is added symmetrically normal to the camber line. More details of the blade geometry definition can be found in (J.E. Kerwin & Lee, 1978).

3.3.2 Unsteady wake alignment

It is well known that the trailing wake sheet traveling downstream of a propeller blade experiences contraction and roll-up at the tip region. Similar phenomenon occurs for a marine current turbine. However, the trailing wake will experience expansion rather than contraction. The expansion effect can also be found in the actuator disk model (Fig. 3.1). In the past, the wake contraction and roll-up motion of the propeller were determined from measurements using Laser Doppler Velocimetry (LDV) or more recently Particle Image Velocimetry (PIV) systems. These results can be used to improve the initial geometry of the wake. As for the expansion and roll up of the marine current turbine wake, to the best of author's knowledge, no measurement has been implemented in order to adjust the simplified techniques, which determine the location of the trailing wake sheet.

Since the roll-up and the expansion of wake sheet depend on the operating condition and the blade geometrical characteristics, the applicability of the experimental measurements on the numerical calculations is still confined to the near design condition.

The unsteady wake alignment developed by (H. S. Lee, 2002) can accurately predict the wake geometry by aligning the wake surface with the local velocities, i.e. by applying force free condition on the wake surface. This method is implemented in the vortex lattice method to compute the accurate wake geometry for both turbines and propellers.

The unknown singularities (vortices and sources) are first solved based on the unaligned wake geometry without any modeling of expansion and roll-up at the blade tip. Then the induced velocities are determined by summing up the velocities induced by each blade and wake element, and are evaluated on each edge point of the wake panels. The components of the total induced velocity are shown in Fig. 3.5.

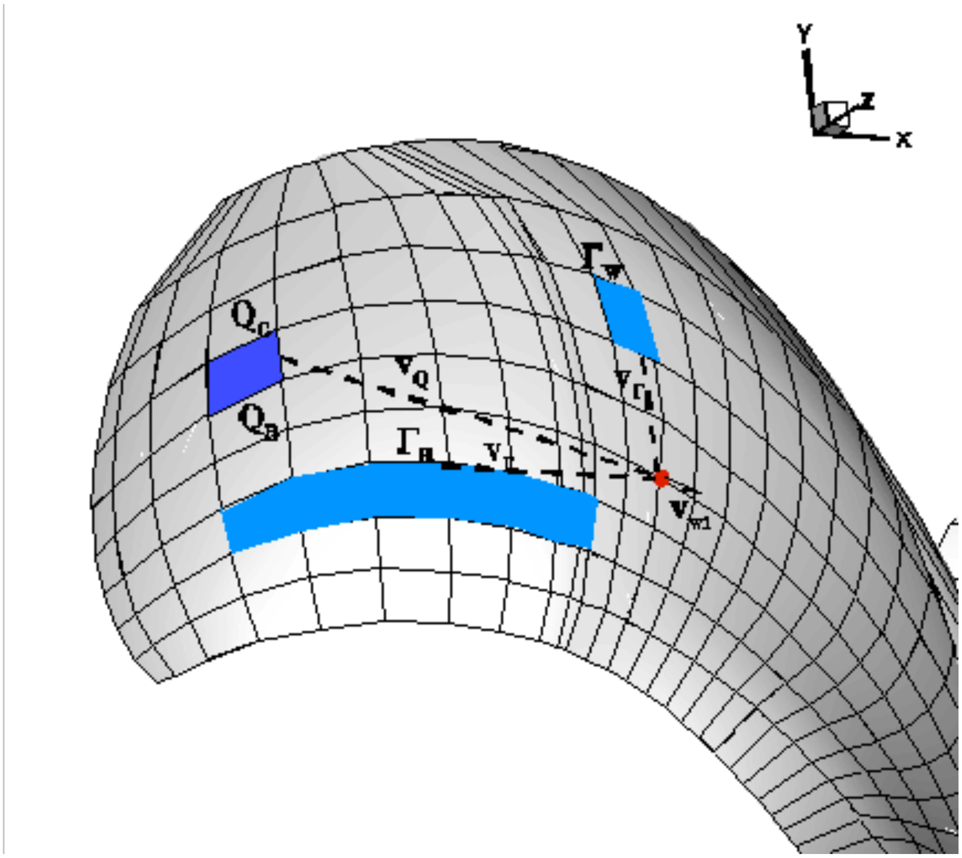

Fig. 3.5 Schematic diagram of the calculation of the induced velocity, from (L. He, 2010). The left part is the blade and the right part is the wake.

$$v_{wi} = \sum_{\Gamma_B} \Gamma_B v_\Gamma + \sum_{Q_B} Q_B v_Q + \sum_{Q_C} Q_C v_Q + \sum_{\Gamma_W} \Gamma_W v_\Gamma \qquad (3.22)$$

where v_{wi} is the induced velocity on a particular wake point, $\boldsymbol{v}_\Gamma$ and $\boldsymbol{v}_Q$ are velocity vectors induced by each unit strength of line source and vortex loop, $\boldsymbol{\Gamma}_B$ and $\boldsymbol{\Gamma}_W$ are the constant strength of bound vortex and free shed vortex. Q_B and Q_C are the magnitude of line sources representing blade and cavity thickness.

Then the locations of new wake geometry are determined by applying the force-free condition on wake, which completes one iteration for the unsteady wake alignment. In order to predict accurate turbine wake geometry, enough iterations are needed to make locations of the wake geometry converge.

It should be noted that the tip vortex model is not included in the vortex lattice method. More details of the unsteady wake alignment method can be found in (H. S. Lee, 2002; H. S. Lee & Kinnas, 2004, 2005b)

3.4 BOUNDARY ELEMENT METHOD (BEM)

Consider a propeller or turbine subject to a non-axisymmetric inflow $\boldsymbol{U}_w(x, r, \theta)$, which rotates at a constant angular velocity $\boldsymbol{\omega}$. The inflow U_w is assumed to be the effective wake[2], i.e. it includes the interaction between the vorticity in the inflow and the propeller or turbine. The definition of the effective wake will be addressed in section 3.5.

The model geometry of turbine blade, trailing wake and coordinate systems are shown in Fig. 3.6. The solution is determined in the (x, y, z) coordinate system, which rotates with the turbine. The turbine in the Fig. 3.6 is a right-handed turbine, i.e. the turbine rotates clockwise when looking upstream. The total inflow velocity relative to the turbine is

$$U_{in}(x,y,z,t) = U_w(x,r,\theta - \omega t) + \omega \times x(x,y,z) \tag{3.23}$$

where $r = \sqrt{(y^2 + z^2)}$ and $\theta = \tan^{-1}(z/y)$

As mentioned in Chapter 1, cavitation can become a problem not only for propellers, but also for turbines. Therefore, the simulation of the cavity is also included in

---

[2] The same assumption is made in the vortex lattice method.

the boundary element method. In this method, the perturbation potential on the surface formed by the combination of the cavity and the blade surface (S_B and S_C) can be expressed as a superposition of the potentials induced by a continuous source distribution and a continuous dipole distribution on S_B and S_C, as well as a continuous dipole distribution on the trailing wake surface S_w.

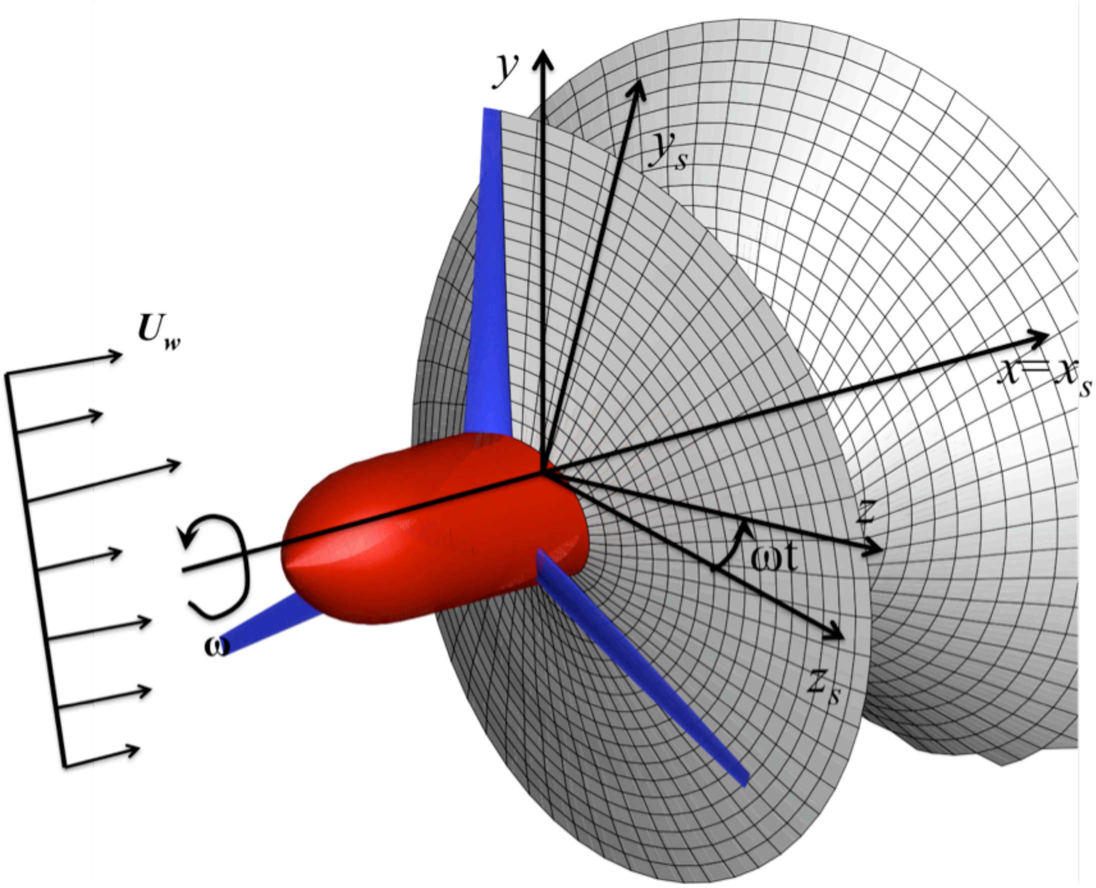

Fig. 3.6 Turbine subject to a general inflow. (Note: x, y, z is a system of coordinates which rotates with the turbine and x_s, y_s and z_s is the inertial system of coordinates, also called the "ship fixed system" in the case of propellers)

Based on potential flow assumption (inviscid and irrotational), the potential ϕ_p at arbitrary point p on the body should satisfy the Green's third identity.

$$
\begin{aligned}
2\pi\phi_p(\vec{x},t) = \iint_{S_B+S_C} \left[\phi_q(\vec{x},t)\frac{\partial G(p;q)}{\partial n_q} - G(p;q)\frac{\partial \phi_q(\vec{x},t)}{\partial n_q} \right] ds + \\
\iint_{S_W} \Delta\phi_W(\vec{x},t)\frac{\partial G(p;q)}{\partial n_q} ds + \iint_{S_T} \phi_q(\vec{x},t)\frac{\partial G(p;q)}{\partial n_q} ds
\end{aligned}
\tag{3.24}
$$

where $G(p;q)=1/R(p;q)$ is the Green's function, $R(p;q)$ is the distance between the field point p and variable point q. n_q is the unit normal vector to the surface of the turbine, the cavity and the wake, pointing to the fluid domain. $\Delta\phi_w$ is the potential jump across the wake surface S_w.

The Green's third identity, together with the kinematic and dynamic boundary conditions can solve the nonlinear potential flow problem that is stated above. The kinematic boundary condition (KBC) requires the flow to be tangent to the surface of the blade, hub and cavity. The dynamic boundary condition (DBC) requires that the pressure everywhere inside and on the cavity be constant and equal to the vapor pressure. More information about the boundary element method can be found in (N. E. Fine, 1992)

3.5 NS-3D AND FLUENT

NS-3D and FLUENT are two similar viscous solvers. FLUENT is a commercial software while NS-3D is developed in the Computational Hydrodynamics Laboratory at The University of Texas at Austin by (Yu, 2008)

3.5.1 Introduction to NS-3D

NS-3D is a finite volume method based viscous flow solver, originally developed for the prediction of the response of ship-shaped hulls (Yu, 2008; Yu & Kinnas, 2009). In this research, NS-3D is used to couple with MPUF-3A in order to predict the performance of turbine when subject to non-uniform inflow. The coupling algorithm requires an iterative procedure, which starts by assuming that the effective wake is the same as the nominal wake in MPUF-3A. The nominal wake is defined as the inflow wake in the absence of propulsor or turbine, while the effective wake is defined as the total time-averaged velocity in the presence of the turbine minus the time-averaged potential flow velocity field induced by the turbine. The resulting pressure distribution on the turbine blade from MPUF-3A is time-averaged and converted to body force terms, which are considered as source terms in the momentum equations, to represent the turbine in NS-3D. The new effective velocity (effective wake) is then calculated by subtracting the turbine-induced velocity from the total velocity obtained from NS-3D at a given effective wake plane. The effective wake plane is located in front of the turbine and as close to it as possible. The updated effective velocity, which becomes non-uniform, is used as a new inflow to the turbine in MPUF-3A. The iteration between MPUF-3A and NS-3D continues until the predicted thrust and torque are converged within a specified tolerance. The procedure of this method is shown in Fig. 3.7. More information about the coupling method can be found in (Kinnas, Chang, Yu, & He, 2009).

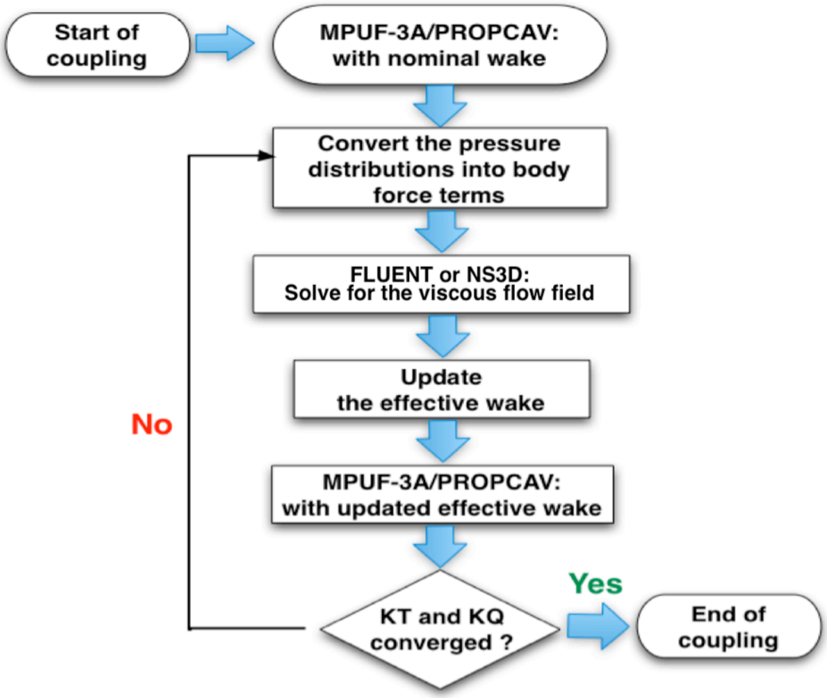

Fig. 3.7 Procedure of the viscous/potential flow method

3.5.2 Introduction to **FLUENT**

The principles and formula of FLUENT can be found in the FLUENT manual (ANSYS, 2009). In this section, only two particular methods that are used in this research will be introduced, namely the periodic boundary conditions and the single moving reference frame.

Periodic boundary conditions are used when the flows across two opposite planes in the computational model are identical. Periodic boundaries can be divided into two types: rotationally and translationally periodic boundaries. Translationally periodic boundaries occur to a rectilinear geometry, while rotationally periodic boundaries can form an included angle about the centerline of a rotationally symmetric geometry (shown in Fig. 3.8).

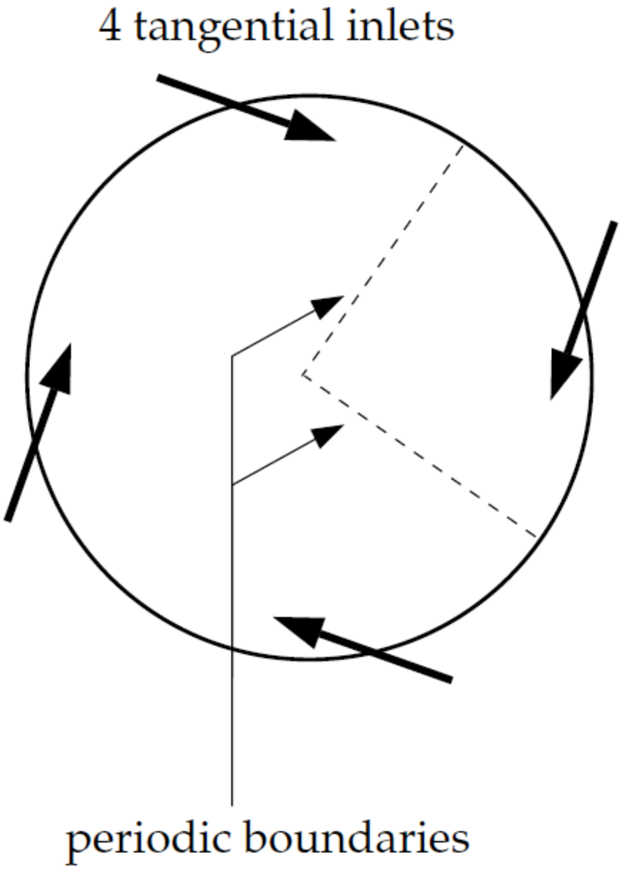

Fig. 3.8 Rotationally periodic boundary (source: FLUENT manual)

The Single Rotating Reference Frame (SRF) modeling can be used for an entire computational domain. The equations for a rotating reference frame, which can be found in the FLUENT manual, are solved in all fluid cell zones. In the SRF modeling, the turbine blade surfaces should have no slip condition, which can ensure that the relative velocity is zero on the moving walls (turbine).

3.6 DATABASE-SEARCHING METHOD (CAVOPT-BASE)

CAVOPT-BASE uses a constrained nonlinear optimization method to search for the optimal turbine geometry in a performance database, which is generated by changing the geometric parameters of base turbine geometry. The base turbine geometry is selected from well-known turbines or from the design result of LLOPT-BASE. The turbine geometric parameters in this research are given as follows:

$$\begin{aligned}(P/D)_{design} &= (P/D)_{base} \times x_1,\\ (c/D)_{design} &= (c/D)_{base} \times x_2,\\ (f/c)_{design} &= (f/c)_{base} \times x_3,\end{aligned} \tag{3.25}$$

where P/D, c/D, and f/c represent normalized pitch, chord and camber distribution, respectively. D is the diameter of the turbine, x_1, x_2, and x_3 are the three multipliers corresponding to these three design parameters. A lower bound x_i^{LB} and an upper bound x_i^{UB} are specified for each multiplier, and the density of the database is determined based on the number of intervals between these two bounds. The constrained nonlinear optimization problem is given in the following form:

$$\begin{aligned}&\text{maximize } C_{\text{pow}}(x),\\ &\text{subject to } C_{P\min}(x) \le CPMIN,\\ &\qquad\qquad x_i^{LB} \le x_i \le x_i^{UB}, i = 1,2,3,\end{aligned} \tag{3.26}$$

where

$$\begin{aligned}&C_{\text{pow}} = \frac{16K_Q}{J^3},\ J=\frac{V}{nD},\ K_Q = \frac{Q}{\rho n^2 D^5},\\ &C_{P\min}(x) = \max(-Cp),\ Cp = (p - p_0)/(0.5\rho n^2 D^2).\end{aligned} \tag{3.27}$$

C_{pow} is the power coefficient, K_Q is the torque coefficient, J represents the advance ratio which is defined as the ratio of the inflow velocity V with respect to the product of rotational frequency n and the turbine diameter D. Q denotes the torque around the turbine axis, ρ is the fluid density, n indicates the rotational frequency, C_p represents the pressure coefficient, p_0 is the far upstream pressure, and p denotes the pressure on blades. $CPMIN$ is the maximum allowed C_{Pmin} which corresponds to the cavitation number $\sigma_n=(p_0-p_v)/(0.5\rho n^2D^2)$, where p_v indicates the vapor pressure. In order to keep the maximum thickness the same among different designs and not compromise the structural integrity of turbine, the thickness distribution *t/D* is not chosen as a parameter. When utilizing CAVOPT-BASE to design a turbine in shallow water, cavitation can be reduced or eliminated by enforcing a *CPMIN* constraint. In addition, more design parameters and constraints can be included to refine the database, and the details are mentioned in (Deng, 2005; Kinnas, et al., 2005).

3.7 NONLINEAR OPTIMIZATION METHOD (CAVOPT-3D)

3.7.1 B-spline blade geometry

In section 3.3, the blade geometry of turbine or propeller is defined in a traditional way. In most of numerical methods, the radial distributions of pitch, rake, and skew, as well as the chordwise distributions of camber and thickness are usually given. Numerical errors arise due to the interpolation process that is necessary to determine the actual blade surface. In this design method, a B-spline representation of the blade is adopted, in which all points of the blade surface are defined uniquely.

In MPUF-3A, non-uniform B-spline curves are defined as:

$$P(u,w) = [x(u,w), y(u,v), z(u,v)] = \sum_{i=0}^{Nu-1} \sum_{j=0}^{Nw-1} d_{ij} N_{i,4}(u) N_{j,4}(w) \tag{3.28}$$

where $d_{i,j}$ are B-spline control points, $N_{i,4}(u)$ and $N_{j,4}(w)$ are B-spline basis of order 4, *u, v and w* are parameters for B-spline, N_u and N_w are the number of B-spline control points in *u*-direction and *w*-direction, respectively.

A cubic B-spline surface formed by a 4 × 4 vertex polygon net is shown in Fig. 3.9.

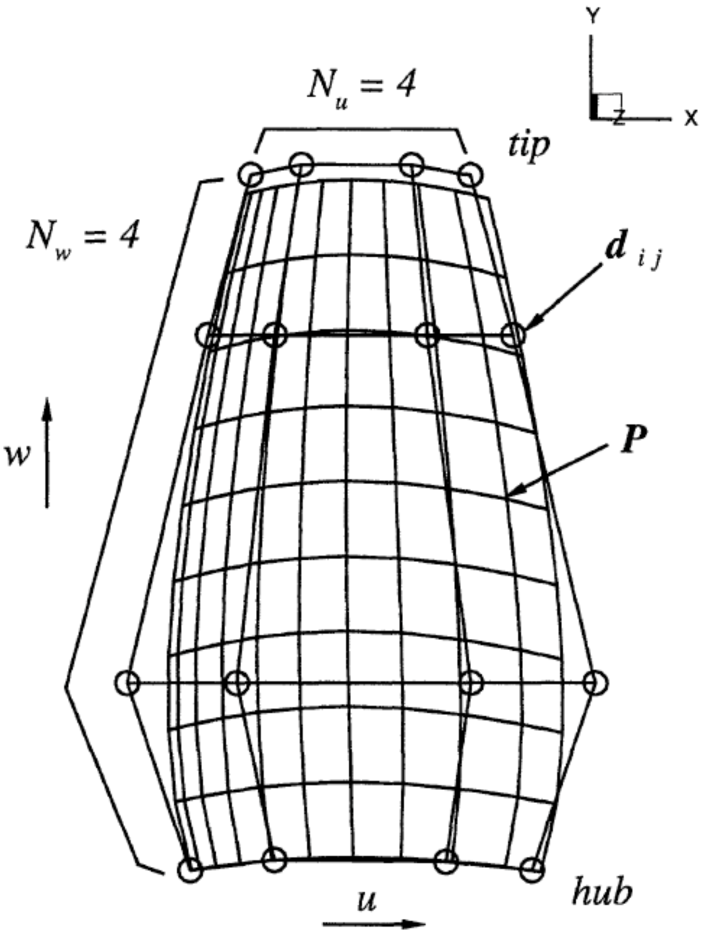

Fig. 3.9 Cubic B-spline surface. 4×4 vertex polygon net and 10×9 grid blade surface in MPUF-3A, from (Mishima & Kinnas, 1996)

3.7.2 Design method

The present method couples the numerical optimization scheme with a vortex lattice method described in section 3.3. The corresponding method is designated as CAVOPT-3D. The objective function $f(x)$ and constraint functions (equality $h_i(x)$ or inequality $g_i(x)$) need to be specified for any optimization problem. In the propeller problem, the torque needs to be minimized for a given thrust. Therefore, the objective function would be the torque coefficient, and the equality constraint function would be the thrust coefficient.

$$
\begin{aligned}
& f(x) = K_Q(x) \\
& h_1(x) = \frac{K_T(x) - K_{T0}}{K_{T0}}
\end{aligned}
\tag{3.29}
$$

where $K_T(x)$ and $K_Q(x)$ are the thrust and torque coefficients defined in the vortex lattice method. x is the design variable vector which defines the blade geometry. Notice that the equality constraint is normalized to its required value, K_{T0}.

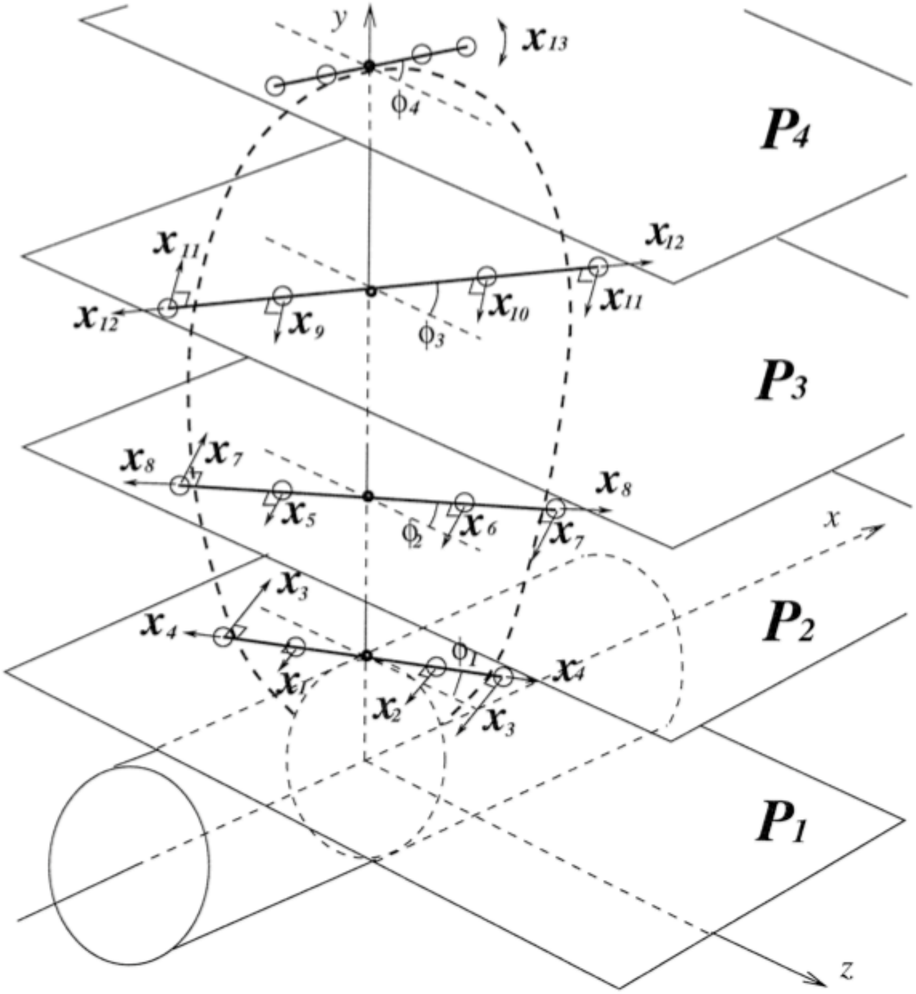

Fig. 3.10 Initial B-spline polygon vertices, design variables, and vertex movement (4×4 vertices), from (Mishima & Kinnas, 1996)

In this method, 13 variables are used, which are shown in Fig. 3.7. The 13 variables determine the direction of the movement of each vortex at each optimization iteration to specify improved blade geometry. The direction can be decomposed into two parts, the one normal to the line connecting the initial leading edge point and trailing edge point on a plane with a certain *y,* and the other being the chordwise direction which could elongate or shorten the chord length. In the case that the chord length distribution of the blade is specified in the method, no vertices are allowed to move in the chordwise direction. It should be noted that the B-spline polygon net only defines the blade geometry without skew. Skew can be added independently after the generation of a no-skew B-spline blade geometry.

In this problem, the quadratic approximations of the objective function and constraints functions are used, since quadratic functions are convex, and also easy to deal with. The objective function and constraints functions are shown below in terms of quadratic expressions (Mishima & Kinnas, 1996).

$$\begin{aligned}
&f(x) = F_f + x^T G_f + \frac{1}{2} x^T H_f x \\
&g_1(x) = F_{g1} + x^T G_{g1} + \frac{1}{2} x^T H_{g1} x \\
&g_2(x) = F_{g2} + x^T G_{g2} + \frac{1}{2} x^T H_{g2} x \\
&\qquad\quad \ldots\ldots \\
&g_m(x) = F_{gm} + x^T G_{gm} + \frac{1}{2} x^T H_{gm} x \\
&h_1(x) = F_{h1} + x^T G_{h1} + \frac{1}{2} x^T H_{h1} x \\
&h_2(x) = F_{h2} + x^T G_{h2} + \frac{1}{2} x^T H_{h2} x \\
&\qquad\quad \ldots\ldots \\
&h_l(x) = F_{hl} + x^T G_{hl} + \frac{1}{2} x^T H_{hl} x
\end{aligned} \tag{3.30}$$

where m and l are the number of inequality constraints and equality constraints, respectively. It should be noted that in the propeller torque minimization problem, only one equality constraint, which is specified in equation (3.26), is applied. F_f, $\boldsymbol{G_f}$, $\boldsymbol{H_f}$, F_{g1}, $\boldsymbol{G_{g1}}$, $\boldsymbol{H_{g1}}$, F_{g2}, $\boldsymbol{G_{g2}}$, $\boldsymbol{H_{g2}}$, …, F_{hl}, $\boldsymbol{G_{hl}}$, $\boldsymbol{G_{h2}}$, …, $\boldsymbol{H_{hl}}$ are the coefficients of the quadratic functions in terms of the design variables.

In order to specify all the coefficients for the quadratic functions, the first stage is to obtain linear approximations of the objective function and constraint functions. F_f, $\boldsymbol{G_f}$, F_{g1}, $\boldsymbol{G_{g1}}$, F_{g2}, $\boldsymbol{G_{g2}}$, …, F_{hl}, $\boldsymbol{G_{hl}}$, $\boldsymbol{G_{h2}}$, … can be determined by running MPUF-3A n+1 times with n+1 different blade geometries, where n is the variable number of vector x. Implementing the linear optimization by approximating objective and constraints functions with linear functions could make the scheme more stable for the nonlinear optimization thereafter. More MPUF-3A runs are needed for specifying the $\boldsymbol{H_f}$, $\boldsymbol{H_{g1}}$, $\boldsymbol{H_{g2}}$, …, $\boldsymbol{H_{hl}}$. The minimization problem can eventually be solved for the quadratic functions. More details of this method could be found in (Mishima & Kinnas, 1996, 1997).

Chapter 4

Results for Turbines

4.1 OPTIMUM CIRCULATION DISTRIBUTION

4.1.1 Single turbine

In LLOPT, a non-dimensional turbine model with r_h/R=0.2 is used for generating the circulation shape used in LLOPT-BASE. The hub effect is not considered in this research. Fig. 4.1 shows the convergence history for $\tan\beta_i$ (defined in Section 3.2.1), which indicates that the LLOPT can converge fast (4 iterations). In LLOPT-BASE, k and h range from -0.15 to 0.15 and 0.5 to 1.1, respectively. As shown in Fig. 4.2, the circulation distribution for a 3-blade turbine operating at J=0.524 (TSR=π/J=6.0) increases in LLOPT-BASE, where $\bar{r}_m$ and $\bar{\Gamma}_m$ are defined in Eq. 3.10. The optimum efficiency given by LLOPT is equal to 0.425. As shown in Fig. 4.3, the optimum efficiency from LLOPT-BASE is increased by 14%, to 0.485, when k=-0.13 and h=0.90.

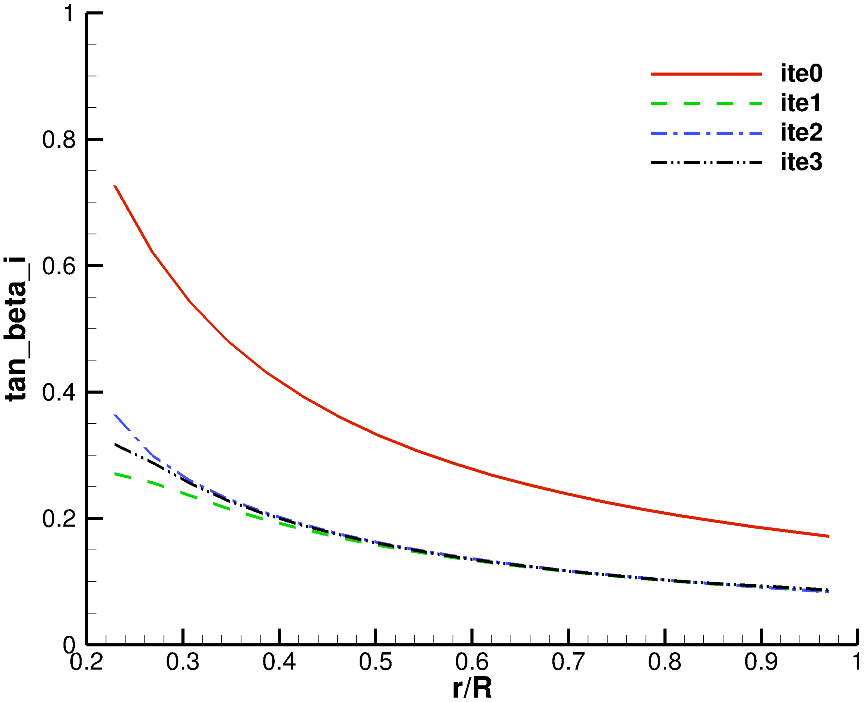

Fig. 4.1 Convergence history for tanβ_i of the single turbine design via LLOPT

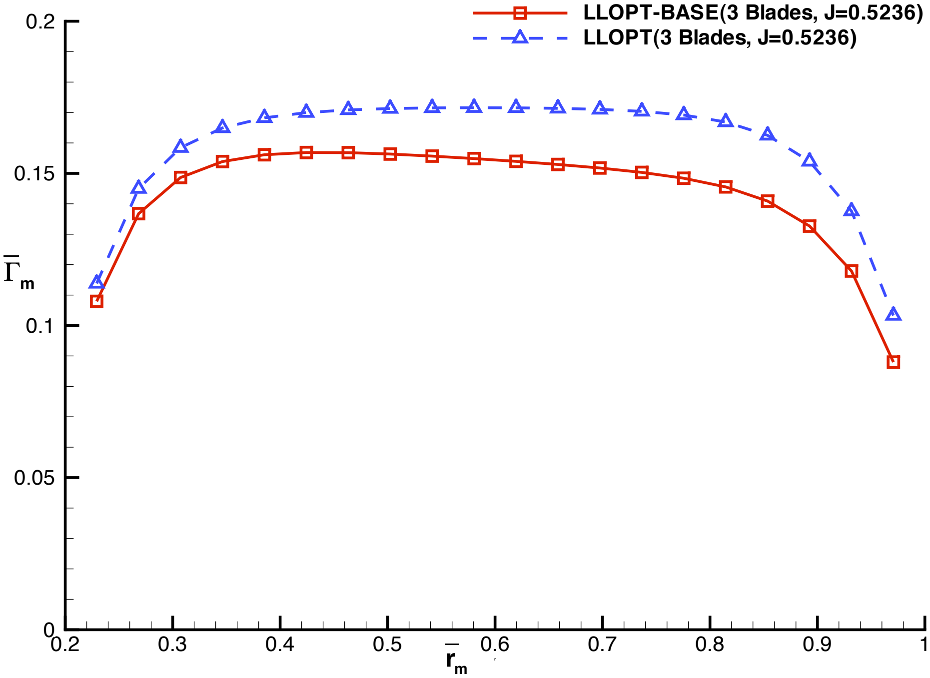

Fig. 4.2. Circulation distributions from LLOPT and LLOPT-BASE for a 3-blade turbine

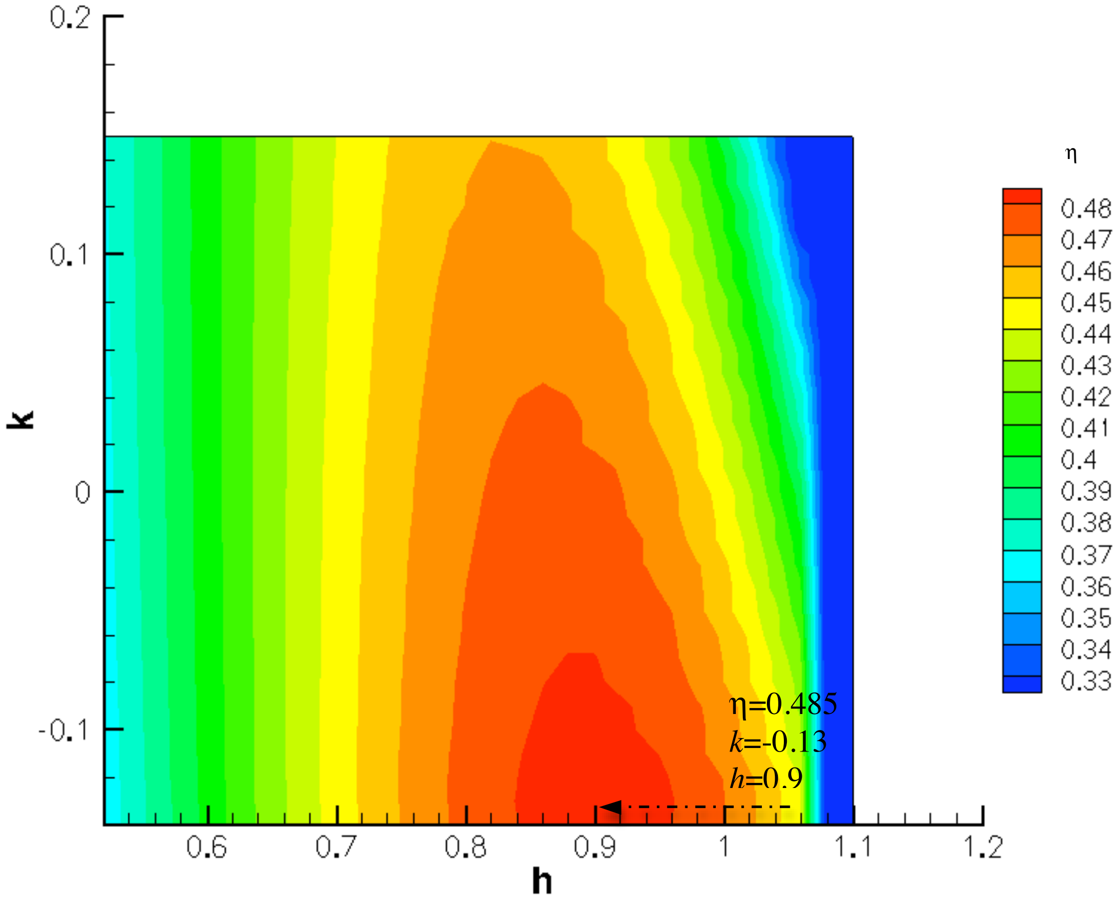

Fig. 4.3 Efficiency contour plot from LLOPT-BASE (3-blade turbine; *J*=0.5236)

Based on the actuator disk theory, the Betz limit gives a maximum efficiency of 0.593, and u_a^*/V is equal to 1/3 when the Betz limit is reached. The effect of blade number (Z=3 and Z=10) and advance ratio on the efficiency is investigated in this research. As shown in Fig. 4.4, the efficiency obtained from LLOPT-BASE approaches the Betz limit gradually when J approaches 0 (*TSR* approaches infinity). However, the efficiency from LLOPT is less than 0.5 even with a low J. As is shown in Fig. 4.5, for the 10-blade and J=0.1 case, the value of u_a^*/V from LLOPT-BASE is close to the ideal value of 1/3 for each section of the blade, while the result from LLOPT is around 0.5.

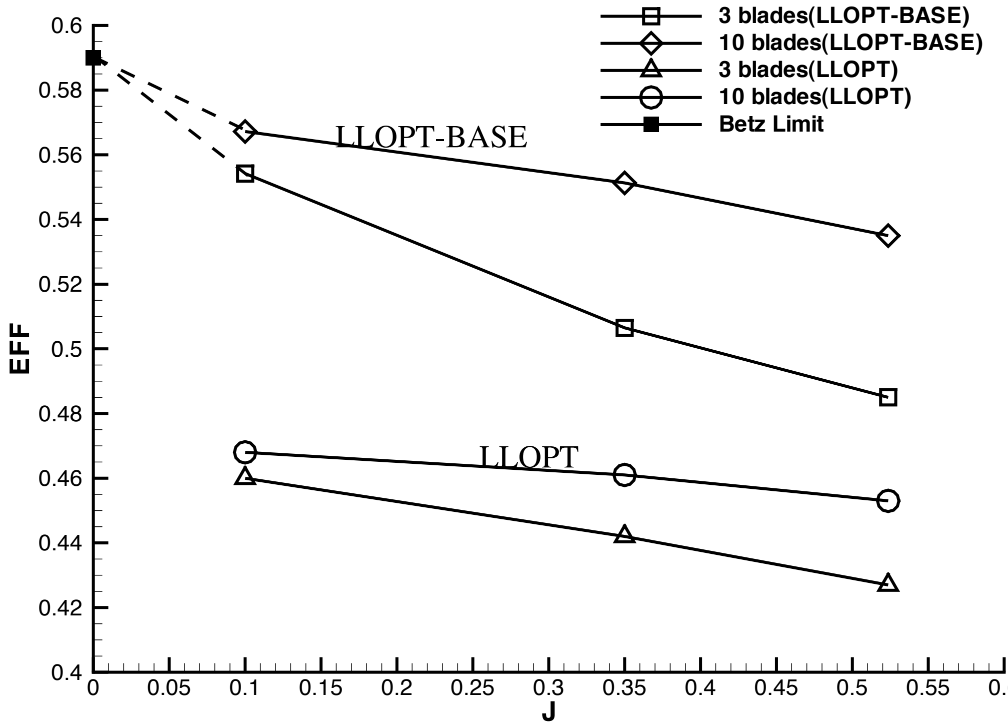

Fig. 4.4 Comparison of the efficiency from LLOPT and LLOPT-BASE for different Z and *J*

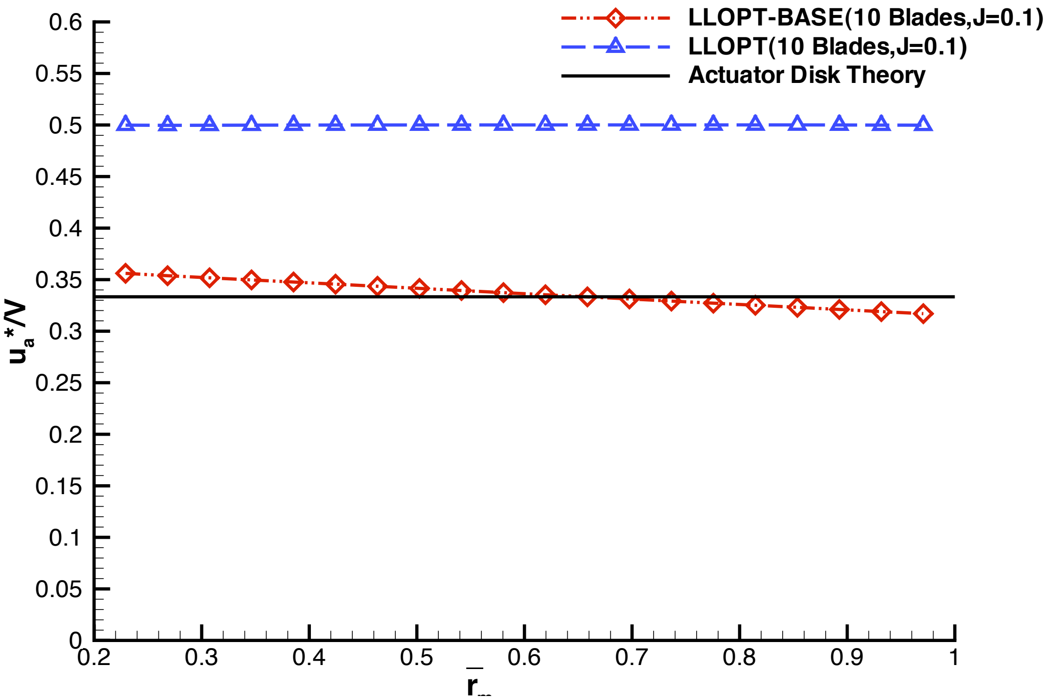

Fig. 4.5 Comparison of the axial induced velocity from LLOPT and LLOPT-BASE and actuator disk theory

For a given J, the LLOPT-BASE is proved to work better in approaching the global optimum circulation distribution, which produces the maximum torque within the database. The small difference between the induced velocity from LLOPT-BASE and that from the actuator disk theory is caused by: (1) the shape of the circulation distribution, predicted by LLOPT, is not accurate enough for LLOPT-BASE to produce the optimum distribution; (2) the two-variable-based database is not sufficient to capture the global optimum circulation distribution; (3) the assumption that r_h=0.2 contradicts the actuator disk theory; (4) the wake alignment in LLOPT is determined by assuming a cylindrical wake of constant pitch in the axial direction, which does not reflect the actual wake geometry behind a turbine. More improvements of LLOPT-BASE could be made by changing the wake alignment method, reducing the hub radius and including more variables in the database.

4.1.2 Contra-rotating turbine

As we know from the previous section, LLOPT cannot generate a final optimum circulation distribution for a single turbine. In this research, the lifting line optimization method (LLOPT) is also utilized to produce the optimum circulation distribution for a contra-rotating turbine. The results are compared with those from a single turbine.

4.1.2.1 Comparison between a single turbine and a contra-rotating turbine

The values of parameters and optimum results (from LLOPT) for a single turbine and a contra-rotating turbine are illustrated in Table 4.1. A contra-rotating turbine consists of two components, the front turbine and the back turbine. The gap between these two components is chosen to be 0.1 and the hubs are also equal to 0.2. In order to compare with the results from a single turbine, the relative *TSR* (front *TSR* plus back *TSR*) for the contra-rotating turbine is equal to the total *TSR* of a single turbine. A contra-rotating turbine has the advantage of reducing the swirl behind the turbine, which could greatly reduce the loss of the energy. Thus, in the inviscid case, the contra-rotating turbine has great potential to generate higher output power. As shown in Table 4.1, the total efficiency for the contra-rotating turbine is 0.486, which is higher than that of a single turbine. Nevertheless, the power coefficient of a contra-rotating turbine may become smaller when including the viscous effect, since the two-component contra-rotating turbine could have more viscous loss of energy due to increased frictional drag. The experimental results (Clarke, et al., 2008) indicate that a contra-rotating tidal current turbine has similar power coefficient to that of a single turbine.

It should be noted that the maximum efficiency of a single turbine operating in a same condition is 0.485 when using LLOPT-BASE, which is almost the same as that of a contra-rotating turbine. More details of LLOPT-BASE can be found in the previous section.

Table 4.1 Parameters and results for a single turbine and two components (front and back) of a contra-rotating turbine

	Radius	Hub Radius	*TSR*	*Z* (blades)	Inflow	No. of Sections	Efficiency
Single(LLOPT)	1.0	0.2	6.0	6	1.0	20	0.4453
Front	1.0	0.2	3.0	3	1.0	20	0.2432
Back	1.0	0.2	3.0	3	1.0	20	0.2428

Fig. 4.6 shows the normalized optimum circulation distributions for the contra-rotating turbine. In this case the two components have the same diameter and the expansion of the wake is ignored. Also shown in Fig. 4.6 is an optimum circulation distribution (LLOPT result) for a single turbine operating at the same total *TSR*. The single turbine is 6 bladed in order to compare with the contra-rotating turbine. The gap of circulations between the single turbine and the contra-rotating turbine is partly because

the *TSR* for each component of the contra-rotating turbine is only half of that of a single turbine.

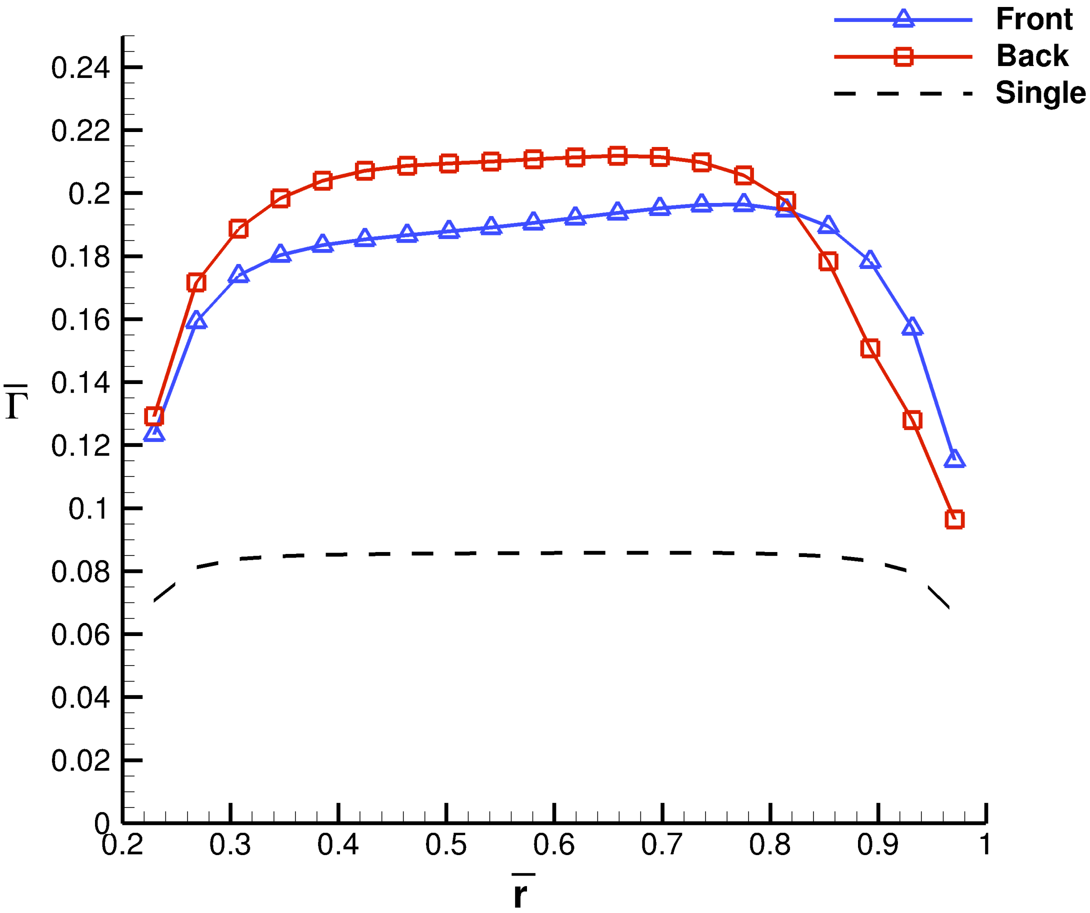

Fig. 4.6 Optimum circulation distribution for both single turbine and contra-rotating turbine (Note: the direction of Γ for the back turbine is opposite to that of the front. In this figure, both of them are plotted positive)

4.1.2.2 Convergence analysis of tanβ_i

In the lifting line theory, the wake alignment of turbine is applied by updating the pitch angle β_i. As shown in the procedure of the optimum circulation calculation in Appendix B, β_i can be updated by calculating self-induced and interaction-induced velocities at each iteration. Thus the convergence of the LLOPT method could be investigated by investigating the variation of tanβ_i. Fig. 4.7 and Fig. 4.8 show the convergence history of tanβ_i for both the front and back components of the contra-rotating turbine. It only takes 6 iterations to make LLOPT converge, and the tanβ_i for the front turbine has a very good convergence at different radii. Nevertheless, the convergent results of the back turbine indicate some problems at the tip and the hub root of the blade. The local convergent problems for the back turbine do not affect significantly the global convergence of the method since the convergence is based on averaged values.

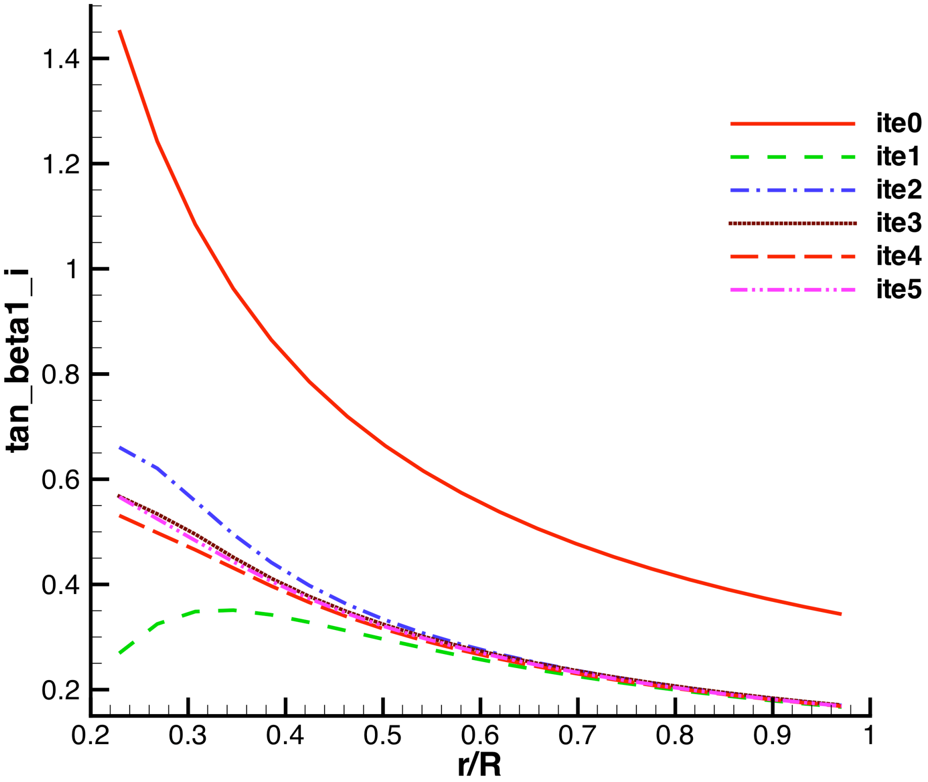

Fig. 4.7 Convergence history for tanβ_i of the front turbine for the contra-rotating turbine

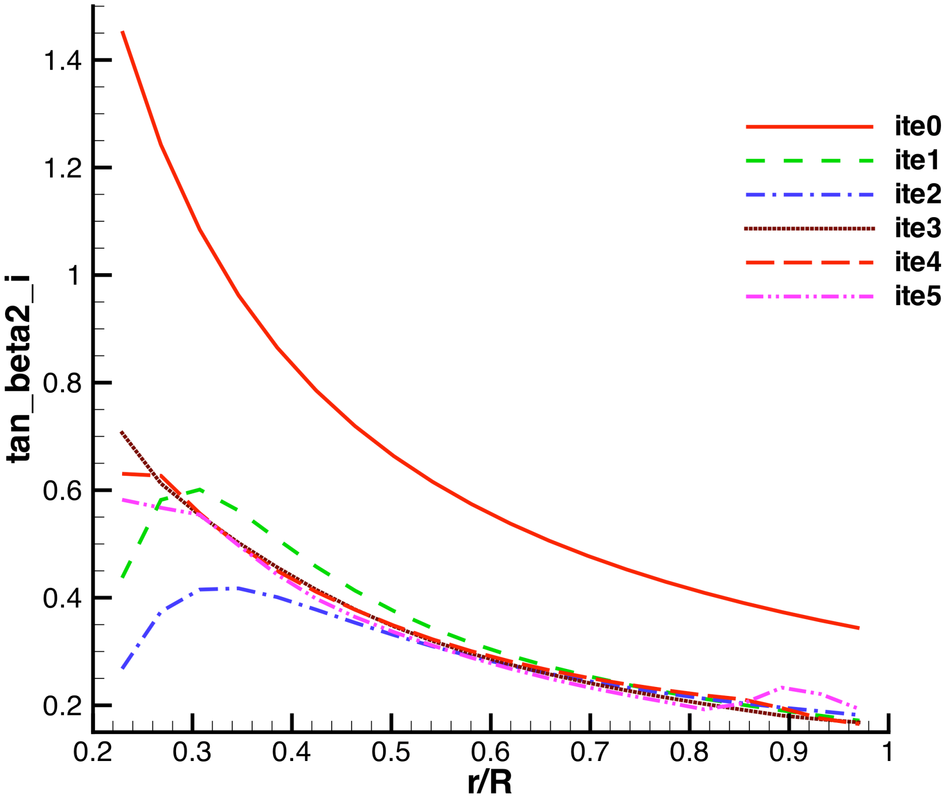

Fig. 4.8 Convergence history for tanβ_i of the back turbine for the contra-rotating turbine

Table 4.2 Efficiencies of the contra-rotating turbine for different *TSR*s (3 blades and 0.2 hub radius)

Total Js	0.5236	0.3926	0.3141	0.2617	0.2243	0.1963	0.174	0.1570	0.1308	0.1121
Total TSR	6	8	10	12	14	16	18	20	24	28
η for front	0.2432	0.2563	0.2636	0.2688	0.2726	0.2754	0.2775	0.2792	0.2835	0.2847
η for back	0.2428	0.2746	0.2757	0.2768	0.2778	0.2786	0.2793	0.28	0.282	0.2827
Total η	0.486	0.5309	0.5393	0.5456	0.5504	0.5540	0.5568	0.5592	0.5655	0.5674

4.1.2.3 Efficiencies of a contra-rotating turbine for different Tip Speed Ratios

The maximum efficiencies of a single turbine for different blades number and different advance ratios are investigated in the previous section. However, for a single turbine, the maximum efficiency from the LLOPT method cannot go beyond 0.5 in any circumstance. Two different methods, LLOPT-BASE and the constant circulation method (Xu, 2009) are utilized to modify the LLOPT. The two modified methods can approach the Betz limit gradually for a single turbine. In this research, the same LLOPT method is used, and the efficiencies of a contra-rotating turbine for different *TSR* are shown in Table 4.2 and Fig 4.9. The total efficiencies of a contra-rotating turbine can approach the Betz limit when the advance ratio approaches zero. Moreover, when the hub radius is reduced from 0.2 to 0.05 and *TSR* increase to 28, the total efficiency for the contra-rotating turbine is about 0.5897, which is more than 99% of the Betz limit. Actually, by greatly reducing the swirl behind the turbine and ignoring the viscous effect, a contra-rotating turbine is similar to an actuator disk when TSR goes to infinity. (J. E. Kerwin, 2001) has already shown that a contra-rotating propeller with increasing number of blades approaches an actuator disk, due to the swirl cancelation.

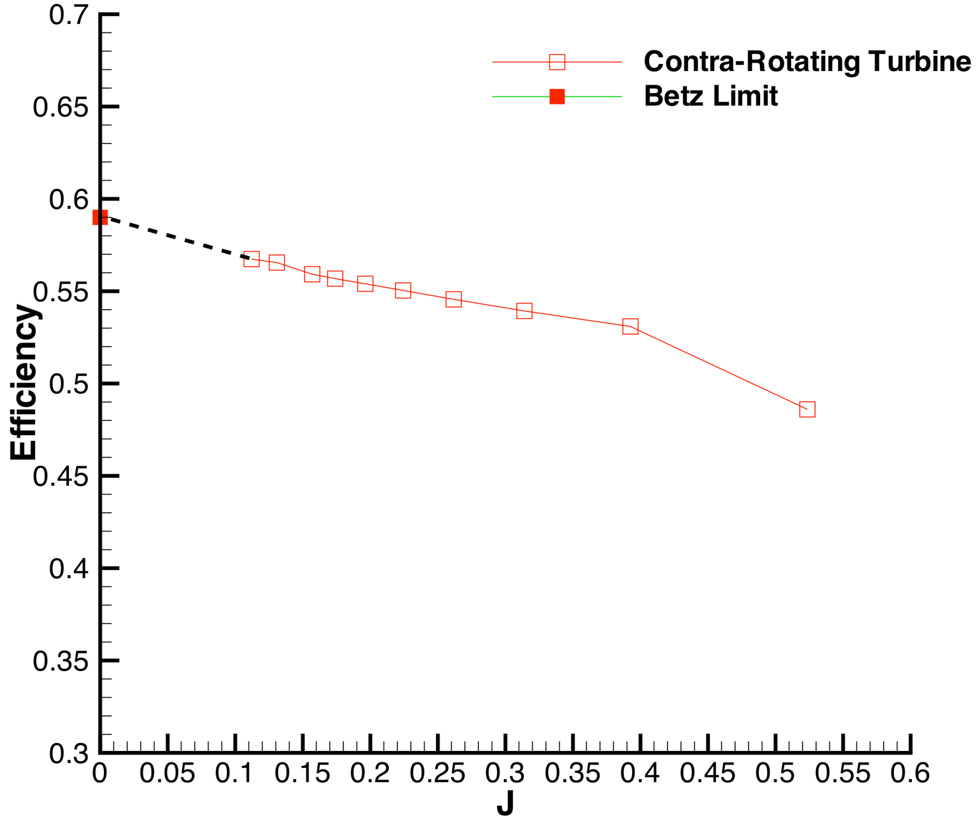

Fig. 4.9 Total efficiencies of a contra-rotating turbine for different Advance Ratios (J)

4.1.2.4 Analysis of the Ratio of TSR between two components

A contra-rotating turbine could significantly reduce the total torque on the support structure, which can greatly simplify the structural design of a tidal turbine. In the design problem, the ideal objective is to eliminate the total torque applied on the support structure without significantly affecting the total output power. However, the assumption of the same *TSR* for both front and back turbines cannot guarantee the same torque with opposite direction on the support structure. Thus, a proper ratio of *TSR* between the two components should be investigated. The optimum ratio of *TSR* can vary with the spacing between the components (δ), the blade number (Z) for each component and the operating conditions. In this research, a 3-blade front and back turbine operating with the spacing

(δ) equal to 0.1*R* is investigated. The *TSR* for the front turbine (*TSR*1) is fixed at 6.0, and the *TSR* for the back turbine (*TSR*2) can vary. As is shown in Table 4.3, the total efficiencies for different *TSR* ratios are similar, and the optimum *TSR* ratio for this case is 0.875, which produces almost zero total torque on the support structure. It should be noted that the viscous effects are not included in these cases, and the optimum *TSR* ratio may change when including viscous effect.

Table 4.3 Efficiencies of the contra-rotating turbine for different *TSR* ratios (Z=3 and δ=0.1*R*)

*TSR*1/*TSR*2	1.0	0.95	0.925	0.90	0.875	0.85	0.825	0.8
Front η	0.2688	0.2699	0.2705	0.2711	0.2717	0.2724	0.2731	0.2739
Back η	0.2718	0.2749	0.2739	0.2729	0.2718	0.2706	0.2694	0.2681
Total η	0.5406	0.5448	0.5444	0.544	0.5435	0.543	0.5425	0.542

4.2 HYDRODYNAMIC ANALYSIS OF MARINE CURRENT TURBINES

4.2.1 The experiment

An experiment with a 3-blade horizontal marine current turbine model was carried out in the University of Southampton in the United Kingdom (Bahaj, Molland, et al., 2007). The tests were carried out in the 2.4m×1.2m cavitation tunnel and the 60m towing tank. In order to maximize Reynolds number and not to incur excessive tunnel blockage correction, a rotor diameter of 800 mm was chosen in the experiment. Fig. 4.10 shows that the test marine current turbine was arranged to be close to the centre of the cavitation tunnel.

Fig. 4.10 Cavitation tunnel with a marine current turbine, from (Bahaj, Molland, et al., 2007).

The blade sections of the turbine are interpolated from 5 two-dimensional section profiles, NACA 63-812, NACA 63-815, NACA 63-818, NACA 63-821 and NACA 63-824. The last two digits of the NACA 63 series indicate the ratio of the maximum thickness with respect to the chord length. A chord length, thickness and pitch distribution with 17 sections of the blade is shown in Table 4.4. The pitch distribution in the figure is actually the pitch angle distribution with hub pitch angle equal to 15 degrees. Adding 10 degrees to each radial section can easily develop a 25 degrees hub pitch setting, which will be utilized in this research.

Table 4.4 Chord, pitch and thickness distribution for the blade of the marine current turbine (source:(Bahaj, Molland, et al., 2007))

r/R	Radius (mm)	c/R	Pitch distribution (deg)	t/c (%)
0.2	80	0.125	15	24
0.25	100	0.1203	12.1	22.5
0.3	120	0.1156	9.5	20.7
0.35	140	0.1109	7.6	19.5
0.4	160	0.1063	6.1	18.7
0.45	180	0.1016	4.9	18.1
0.5	200	0.0969	3.9	17.6
0.55	220	0.0922	3.1	17.1
0.6	240	0.0875	2.4	16.6
0.65	260	0.0828	1.9	16.1
0.7	280	0.0781	1.5	15.6
0.75	300	0.0734	1.2	15.1
0.8	320	0.0688	0.9	14.6
0.85	340	0.0641	0.6	14.1
0.9	360	0.0594	0.4	13.6
0.95	380	0.0547	0.2	13.1
1.0	400	0.05	0	12.6

Fig. 4.11 Photograph of the blade and hub component (source: (Bahaj, Molland, et al., 2007))

The details of the blade root geometry that is clamped in the hub are shown in Fig. 4.11. It should be noted that there is a gap between the hub and each blade root, which will lead to a significant drop of circulation at the root. In this research, the hub and the circular cylinders, which connect the blades and the hub, are ignored.

In the experiment, the original test measurements were adjusted by the modified Glauert's equation(Barnsley & Wellicome, 1990) in order to include the blockage effect. The cavitation inception tests were also carried out for two hub pitch angles of 20^0 and 25^0, and the cavitation was observed under a strobe light and a video was recorded.

4.2.2 Performance predictions and wake geometries

4.2.2.1 Predictions of performance and wake geometry for the 0 yaw angle turbine-uniform inflow

The tested turbine geometry as that in the experiment was modeled by BEM, VLM and FLUENT. In these three methods, all the length scales were normalized by the radius of the blade R. In the BEM and VLM, the viscous effects are included via applying a friction coefficient C_f over the fully wetted blades. The definition of C_f will be described in Section 4.3.3.3.

Fig. 4.12 shows the geometry with 25^0 hub pitch from BEM. The 40×18 grid was adopted. In the chordwise direction, the 40 grids were not only for the pressure side surface but also for the suction side surface, i.e. 20 grids for each side. In the VLM, the same geometry was developed and the 20×18 grid was utilized since only the camber surface needed to be discretized in this method.

Fig. 4.13 shows the first four sections of the key blade at different radii. As is shown in Fig. 4.12, uniform spacing was utilized in the radial direction, and the cosine spacing was adopted for the chordwise direction, which can improve accuracy of the geometry by allowing more points around leading edge and trailing edge. The section profiles in Fig. 4.13 indicate the variation of the chord length and thickness, which were evaluated internally in BEM by interpolation. It should be noted that the skew and rake of the turbine blades are negligible and thus ignored in this research. The zero skew turbine and the straight leading edge turbine (for which small non-zero skew and rake have to be considered) were analyzed by PROPCAV and the results were found to be practically identical to each other.

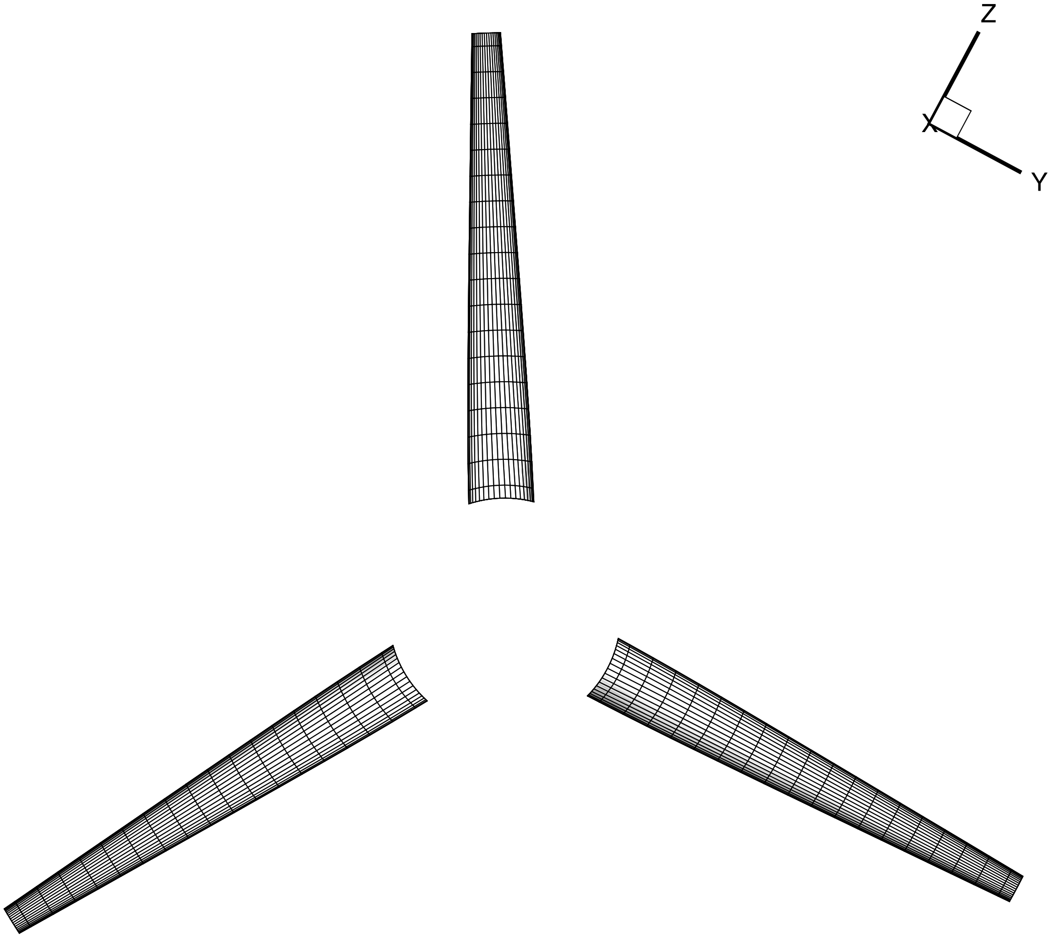

Fig. 4.12 Blade geometry modeled by boundary element method

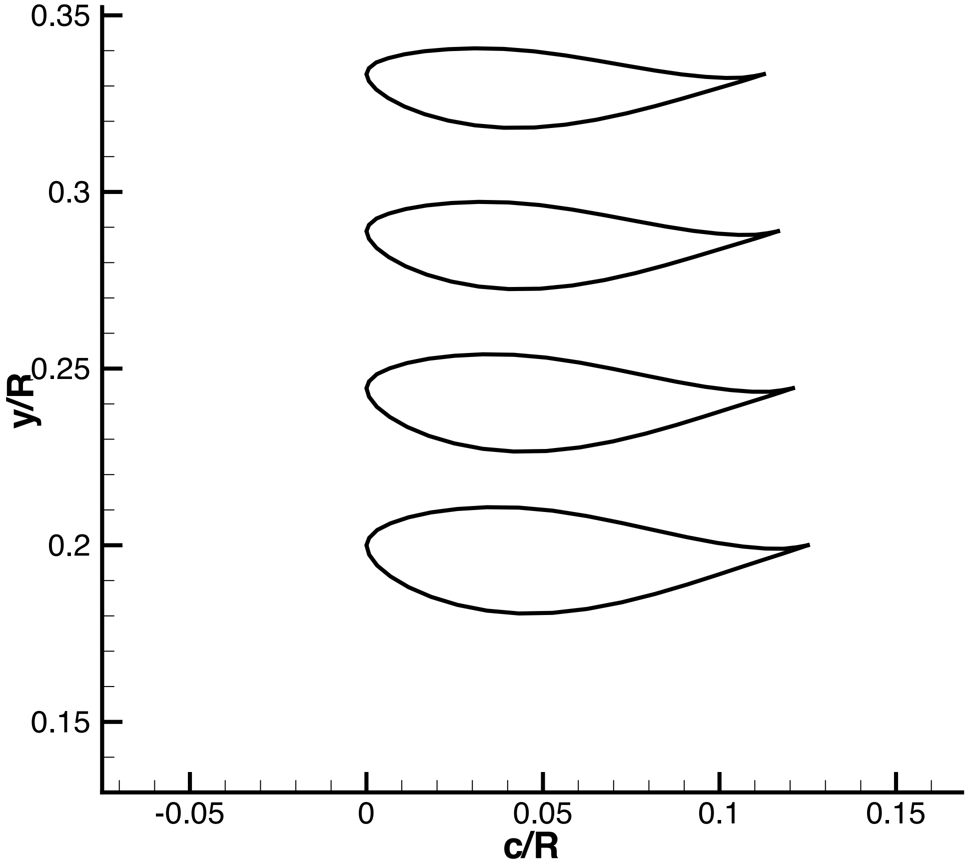

Fig. 4.13 First 4 blade sections from the boundary element method

In FLUENT, the geometry of the blade is imported from BEM, which ensures that a same blade as those in two potential methods (VLM and BEM) is analyzed. The turbine was located at x=0, within a domain ranges from x=-5R to x=5R, where 5R is the radius of the domain, R is the turbine radius. In order to reduce the number of cells and to save running time, only 1/3 of the total domain was meshed, and the periodic condition was applied on the two side faces. Fig. 4.14 and Fig. 4.15 show the mesh of the flow domain and the blade in the FLUENT, respectively. It should be noted that the y^+ that corresponding to this turbine grid is within the range of 30 to 100, except for small areas on the root and tip parts where it is smaller than 30.

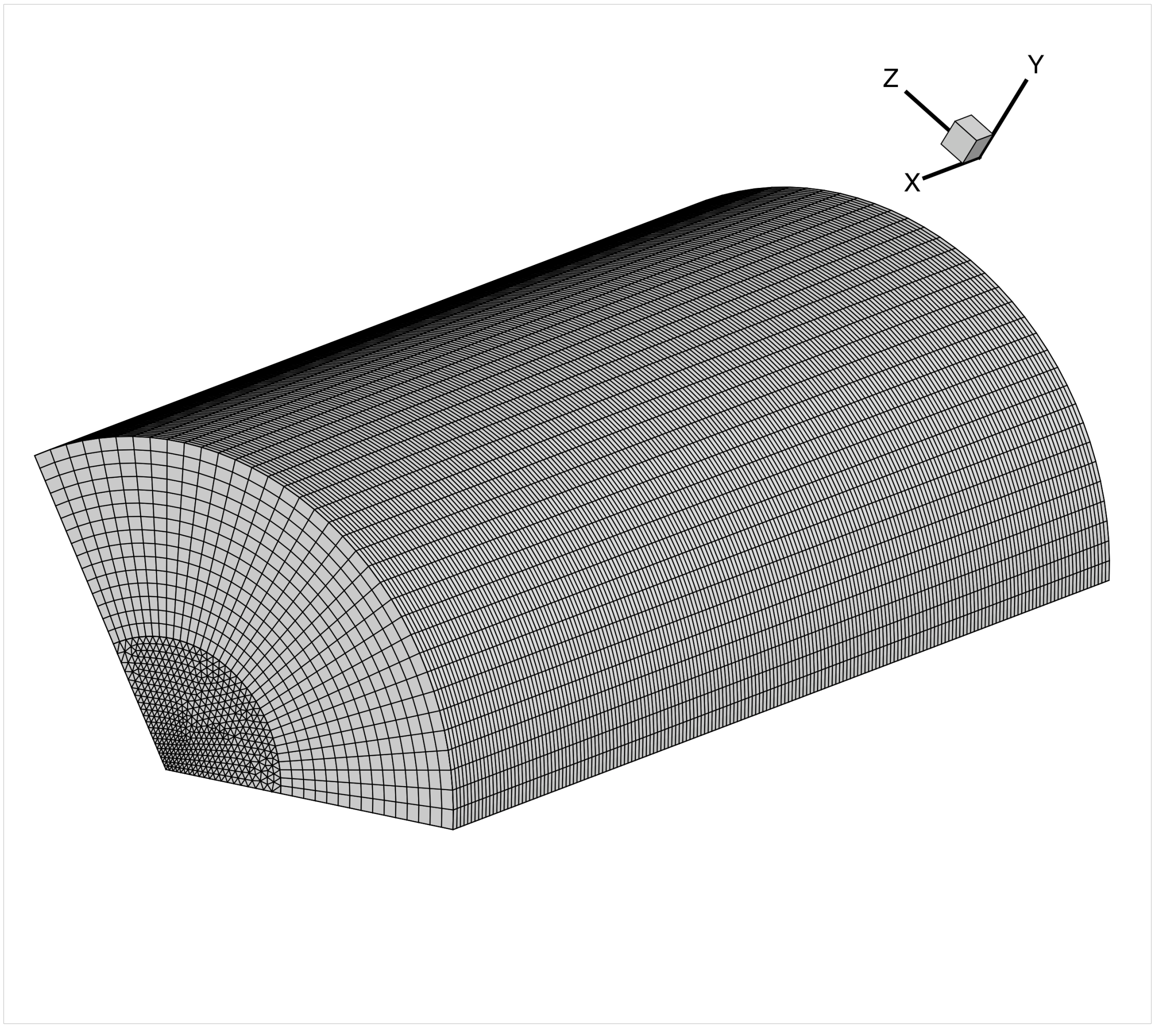

Fig. 4.14 Geometry and mesh of the fluid domain in the FLUENT.

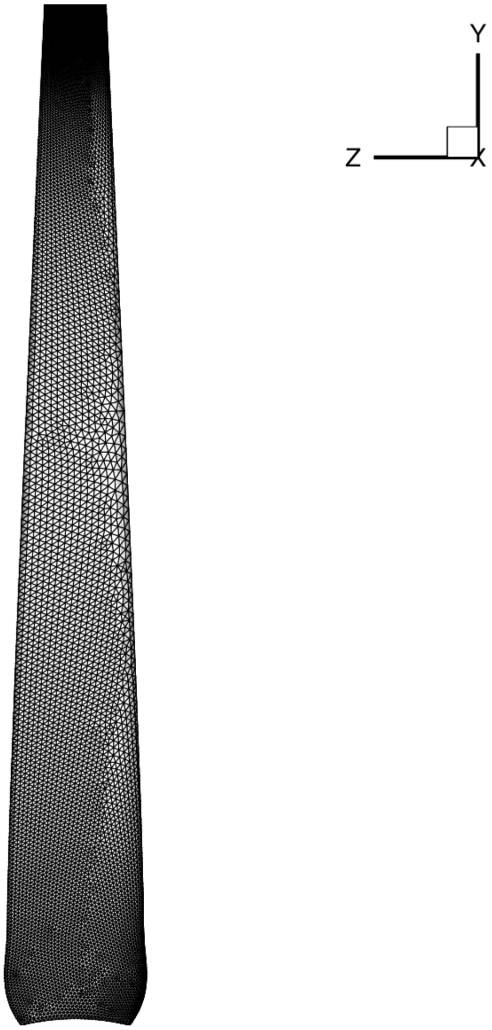

Fig. 4.15 Geometry and mesh of the turbine blade in FLUENT (Notice that the root part of the blade in the FLUENT is extended (to the hub) for 0.02R with decreasing chord length and thickness distributions)

Numerical predictions from PROPCAV, MPUF-3A and FLUENT are compared with experimental data for a turbine with a hub pitch angle (ϕ) of 25 degrees operating at different tip speed ratios ($TSR=\omega R/V$). V is the mean inflow velocity defined at the hub axis, $\omega=2\pi n$ is the turbine angular frequency, and $R=D/2$ is the turbine radius. Comparisons of the predicted thrust coefficient ($CT=T/0.5\rho V^2A$) and power coefficient ($C_{pow}=Q\omega/0.5\rho V^3A$) are shown in Figs. 4.16 and 4.17, where $A=\pi R^2$ is the turbine sweep area, *T* is the flow generated thrust. All three methods reasonably predict the performance of turbines within reasonable accuracy. The FLUENT has a better prediction for high *TSR* (=8), while the results from PROPCAV and MPUF-3A are better when compared with the experimental measurements for design *TSR* (5≤*TSR*≤6). The predictions of the performance for the same turbine operating at 27 and 30 degrees hub pitch, which are not shown on these two figures, also compared well with the experimental measurements. It should be noted that the computational time for PROPCAV and MPUF-3A is less than 3 minutes on one node, which is much less than the time needed for FLUENT (5 hours) on 16 nodes. One node has two 2.4 GHZ quad-core 64-bit Intel Xeon processors with 16 GB Memory.

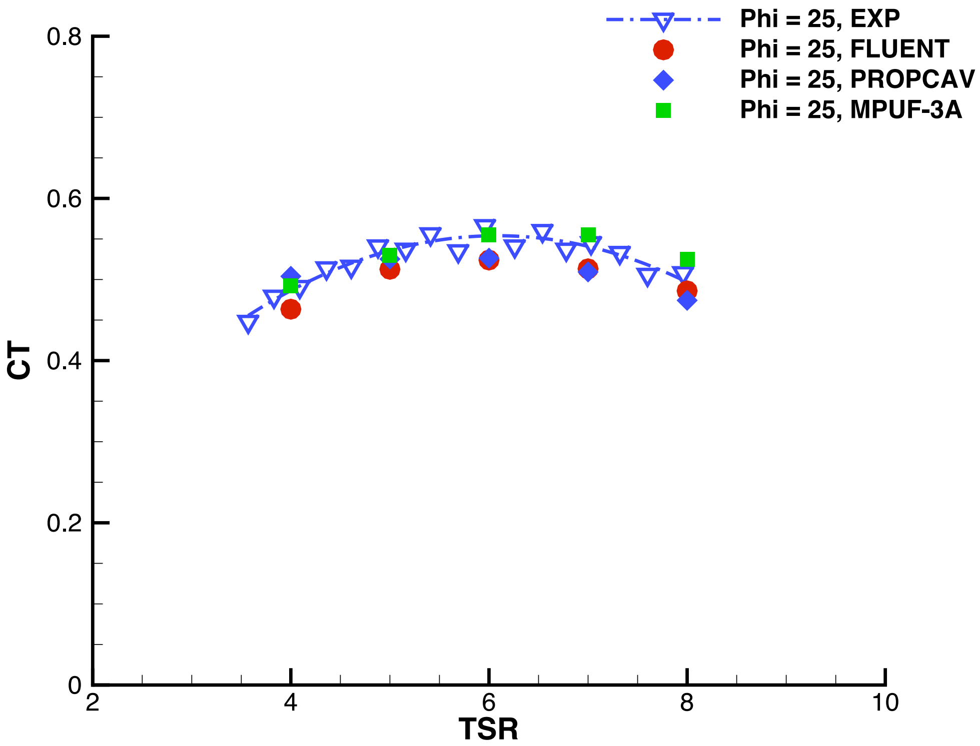

Fig. 4.16 Comparison of thrust coefficient (*CT*) from different numerical methods with the experimental measurements

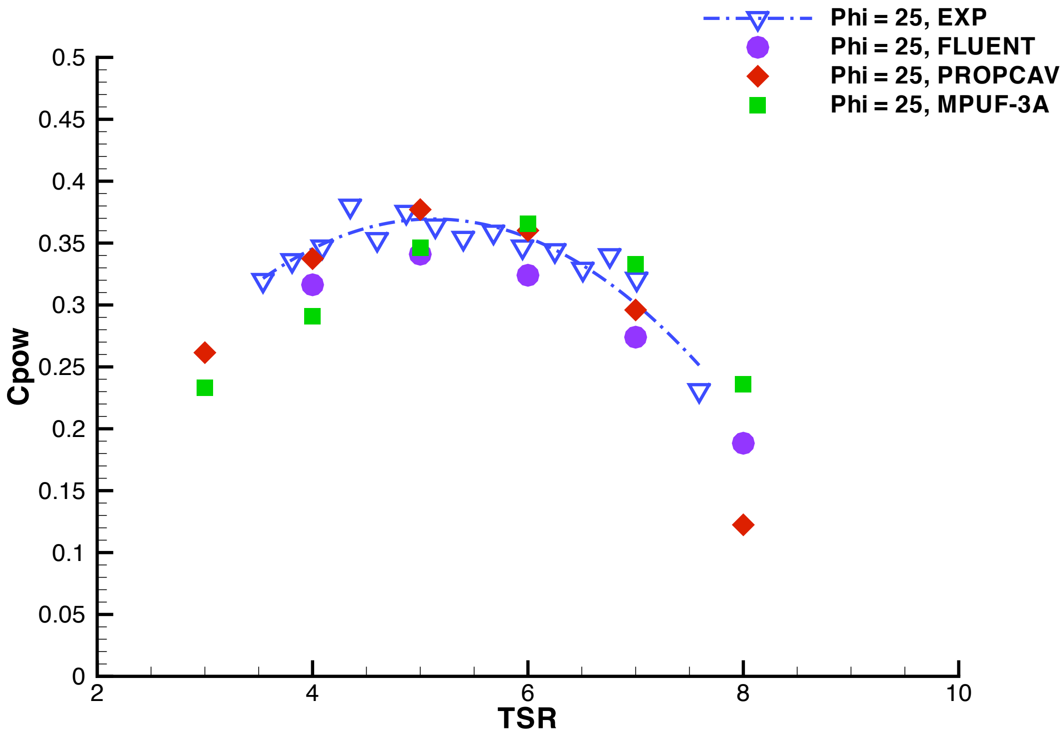

Fig. 4.17 Comparison of power coefficient (Cpow) from different numerical methods with the experimental measurements

It should be noted that in FLUENT, the flow in the domain is modeled with rotating reference frames, and the turbulence model is *k*-ω, SST. The Reynolds number in this case is $Re = VD/\nu = 1.445\times10^6$. The total cell number for the 1/3 domain is about 930,000.

As is mentioned in Chapter 3, having the correct trailing wake location is crucial in accurately predicting the thrust and the power coefficients. In the BEM, the geometrical pitch wake alignment is adopted and the ultimate wake radius is assumed to be *1.2R,* in order to model the wake expansion effect. Nevertheless, the roll up effect cannot be modeled in this simplified wake alignment method. The wake geometry from BEM is shown in Fig. 4.18 for the modeled turbine operating at *TSR*=6.0. In the VLM, the unsteady wake alignment method is used, in which the wake geometry is determined by applying the force free condition (L. He, 2010). It takes 5 iterations for the wake adjustment to converge. The final converged wake alignment for *TSR*=6.0 is shown in Fig. 4.19. The same wake geometry from VLM of the y-z plane view is also shown in Fig. 4.20. It should be noted that the contour of these three figures indicates the z coordinate, which can help make the wake geometry visible.

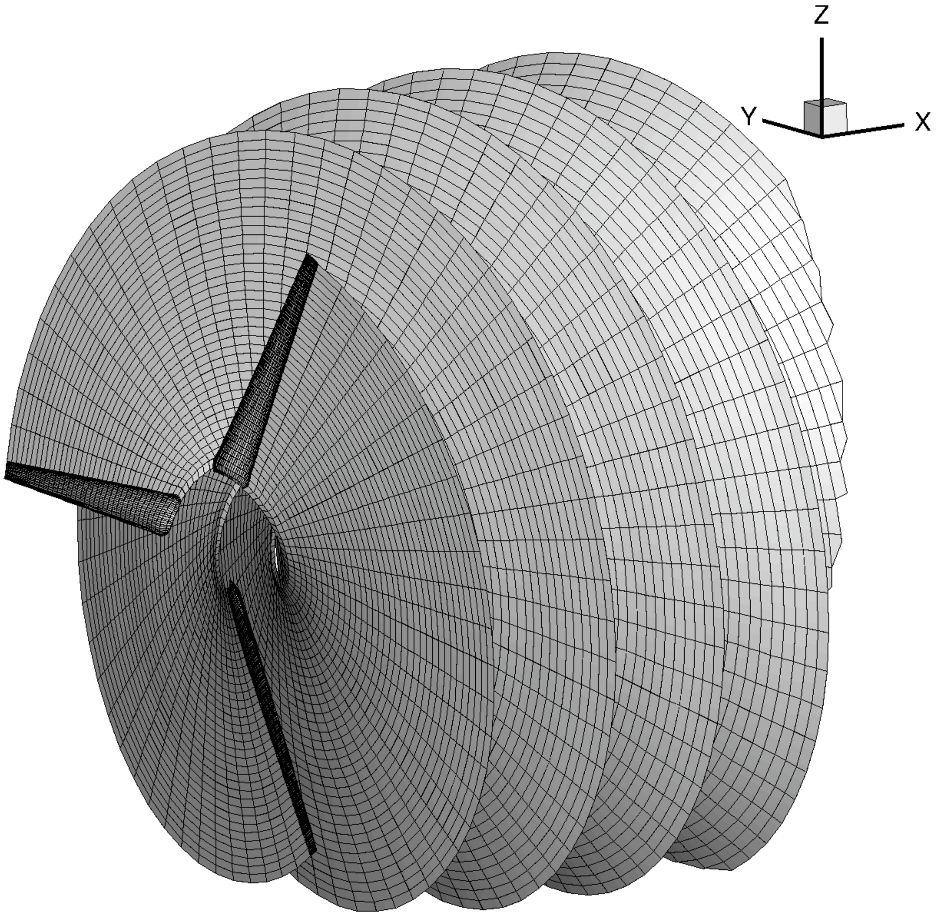

Fig. 4.18 Wake geometry from BEM using blade pitch wake alignment (*TSR*=6.0)

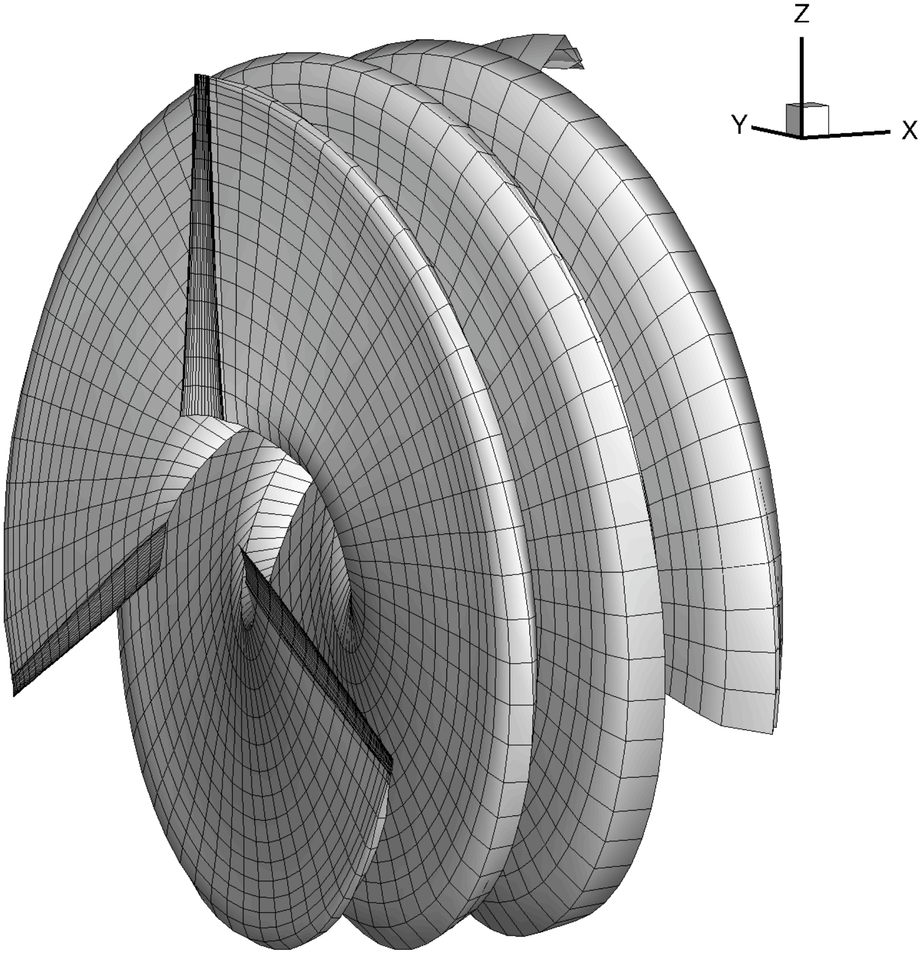

Fig. 4.19 Converged wake geometry from VLM using unsteady wake alignment (*TSR*=6.0).

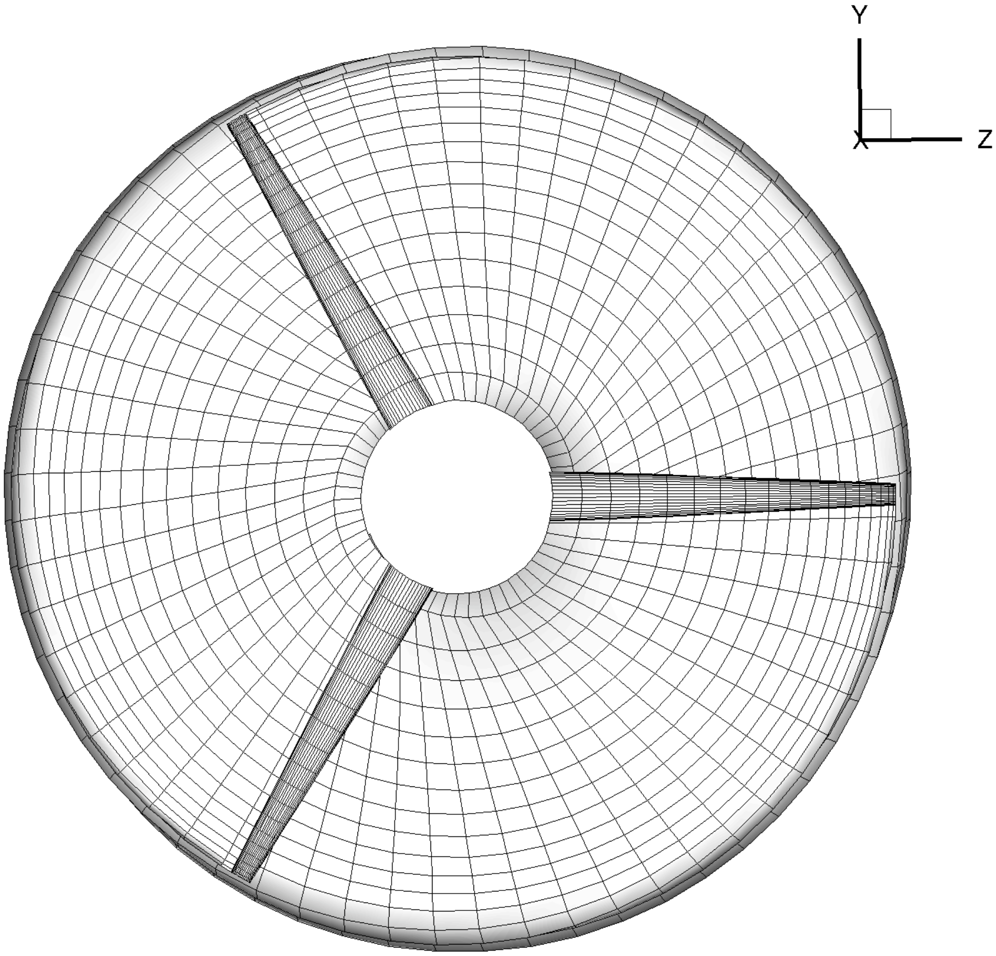

Fig. 4.20 y-z view of the final converged wake geometry from VLM using unsteady wake alignment (*TSR*=6.0).

Blade pitch wake alignment is an approximation of the turbine wake. It turns out that this wake alignment method can make a good prediction of the turbine performance in this research. As is mentioned in Chapter 3, the accuracy of wake approximations is dependent on the turbine operating conditions and specific blade geometries. Therefore, a simplified technique, like blade pitch wake alignment, may not work well for other cases. On the other hand, the unsteady wake alignment that can automatically adjust the wake geometry, and should work better in predicting the location of the wake in other cases. As shown in Fig. 19 and Fig. 20, both the wake roll up phenomenon and the expansion effect can be predicted by this wake alignment.

In FLUENT, the wake geometry in Fig. 4.21 is presented by streamlines. A full domain analysis case is carried out in order to investigate the wake geometry. Fig. 4.22 shows a streamline of the flow passing the tip point, which clearly indicates the expansion effect. In Fig. 4.23, streamlines around the blade tip part are shown, and the tip roll up phenomenon is detected.

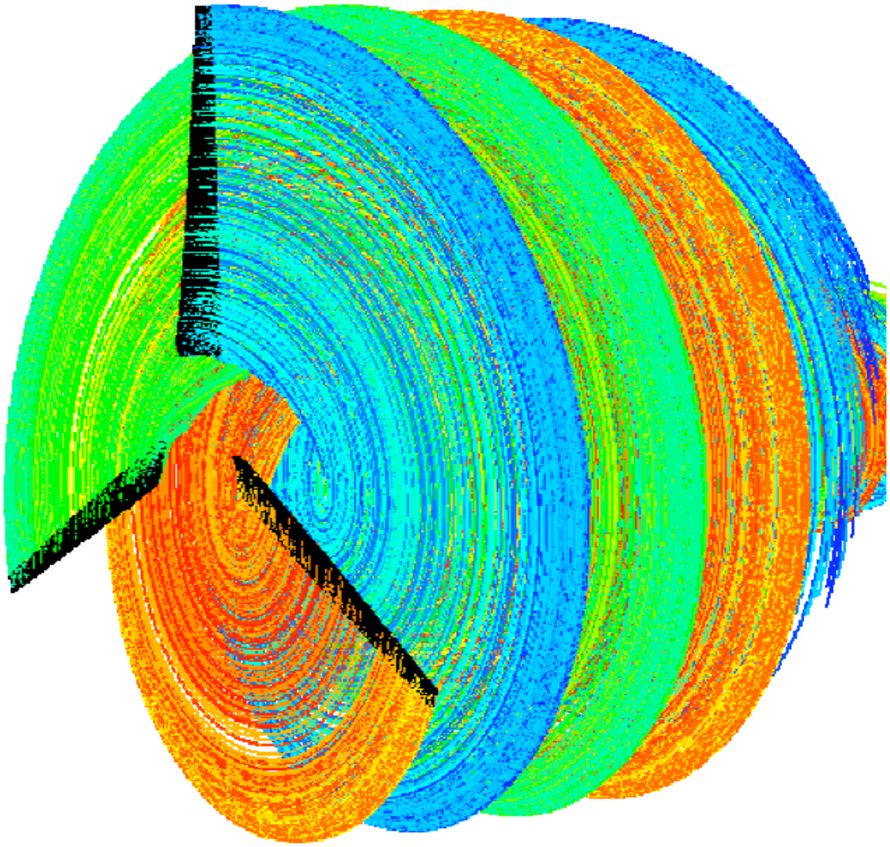

Fig. 4.21 Wake geometry from FLUENT (visualized by streamlines)

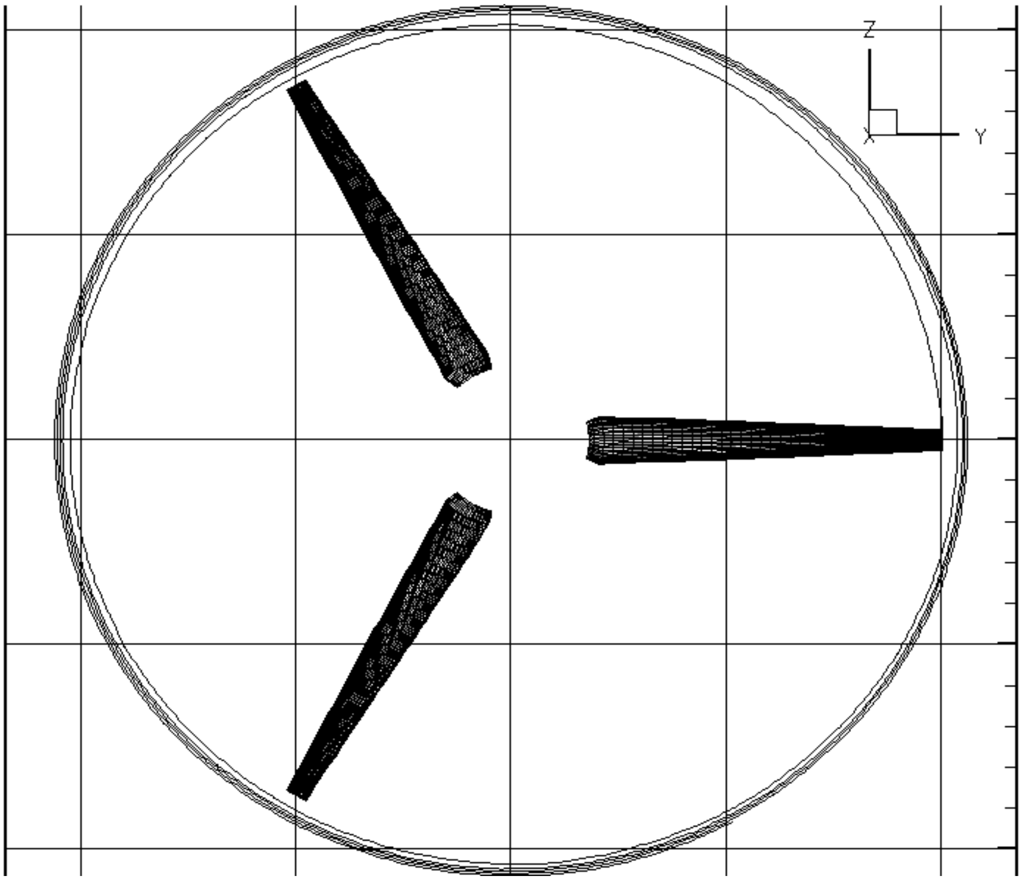

Fig. 4.22 A Tip streamline from FLUENT viewed in a *y-z* plane (wake expansion effect)

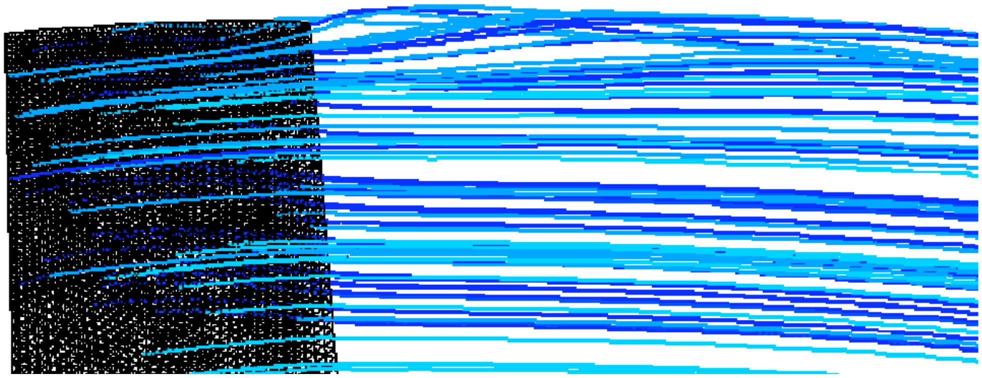

Fig. 4.23 Streamlines around the tip part viewed in a *y-z* plane (tip roll up phenomenon is observed)

The turbine performances, K_T and K_Q, are actually the integration of the pressure force on the blade pressure side and suction side. The pressure coefficients C_p (=(P-P_0)/0.5$\rho n^2 D^2$) on the turbine surface that are predicted by FLUENT and BEM are investigated, and the results at three sections (Y=0.3, Y=0.5, Y=0.8) are compared in Fig. 4.24 ~ 4.26. As can be found in these three figures, the pressure coefficients between FLUENT and BEM are close to each other when Y is small. As Y becomes larger, i.e. approaches the tip, the BEM results have greater pressure jump on the blades, which leads to a relatively higher power coefficient (see Fig. 4.17).

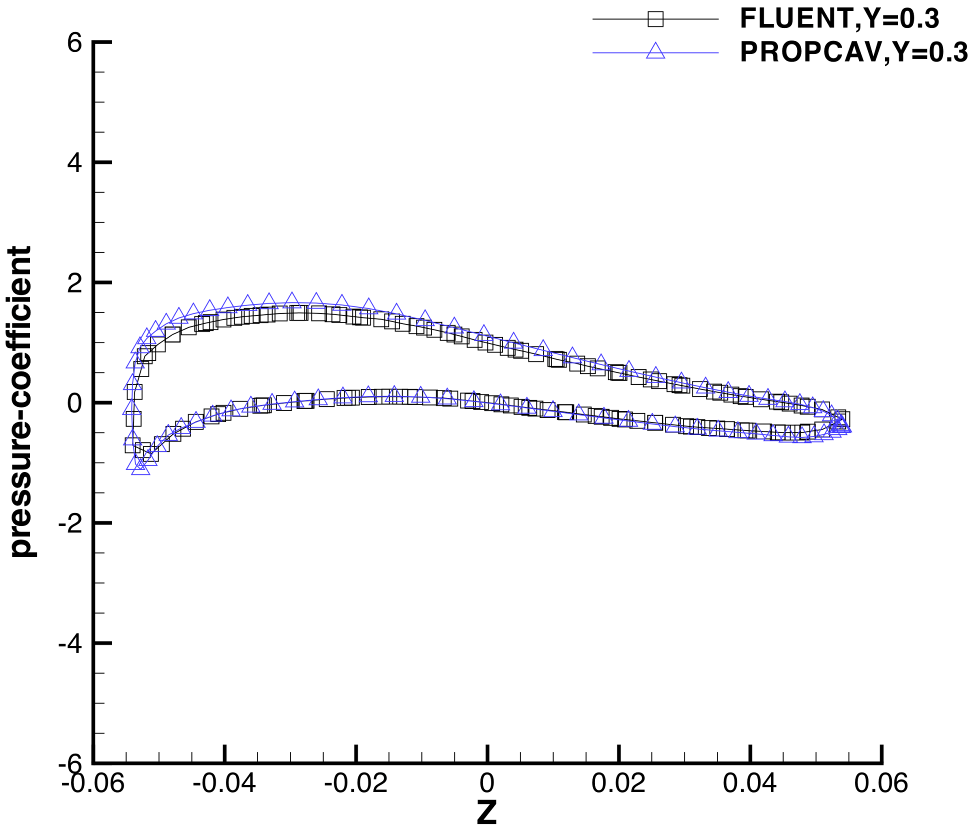

Fig. 4.24 Comparison of Pressure coefficients (C_p) at Y=0.3 between FLUENT and PROPCAV (*TSR*=6.0, 25^0 hub pitch and 0^0 yaw angle).

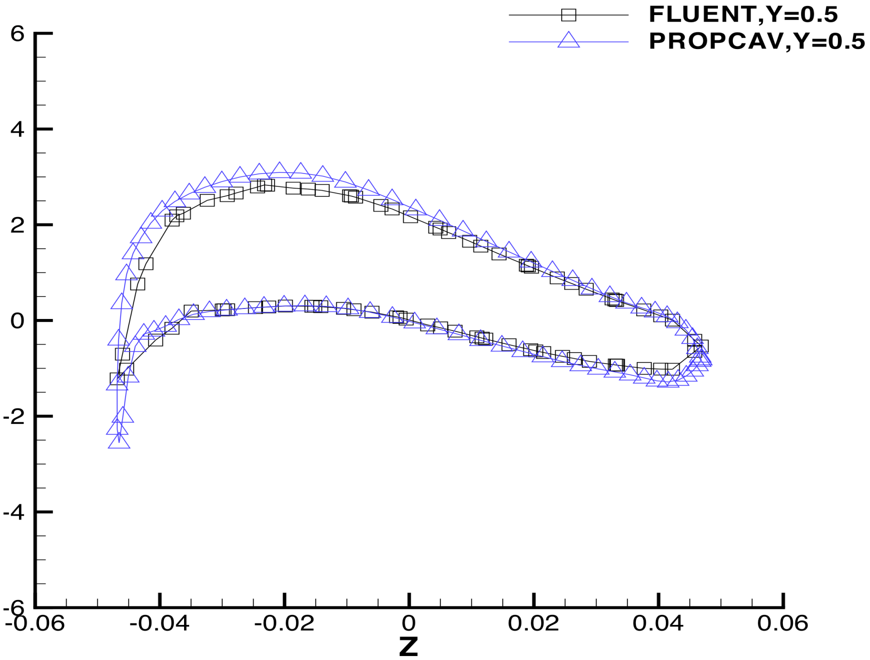

Fig. 4.25 Comparison of Pressure coefficients (C_p) at Y=0.5 between FLUENT and PROPCAV (*TSR*=6.0, 25^0 hub pitch and 0^0 yaw angle).

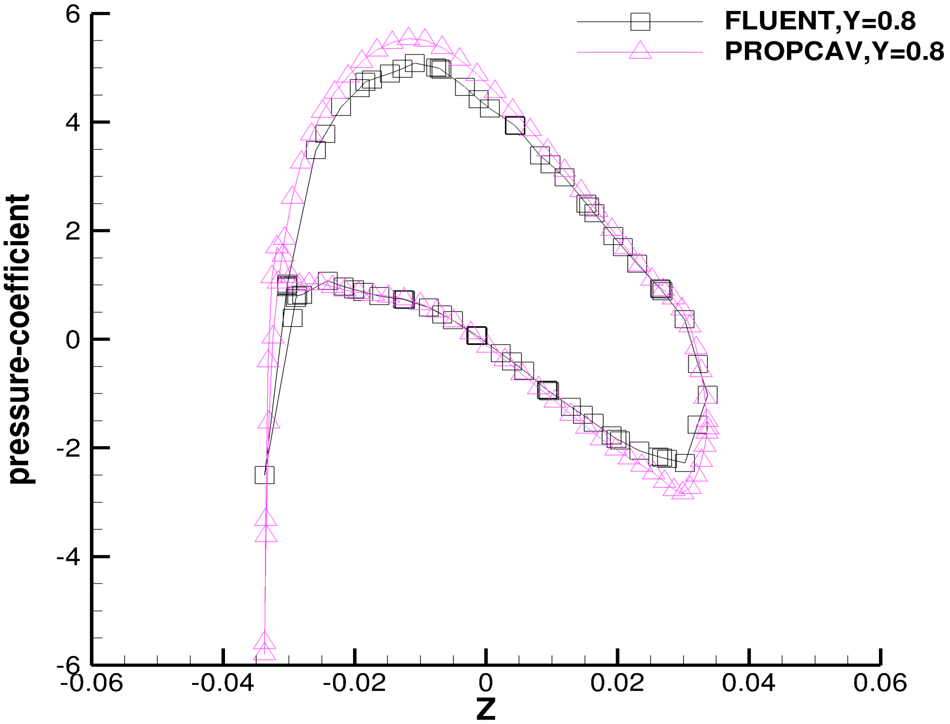

Fig. 4.26 Comparison of Pressure coefficients (C_p) at Y=0.8 between FLUENT and PROPCAV (*TSR*=6.0, 25^0 hub pitch and 0^0 yaw angle).

4.2.2.2 Predictions of performance and wake geometry for the turbine with non-zero yaw angle

In this research, the influence of inflow yaw angle on turbine performance is also investigated by vortex lattice method MPUF-3A. The yaw angle for a marine current turbine is the angle between the inflow velocity and the turbine hub axis in the horizontal plane (shown in Fig. 4.27). An inflow wake file with a yaw angle with respect to the turbine axis is specified and the unsteady wake alignment method is utilized in MPUF-3A. Two yaw angle cases (15^0 and 30^0 yaw angles) are analyzed and the performance of turbine operating at different *TSR*s are shown in Fig. 4.28 and Fig. 4.29, respectively. Also shown in these two figures are the experimental results from (Bahaj, Molland, et al., 2007). As can be found in Fig. 4.29, the power coefficients for the turbine subject to inflow with a yaw angle can be accurately predicted by MPUF-3A. Nevertheless, in Fig. 4.28, the thrust coefficients predicted by MPUF-3A are higher than the experimental results for high *TSR*s. As is mentioned above, the final converged wake geometry is crucial to the turbine performance predictions. Fig. 4.30 and Fig. 4.31 show the wake geometries of the turbine (*TSR*=6.0) with an inflow angle equal to 15^0 in *yz* and *xz* planes, respectively. The converged wake also has an angle with respect to the turbine hub axis.

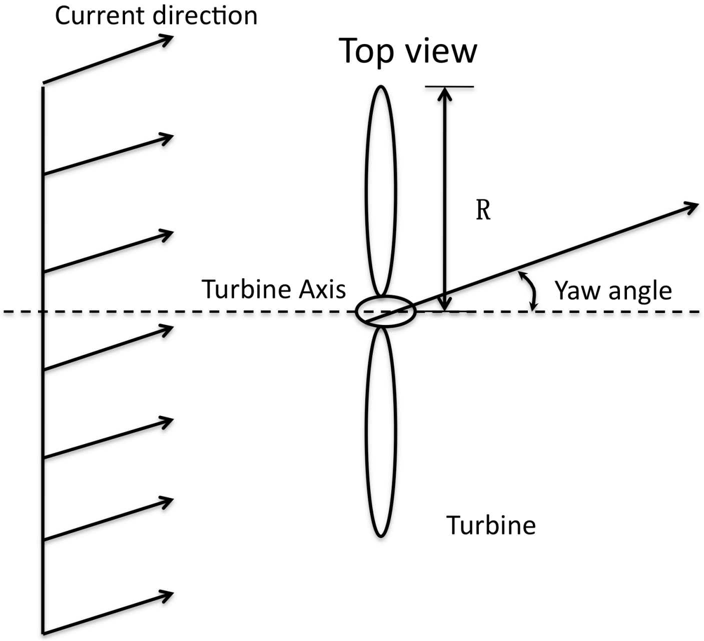

Fig. 4.27 Definition of yaw angle for the marine current turbine

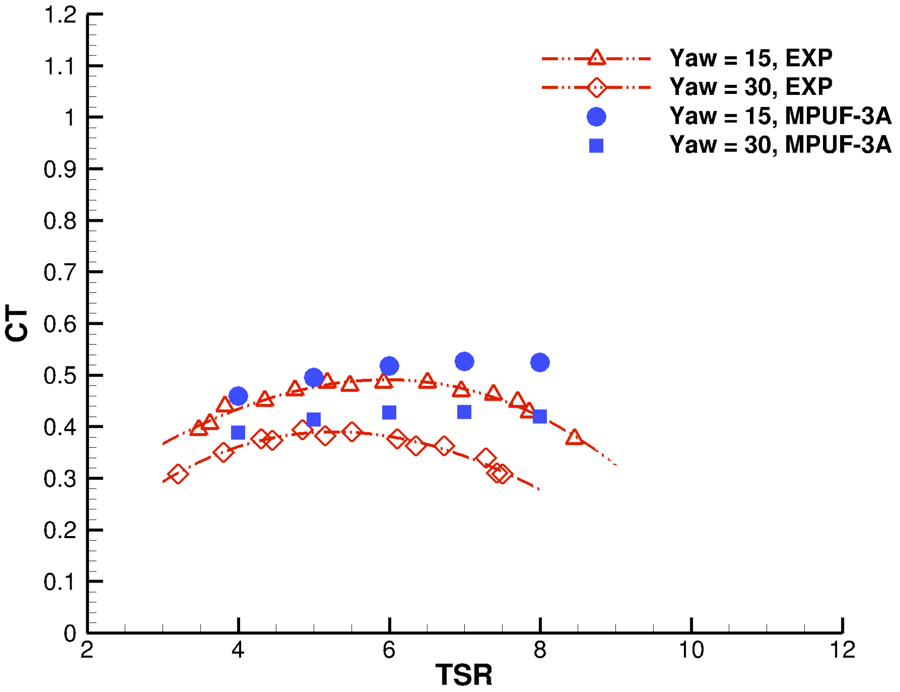

Fig. 4.28 Comparison of thrust coefficient (*CT*) from MPUF-3A at different inflow yaw angles (15^0 and 30^0) with the experimental measurements

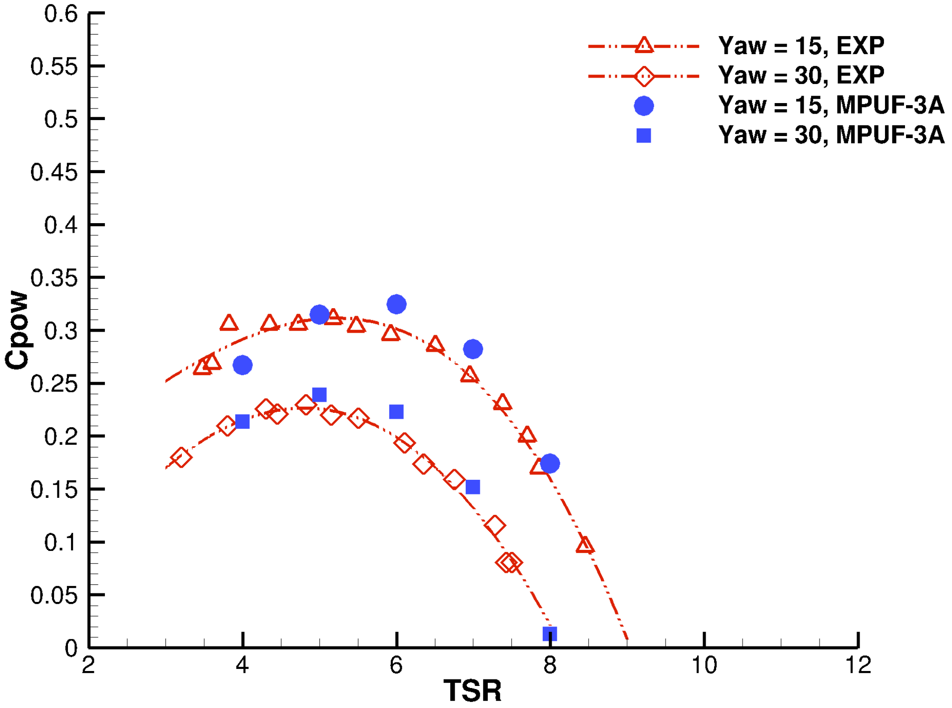

Fig. 4.29 Comparison of thrust coefficient (C_{pow}) from MPUF-3A at different inflow yaw angles (15^0 and 30^0) with the experimental measurements

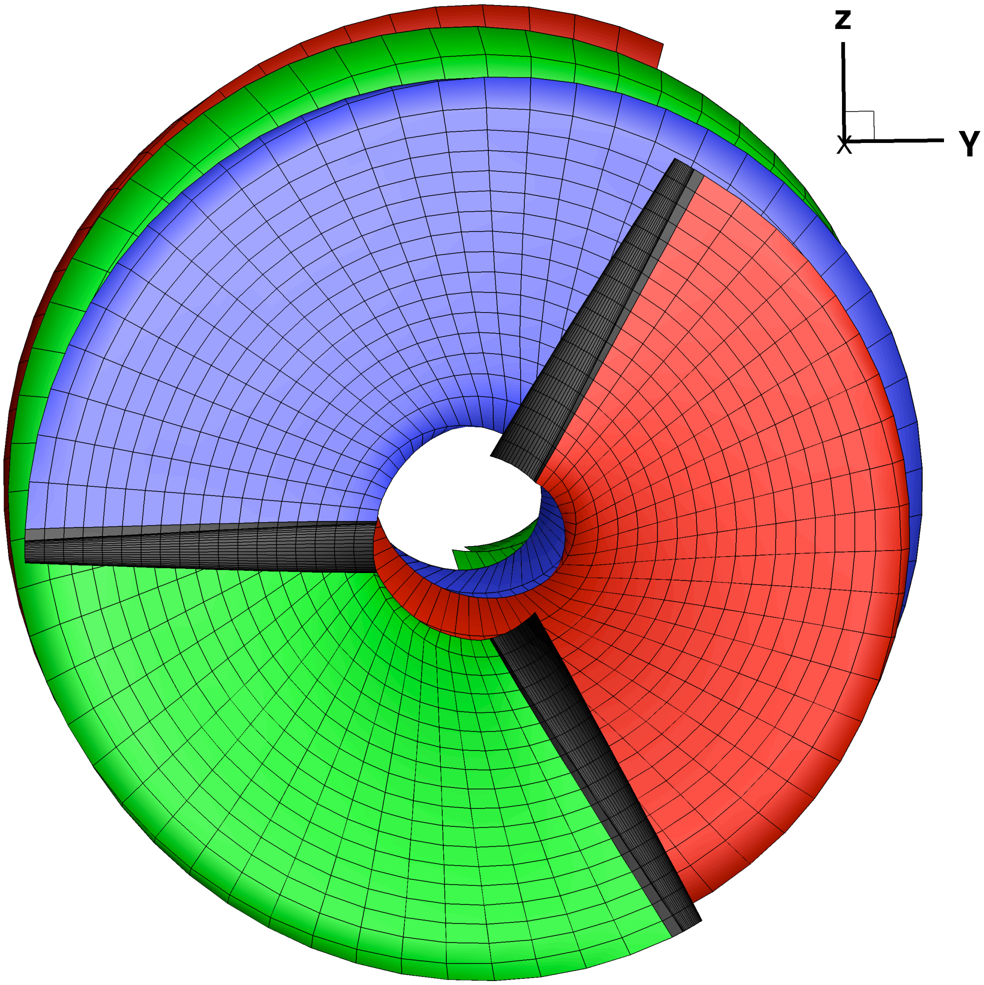

Fig. 4.30 Final converged wake geometry in yz plane for 15^0 yaw angle

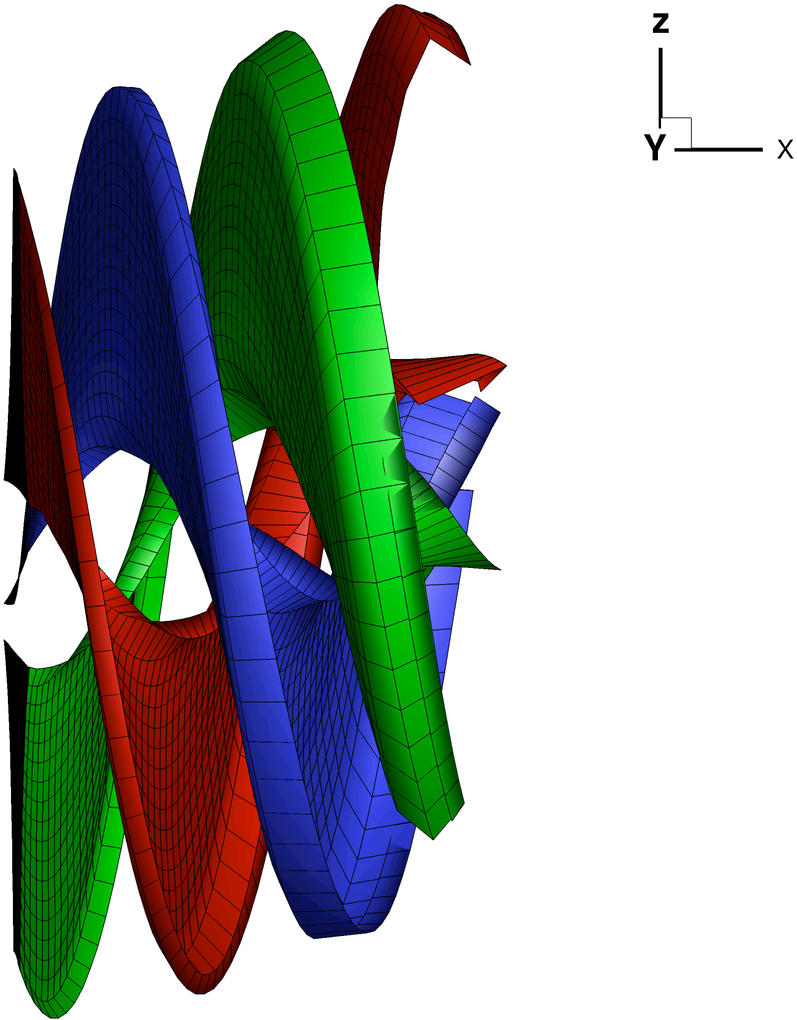

Fig. 4.31 Final converged wake geometry in xz plane with 15^0 yaw angle

4.2.2.3 Prediction of cavitation for the 0 yaw angle turbine-uniform inflow

When a large-scale tidal turbine with a large rotational speed is installed close to the water surface, cavitation will occur, which can have a significant effect on the turbine performance. In order to validate the predicted cavitation pattern, a cavitating turbine with a 25^0 hub pitch and 0^0 yaw angle operating at TSR=7.5 has also been investigated via using the boundary element method. The static pressure of the cavitation tunnel is P_0=23,000Pa and the vapor pressure of water at 100^{0}C is P_v=1,230Pa. Thus the cavitation number defined at the axis of rotation is σ_n=3.9 ($CPMIN$=3.9). A photo of a cavitating turbine from the experiment, operating at TSR=7.5 and σ_n=3.9 is shown in Fig. 4.32. Fig. 4.33 shows the predicted cavity pattern and pressure contour for the turbine model with same working conditions. As shown in these two figures, the boundary element method can correctly predict the cavity pattern for a tidal turbine.

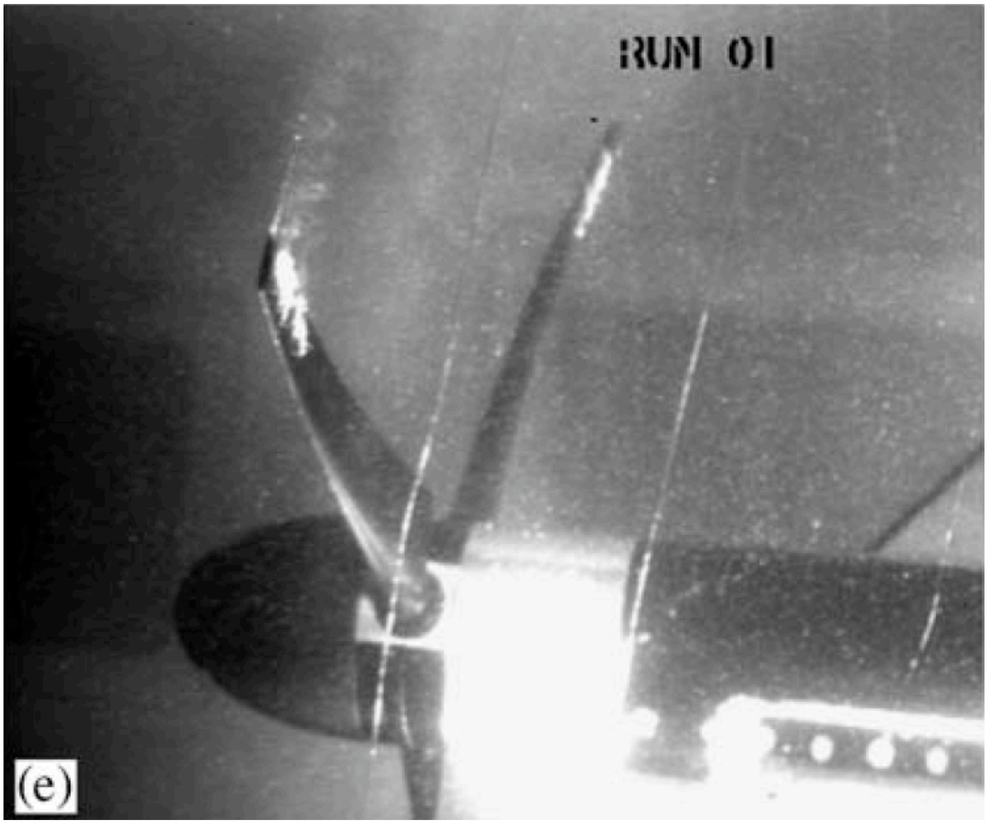

Fig. 4.32 The cavity pattern of the model turbine in the experiment (TSR=7.5 and σ_n=3.9), from (Bahaj, Molland, et al., 2007)

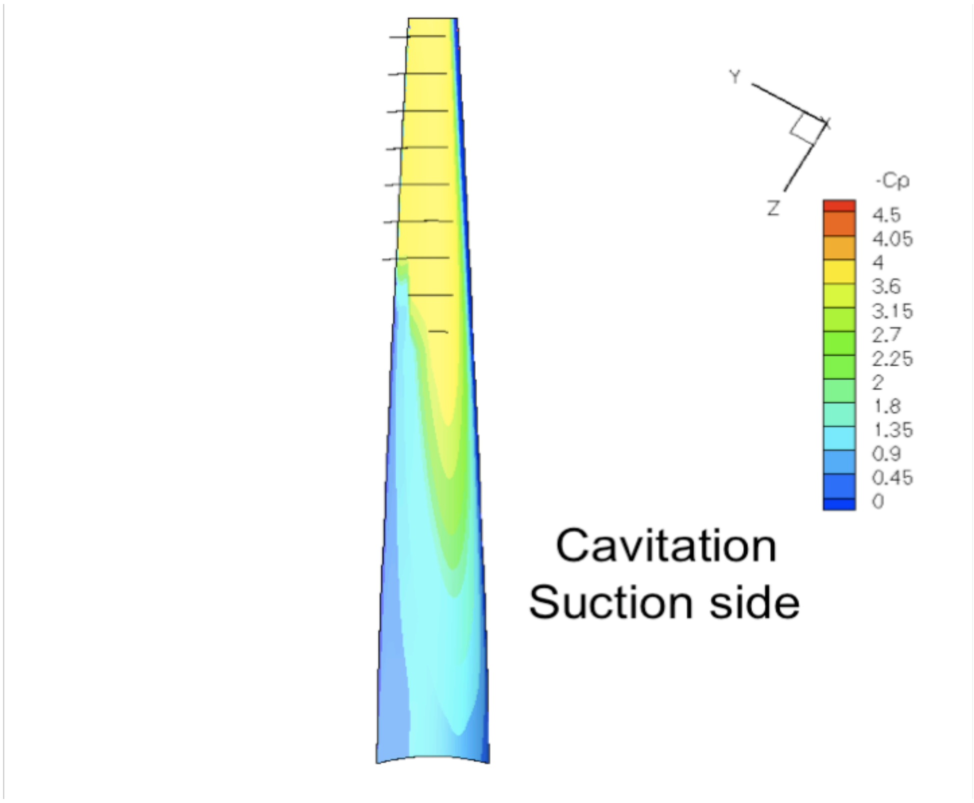

Fig. 4.33 Pressure contour and cavity patterns for a same turbine (*TSR*=7.5 and σ_n=3.9)

4.2.3 Marine current turbine subject to non-uniform current

The realistic inflow of a marine current turbine is not uniform (e.g. tidal boundary layer flow). The analysis of the performance is explored by adopting a viscous/potential flow method, which couples VLM with NS-3D. For a detailed design of a marine current turbine farm, measurements need to be taken for a particular site over a period of a month or more in order to produce accurate velocity profile data. Based on (Batten, et al., 2008), the tidal velocity profile at the inflow boundary, as shown in Fig. 4.34 and Fig. 4.36, can be approximated as:

$$U(y) = U_0\left(\frac{y+5R}{5R}\right)^{1/7} \tag{4.1}$$

where U_0 is the velocity at the hub axis, and y indicates the vertical position with the hub axis located at y=0 (shown in Fig. 4.34). The total tidal depth is assumed to be 10R. The inflow velocity contour is shown in Fig. 4.36. The turbine model is the same as the one used in the experiment with 25^0 hub pitch and 0^0 yaw angle. The 3-D mesh used in NS-3D, as shown in Fig. 4.35, is generated via using GAMBIT, and the total number of elements is about 300,000. The 5R radius cylindrical computational domain ranges from x=-5R to x=10R with the turbine locates at x=0. The effective wake is evaluated at x=-0.1R.

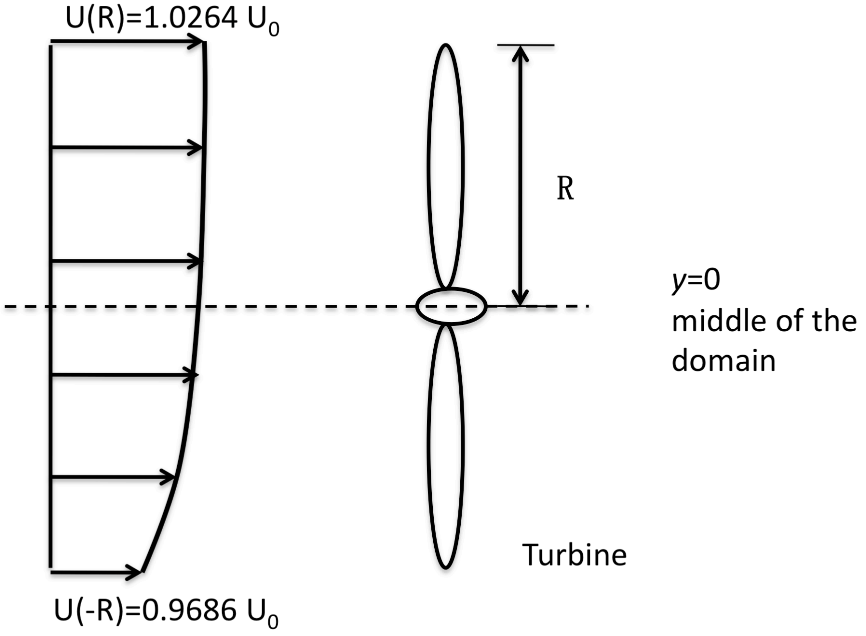

Fig. 4.34 Tidal profile and location of turbine in NS-3D

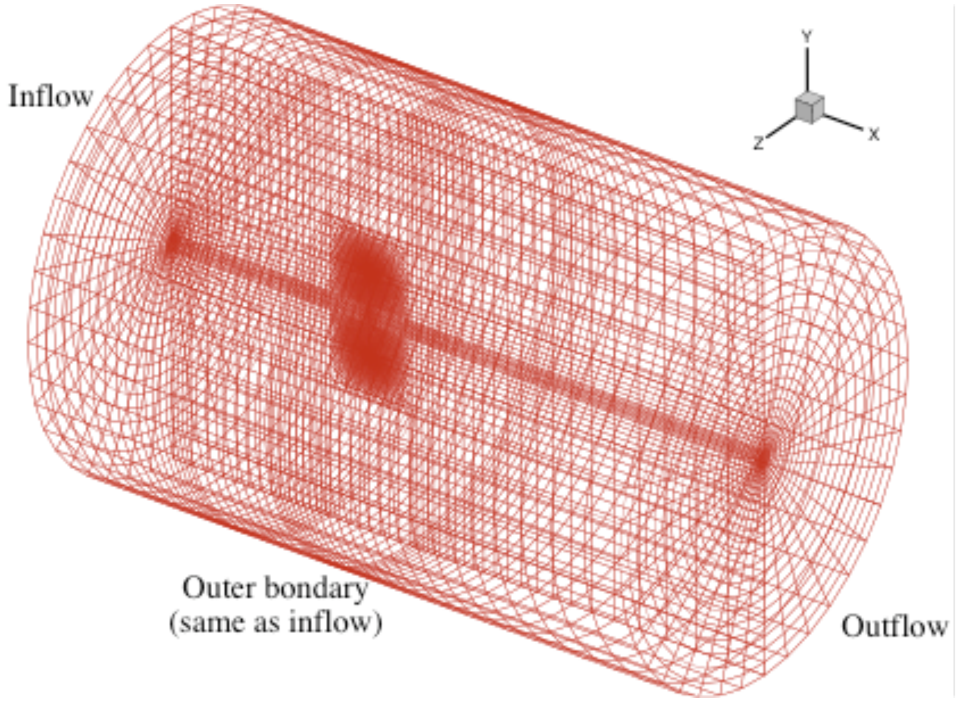

Fig. 4.35 Mesh of the computational domain of NS-3D

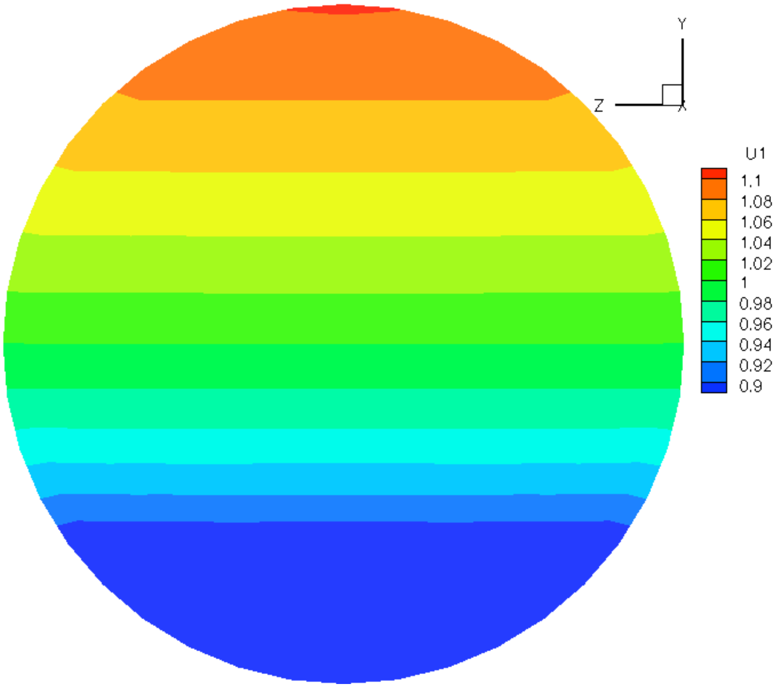

Fig. 4.36 Inflow velocity contour (x=-5.0)

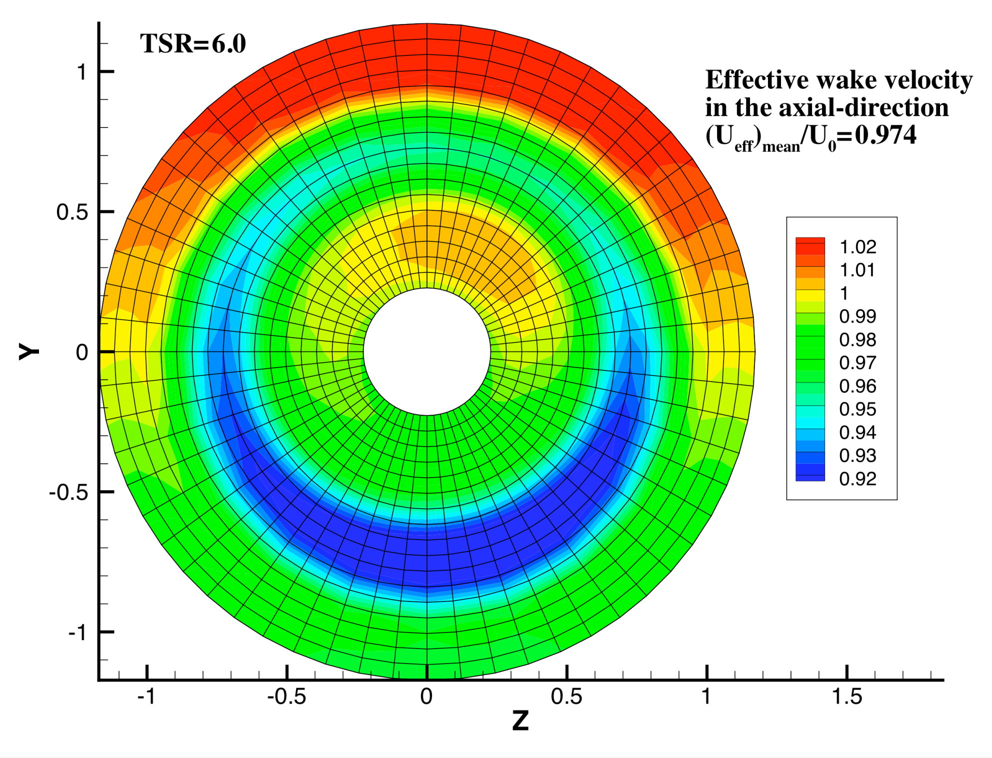

Fig. 4.37 Effective wake axial velocity contour (*x*=-0.1*R*) (The circumferential and radial views of the grid are also shown)

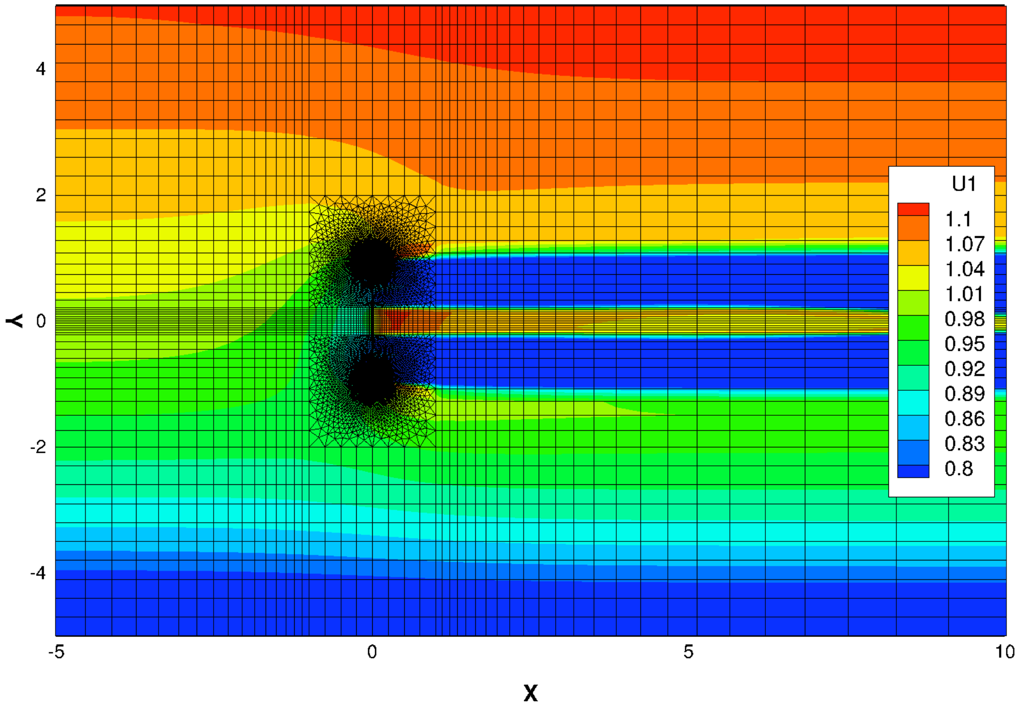

Fig. 4.38 Total axial velocity contour and grid at *xy*-plane when *z*=0 (the turbine is located at *x*=0).

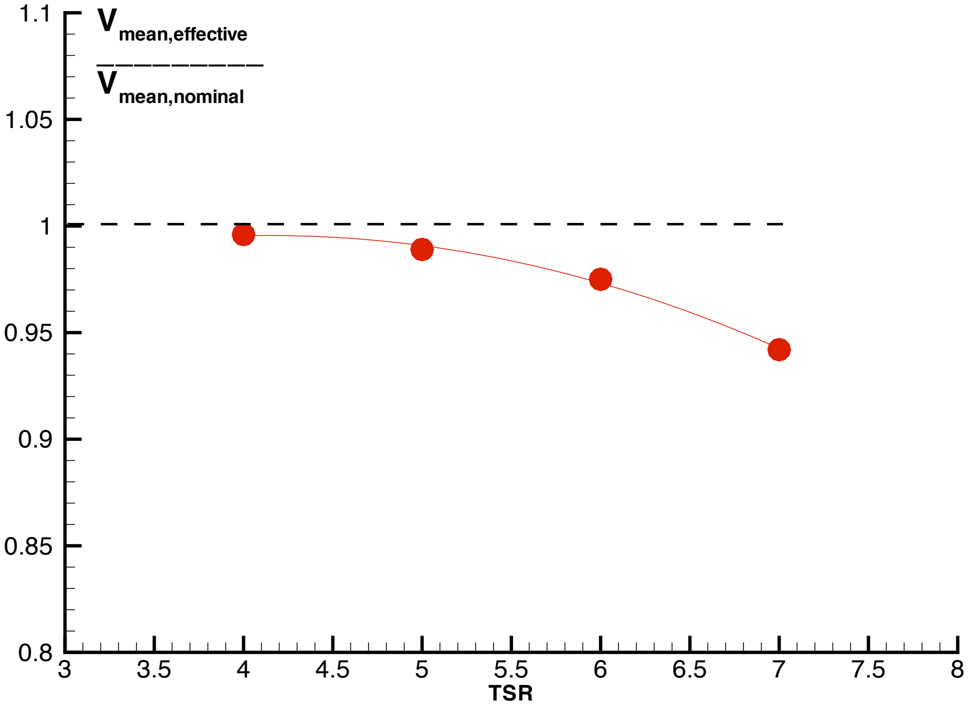

Fig. 4.39 Comparison of the effective mean velocity with the nominal mean velocity

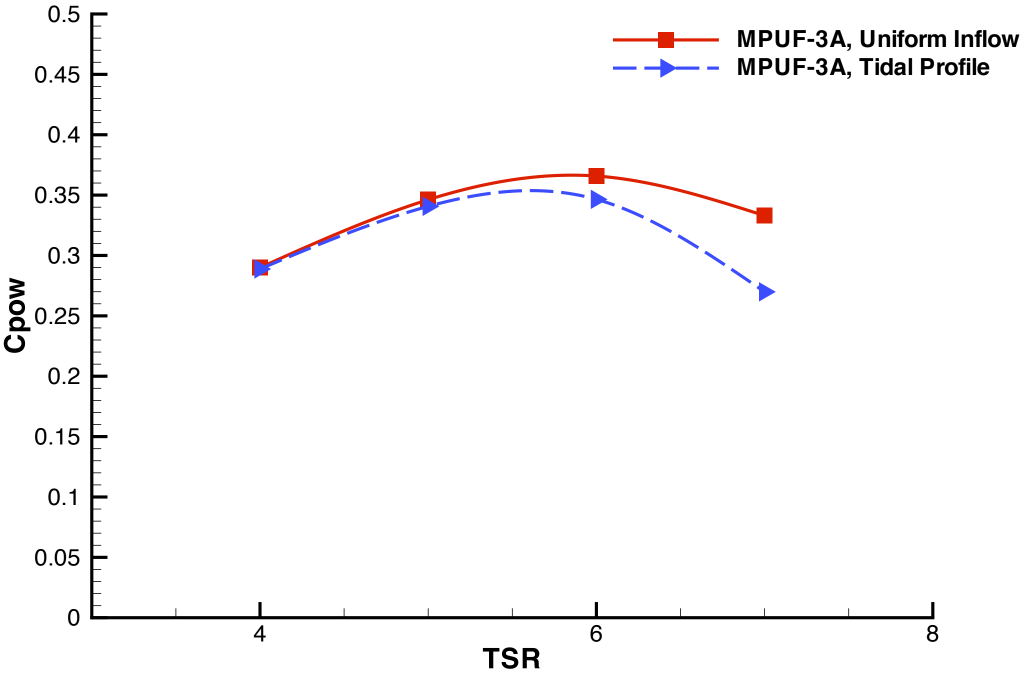

Fig. 4.40 Comparison of C_{pow} between uniform velocity case and tidal velocity case

Figures 4.37 and 4.38 plot the contours of the converged effective wake axial velocity at the effective wake plane and total axial velocity at *xy*-plane (*z*=0) when *TSR*=6.0. Also shown in Fig. 4.38 are the axial and radial views of the utilized grid. Both the total and effective wake axial velocities are not axisymmetric because of the non-uniform inflow. Due to the stronger interaction between the turbine and the flow filed, as shown in Fig. 4.39, the ratio of the mean velocity of the effective wake to that of the nominal wake decreases for larger *TSR*. The power coefficients for a range of *TSR*s are shown in Fig. 4.40. As a result of the reduction in the mean velocity of effective wake, the over all efficiency drops for a higher *TSR* when the turbine is subject to a tidal velocity profile. The coupling between MPUF-3A and NS-3D converges after 5 iterations, and NS-3D requires 800 iterations (steady-flow simulation) in total to achieve a converged solution.

4.3 EXAMPLES OF BLADE DESIGN FOR TURBINES

4.3.1 Database-searching method (CAVOPT-BASE)

CAVOPT-BASE method, which couples PROPCAV and a nonlinear optimization method, is proposed for the rotor design in this research. A 20m diameter tidal turbine, suggested by a(Blunden & Bahaj, 2007), is used as an example here. Based on the power coefficient curve (Fig. 4.17) and the given tidal velocity data (Batten, et al., 2007), the suitable design *TSR* and design tidal speed range from 4 to 7 and 2m/s to 3m/s, respectively.

In this section, the turbine model in the experiment (Bahaj, Molland, et al., 2007) is chosen as a base turbine[3] and the three geometric parameters are

---

[3] The same spanwise thickness distribution as that of the experimental turbine model is maintained in the blade design

$$\begin{aligned}
&(P/D)_{design} = (P/D)_{base} \times x_1 \\
&(c/D)_{design} = (c/D)_{base} \times x_2 \\
&(Y_{p,s}/c)_{design} = (Y_{p,s}/c)_{base} \times x_3
\end{aligned} \qquad (4.2)$$

where P/D, c/D, and $Y_{p,s}/c$ represent normalized pitch, chord and blade offsets of the pressure or suction side, respectively. It should be noted that in order to keep the maximum thickness the same among different designs and not compromise the structural integrity of the turbine, we require that $x_3=1/x_2$. Therefore, only the parameters x_1 and x_2 are to be determined in the optimization.

4.3.1.1 Fully wetted turbine design

For the blade to be fully wetted, a constraint on *CPMIN* must be applied. Namely, as described in section 3.6, $CPMIN \leq \sigma_n$. In the present case, we assume that σ_n is high enough that cavitation is not an issue. Thus, we do not activate the *CPMIN* constraint. In this research, a case with TSR=5.0 and the tidal velocity U=2.5m/s is investigated. Thus the turbine rotational frequency is n=0.24rev/s. The *CT* and C_{pow} for the original geometry are 0.55 and 0.39, respectively. In this case, only the pitch and chord length are selected as the geometric parameters to produce a performance database. The thickness of the blade is kept the same for all geometries. The two multipliers (x_1 and x_2), which correspond to pitch and chord length, range from 0.80 to 1.2 and 0.8 to 1.2. The design results are C_{pow}=0.412 and CT=0.586 when x_1=0.803 and x_2=1.006. The maximum $-Cp$ (C_{Pmin}) for the design geometry is 7.78, which is very close to the value (7.26) of the original geometry. Both C_{pow} and *CT* increase in this design. Thus there is clearly a balance between the extra costs of the support structure (larger *CT*) and the extra power (larger C_{pow}) that can be generated. It should be noted that the database size is rather limited in this design case, and a better geometry may be found if a larger database is used.

4.3.1.2 Cavitating turbine design

For the larger size turbines that have shallow tip immersion, cavitation may become a serious issue. The design method CAVOPT-BASE can also be used to reduce or eliminate the cavitation by adjusting the geometric parameters of a certain turbine. In this research, two cavitating cases are investigated and the same numerical turbine model as that in the experiment (Bahaj, Molland, et al., 2007) is used.

Cavitating Case 1

A 25^0 hub pitch and 0^0 yaw turbine operates at TSR=5.0 with cavitation number σ_n equal to 5.0. The pressure distributions of different blade sections are shown in Fig. 4.41. The x coordinate is the ratio of section point locations with respect to the section chord length. Thrust coefficient and power coefficient are CT=0.486 and C_{pow}=0.317, respectively. As shown in Fig. 4.41, cavitation occurs on part of the blade. The cavitation pattern for this case is close to what is shown in Fig. 4.33. The pitch and chord length are also selected as the two geometric parameters to produce a performance database. The ranges of the two multipliers are $1.0 \le x_1 \le 1.2$ and $0.8 \le x_2 \le 1.5$. In order to eliminate the cavitation, the inequality constraint $C_{Pmin} \le 5.0$ is applied in the optimization problem. The design result from CAVOPT-BASE is CT=0.516 and C_{pow}=0.371 when x_1=1.006 and x_2=1.351. In this database, the optimal geometry, which satisfies all the constraints, is the one with a longer chord length and almost the same pitch. The pressure distributions of the designed turbine at different sections are shown in Fig. 4.42. It is noted that cavitation is successfully eliminated and the power coefficient increases as well. Nevertheless, the thrust coefficient also increases which can also lead to structural problem for the turbine. There is clearly another balance between the extra costs of support structure (larger CT) and the benefits from the non-cavitation working condition and extra power (larger C_{pow}).

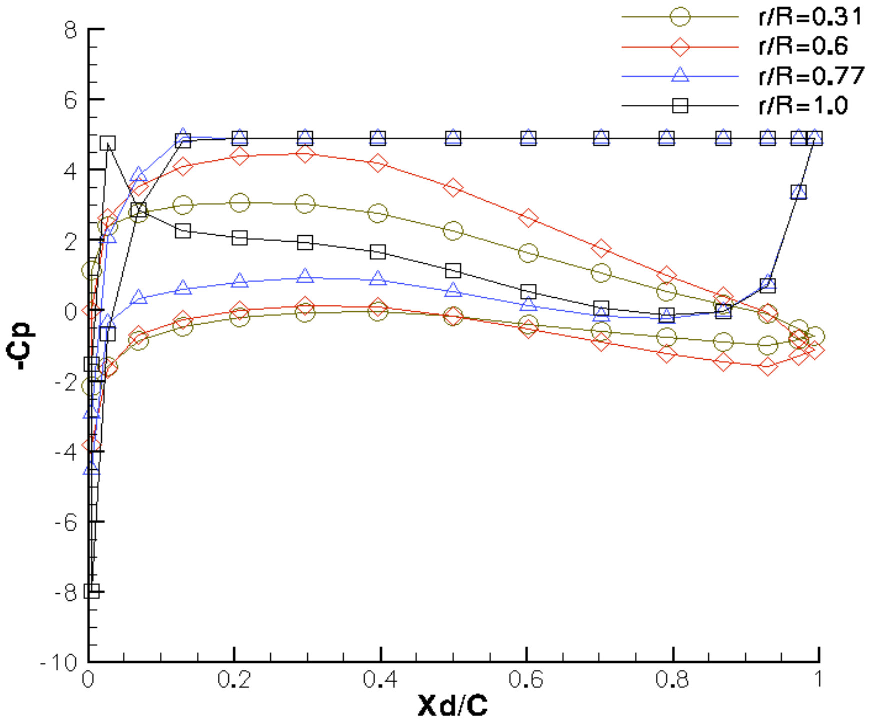

Fig. 4.41 Pressure distribution of the original cavitation case at different radii for Cavitating Case 1, σ_n=5.

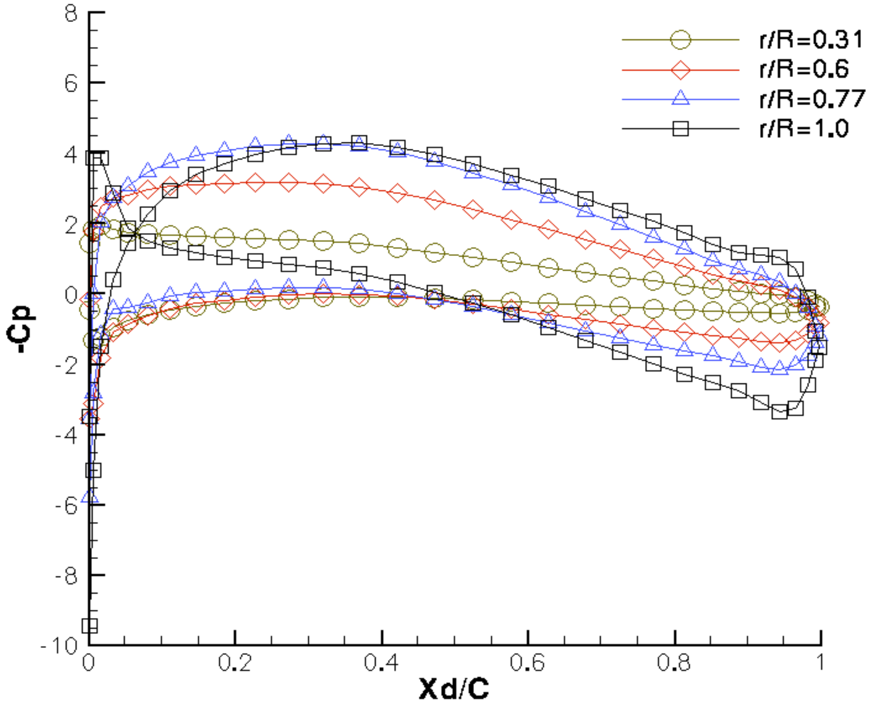

Fig. 4.42 Pressure distribution of the design turbine at different radii for Cavitating Case 1

Cavitating Case 2

A turbine with 40*m* diameter and 25^0 hub pitch, operating at *TSR*=7.5 is analyzed in this case. The tip immersion for this turbine is 5*m* and the tidal velocity is 3*m/s*. Thus the rotational frequency is n=0.179rev/s.

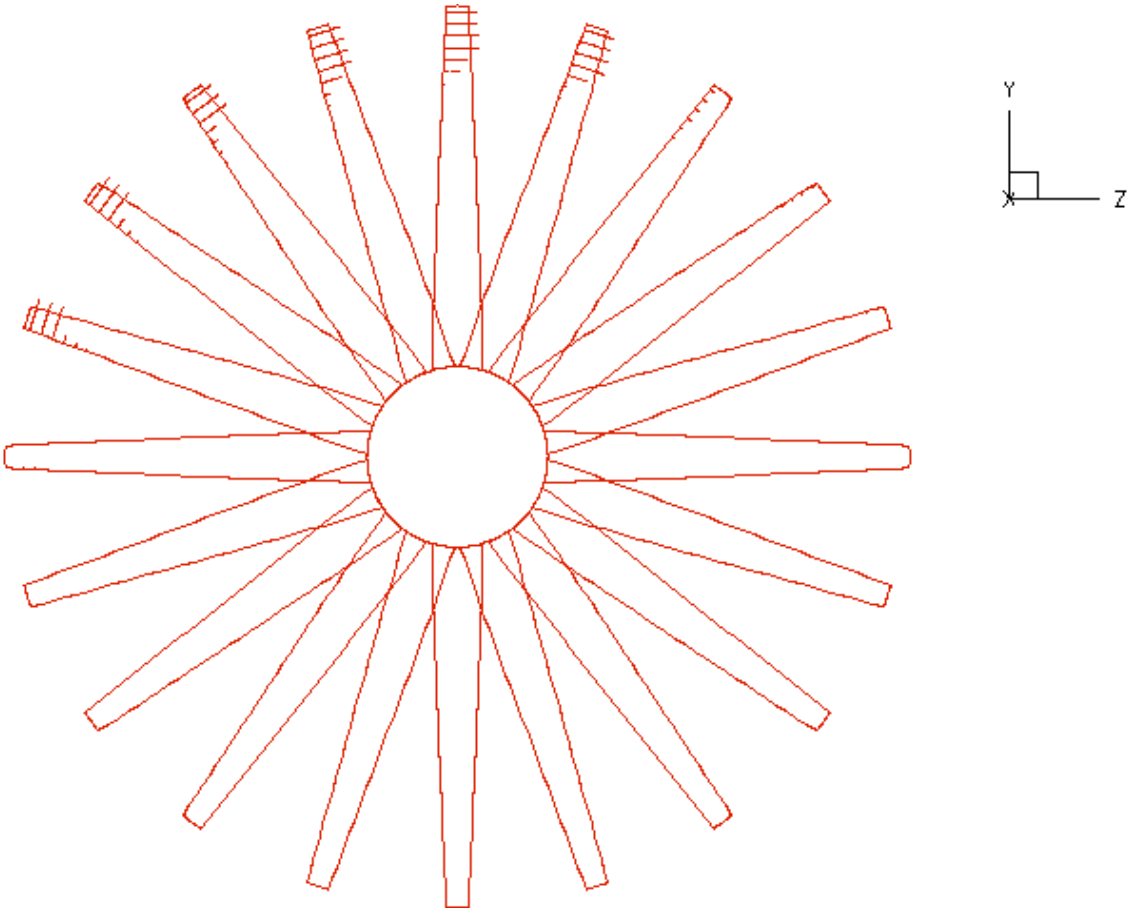

Fig. 4.43 Projected Blade geometry and cavity patterns at various angular positions for the original turbine (Cavitating Case 2)

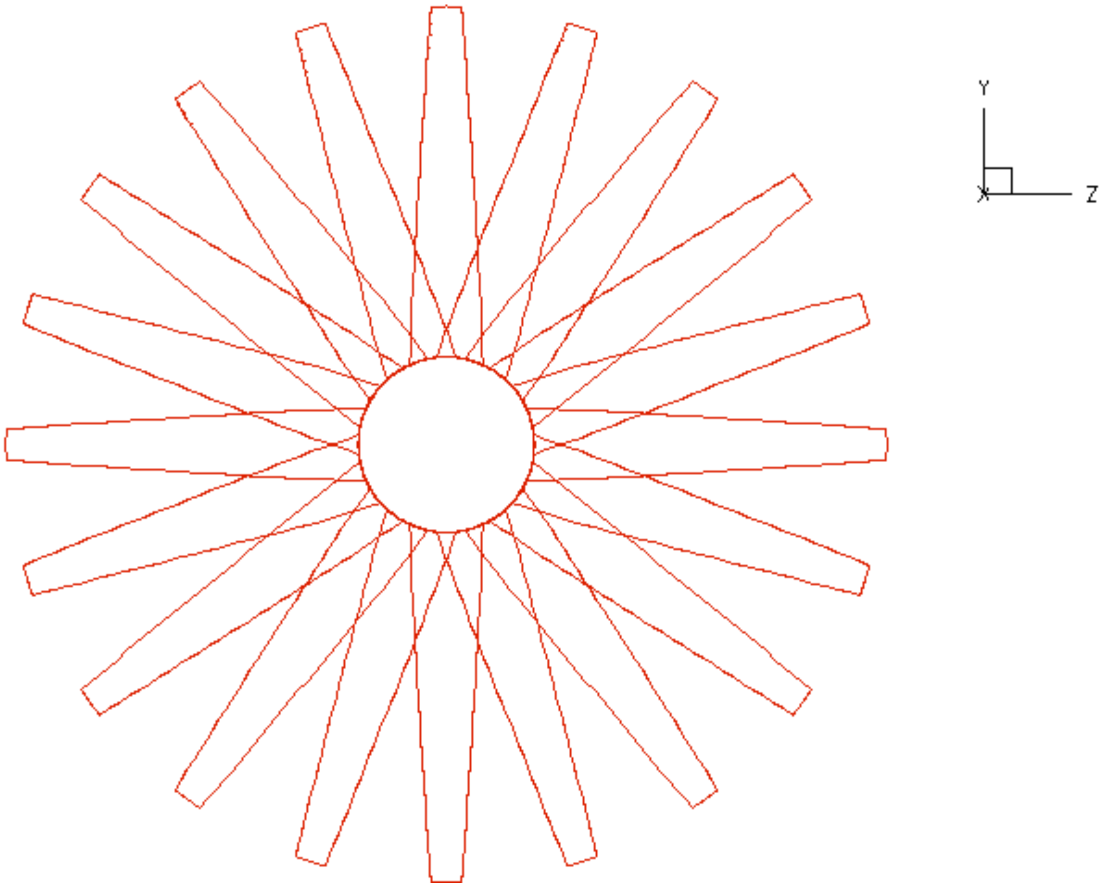

Fig. 4.44 Projected Blade geometry and cavity patterns at various angular positions for the design turbine (Cavitating Case 2)

The cavitation number is $\sigma_n=11.4$ and the Froude number is $Fr=n^2D/g=0.1308$. The cavity patterns at several angular positions are shown in Fig. 4.43. The thrust coefficient and power coefficient for the original turbine geometry are $CT=0.497$ and $C_{pow}=0.153$. A database is produced by selecting pitch and chord length as geometric parameters. The ranges of these two multipliers are changed to be $0.8\leq x_1\leq 1.2$ and $0.8\leq x_2\leq 1.5$, respectively. A fully wetted solution cannot be found in this database, which indicates the cavitation can only be reduced rather than be eliminated via searching this database. *CPMIN* is chosen to be 11.2 for this case, and the projected blade geometry and the cavity pattern of the optimal turbine when $x_1=0.8$ and $x_2=1.445$, are shown in Fig. 4.44. The thrust and power coefficients corresponding to the design geometry are

CT=0.697 and C_{pow}=0.342. Notice that the cavitation is greatly reduced by decreasing the pitch and increasing the chord length, while keeping the thickness of the blade the same. All design conditions and results are tabulated in Table 4.4.

Table 4.4 Three design cases by CAVOPT-BASE

	Fully wetted case	**Cavitating Case 1**	**Cavitating Case2**
Design Parameters	P/D c/D	P/D c/D	P/D c/D
Multipliers' Range	$0.8 \le x_1 \le 1.2$ $0.8 \le x_2 \le 1.2$	$1.0 \le x_1 \le 1.2$ $0.8 \le x_2 \le 1.5$	$0.8 \le x_1 \le 1.2$ $0.8 \le x_2 \le 1.5$
TSR	5.0	5.0	7.5
Design Multipliers	x_1=0.803 x_2=1.006	x_1=1.006 x_2=1.351	x_1=0.800 x_2=1.445
$CPMIN$	N/A	5.0	11.2
Original CT C_{pow}	0.550 0.390	0.486 0.317	0.497 0.153
Design CT C_{pow}	0.586 0.412	0.516 0.371	0.697 0.342

4.3.2 Nonlinear optimization method (CAVOPT-3D)

For this design method, only a fully wetted case is investigated in this research. An initial B-spline geometry is generated manually by specifying 4×4 control vertex. The initial 4×4 vertex polygon net and the initial turbine geometry are shown in Fig. 4.45 and Fig. 4.46.

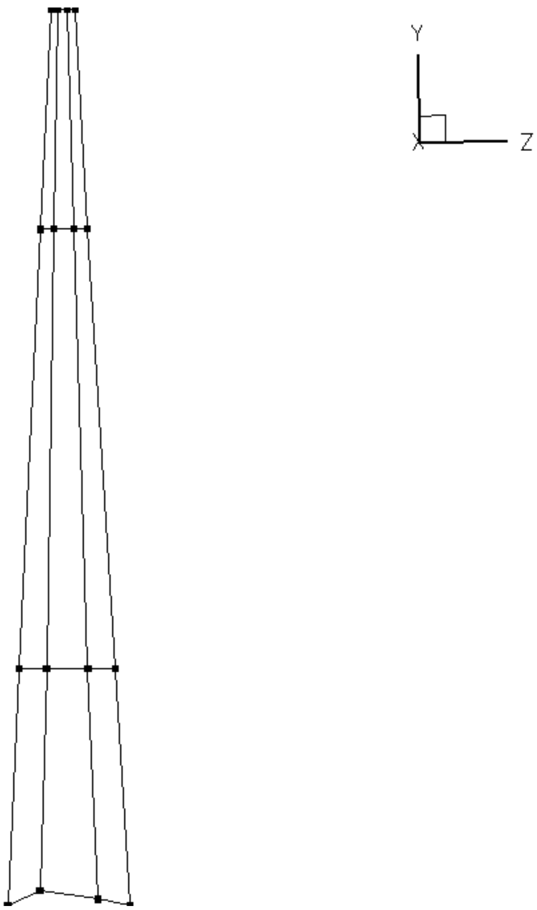

Fig. 4.45 4×4 vertex polygon net for the B-spline turbine geometry

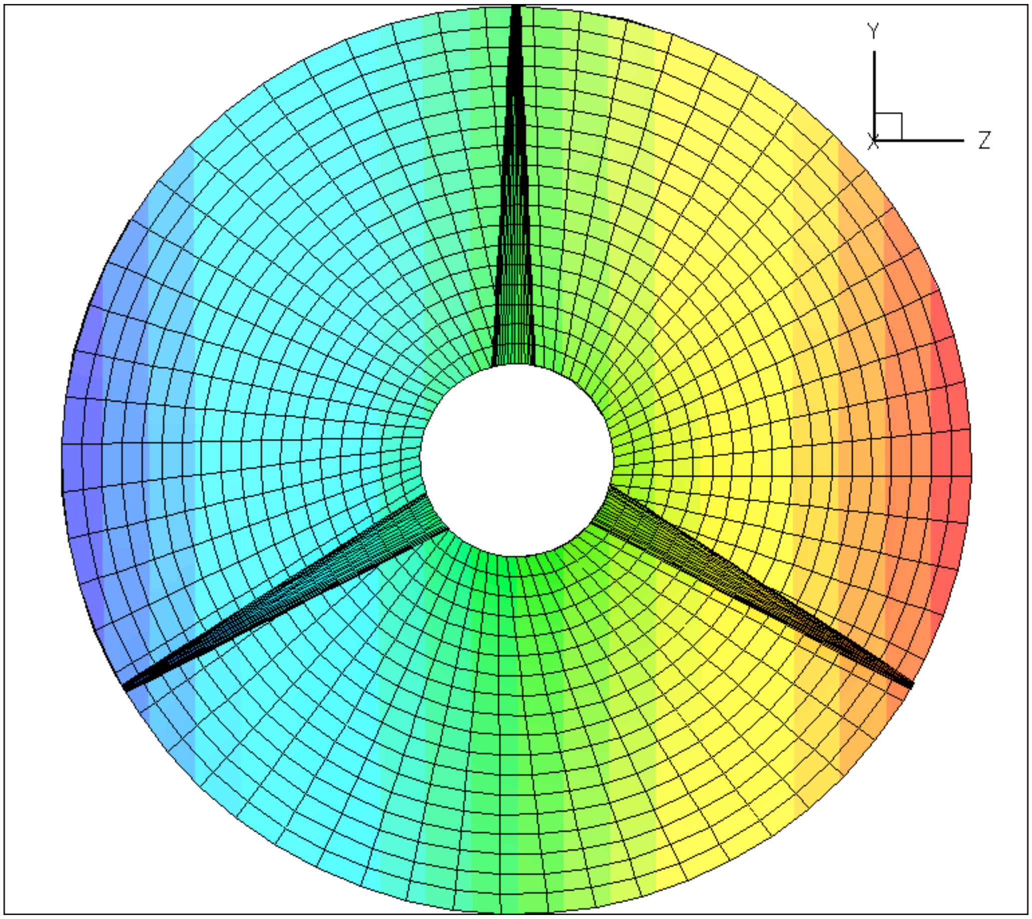

Fig. 4.46 Initial turbine geometry (utilized in CAVOPT-3D)

The support structure of the tidal turbine has a limit on the total thrust that is allowed for the operation of turbine. Therefore, an inequality constraint of the thrust coefficient is added instead of an equality constraint required in propeller cases. The design result of the fully wetted case by CAVOPT-BASE is adopted, i.e. $CT \leq 0.586$. For this case, constraints on the chord length distribution are applied in order to achieve reasonable design geometry. The chord length distribution of the experimental geometry as illustrated in Table 4.4 is adopted. The NACA 66 thickness form is used in generating the turbine blade sections. The final optimization problem is expressed as follows:

$$
\begin{array}{lll}
\multicolumn{3}{l}{\textit{problem}:} \\
\quad \max & C_{pow} & \\
\quad \text{subject to:} & & \\
 & CT \leq 0.586 & \\
 & \text{c/D=0.125} \quad \text{at} \quad \text{r/R=0.2} & \\
 & \text{c/D=0.106} \quad \text{at} \quad \text{r/R=0.4} & \\
 & \text{c/D=0.069} \quad \text{at} \quad \text{r/R=0.8} & \\
 & \text{c/D=0.050} \quad \text{at} \quad \text{r/R=1.0} &
\end{array}
\tag{4.3}
$$

The design turbine geometry is shown in Fig. 4.47, and the designed thrust and power coefficients are CT=0.586 and C_{pow}=0.411, respectively. The final pitch, chord and camber distributions corresponding to the design geometry are shown in Fig. 4.48.

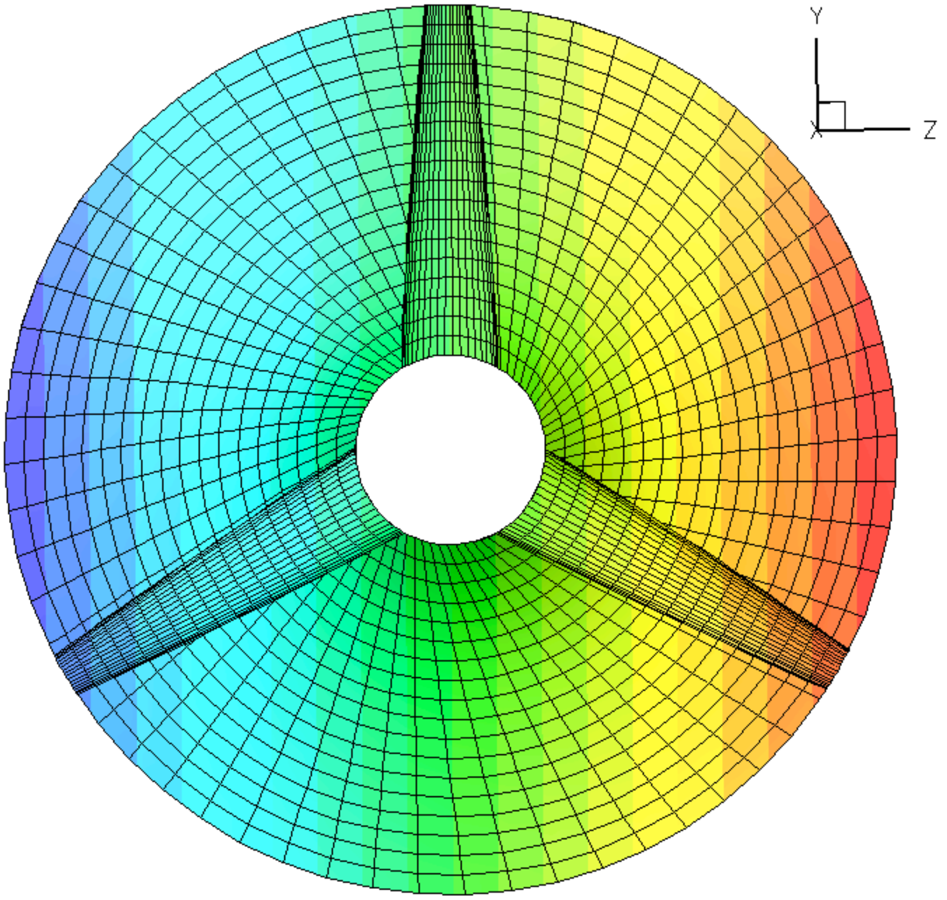

Fig. 4.47 Designed projected turbine geometry from CAVOPT-3D

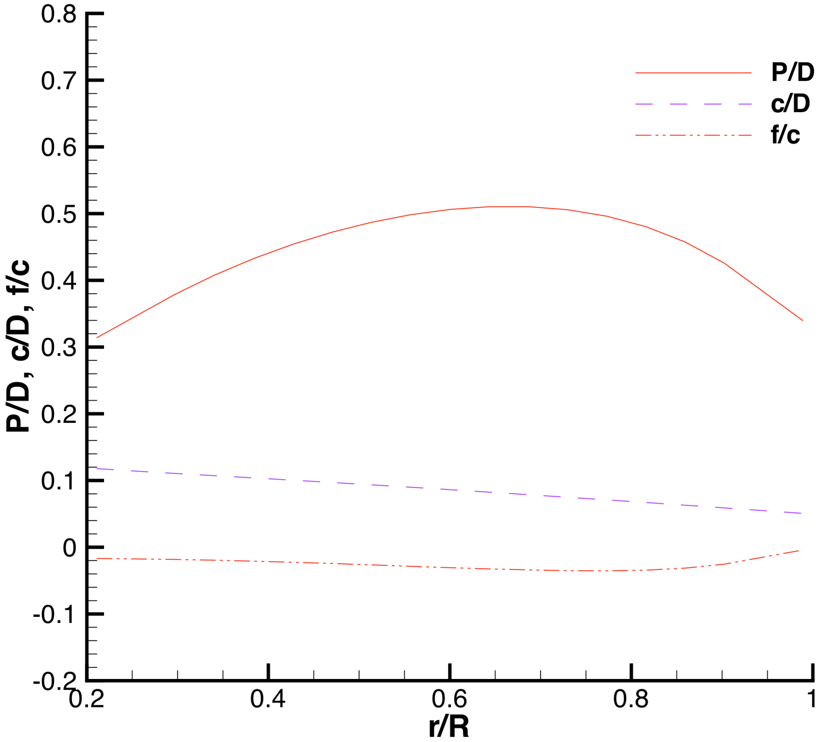

Fig. 4.48 Designed pitch (*P/D*), chord (*c/D*) and camber (*f/c*) distributions for the designed turbine

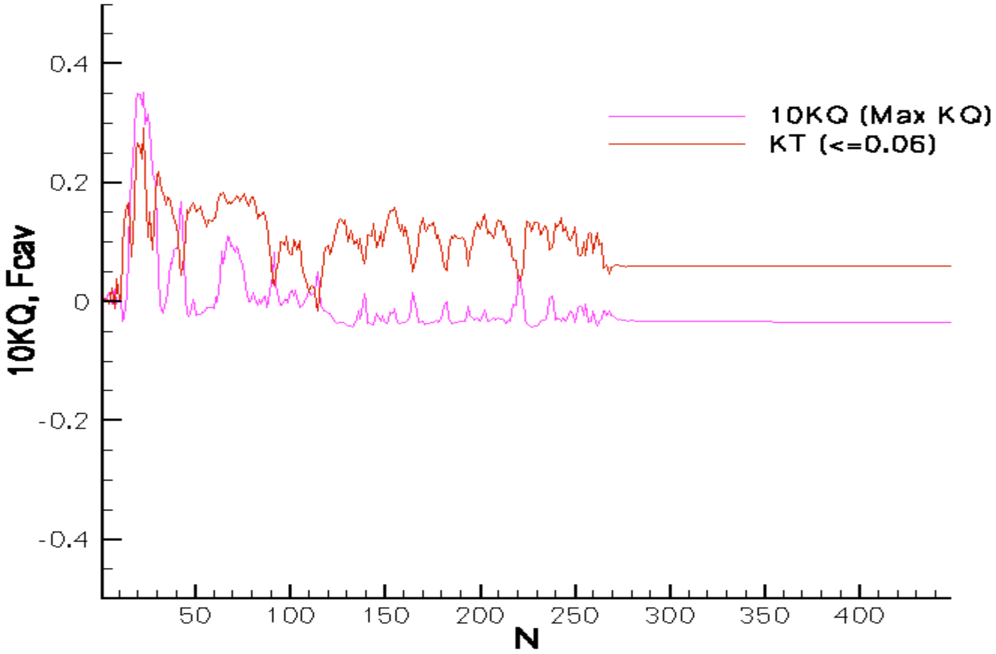

Fig. 4.49 Convergence history for the design of turbine

The optimized result from CAVOPT-3D is on the boundary of the thrust coefficient inequality constraint ($CT \leq 0.586$), which indicates that more output power may be produced when given more allowed thrust. On the other hand, by having the same design thrust coefficient, the design power coefficient in this case (C_{pow}=0.411) is also very close to that from the fully wetted case of CAVOPT-BASE (C_{pow}=0.414), although the final turbine geometries are different for these two cases. Fig. 4.49 is the convergence history of the optimization problem, which shows that the method can converge well in terms of the final K_T and K_Q. The relationship between K_T, K_Q and CT, C_{pow} has already been addressed in the previous section.

4.3.3 The complete design procedure

The objective of this section focuses on developing a procedure for designing an optimal blade geometry, which gives the turbine the maximum efficiency or maximum output power. The procedure starts by applying a lifting line theory based optimization method (LLOPT) to generate the shape of the circulation distribution for a turbine with a given number of blades and an operating condition. A circulation database searching method (LLOPT-BASE) is then utilized to produce the optimal circulation distribution that gives turbine the maximum efficiency within the database. Based on the circulation distribution, a base turbine geometry is generated by specifying a chord, a maximum thickness distribution and a blade section profile. The base geometry is, therefore, used to generate a performance database by running a VLM-based potential flow solver (MPUF-3A) with different blade geometries. Finally, a nonlinear optimization method CAVOPT-BASE is utilized to refine the turbine geometry. The design procedure is illustrated in Fig. 4.50. It should be noted that VLM has the advantage of being more accurate than lifting line theory on the prediction of the turbine performance, and the effect of free surface and non-uniform inflow can also be included by using a hybrid viscous/potential flow method, which couples MPUF-3A with a viscous flow solver.

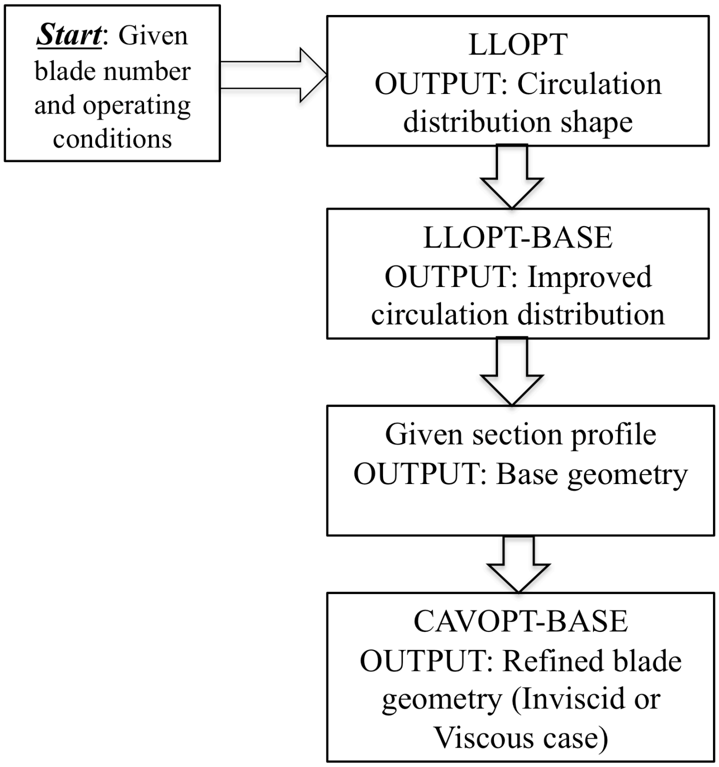

Fig. 4.50 Flow chart of design procedure

4.3.3.1 Determining the optimum circulation distribution

The LLOPT-BASE will be used to generate the optimum circulation distribution. In this research, a 3-blade horizontal tidal turbine will be designed, and the optimum circulation indicated in Fig. 4.2 will be used in this design procedure.

4.3.3.2 Generation of base geometry

Based on the optimum circulation distribution from LLOPT-BASE for a 3-blade turbine operating at *TSR*=6, a base turbine geometry is produced by specifying a section profile, a chord distribution and a maximum thickness distribution. Based on (Abbott & Von Doenhoff, 1959), the geometry of the NACA mean line a=0.8 and the NACA66 basic thickness form are chosen for the blade section profile, where α_0=1.54° and f_0=0.0679$c(i)$ (see Appendix C). The same chord and maximum thickness distributions in (Bahaj, Molland, et al., 2007) are used to generate the base blade geometry for CAVOPT-BASE. The hub effect and viscous effect are not included in LLOPT, LLOPT-BASE and MPUF-3A at this stage. These effects will be included later (Section 4.3.3.3). As plotted in Fig. 4.51, the circulation distribution from MPUF-3A is close to the optimum result of LLOPT-BASE. The C_{pow} given by MPUF-3A is equal to 0.476, which is close to the result from LLOPT-BASE (C_{pow}=0.485). It should be noted that the power coefficient has the same definition as efficiency (shown in Section 3.1). Fig. 4.52 shows that the design *TSR* predicted by MPUF-3A for the base geometry is 6.0, which is consistent with the design condition at the beginning of the procedure. In addition, MPUF-3A is more precise in wake modeling, and the corresponding prediction on the turbine performance is, therefore, more accurate.

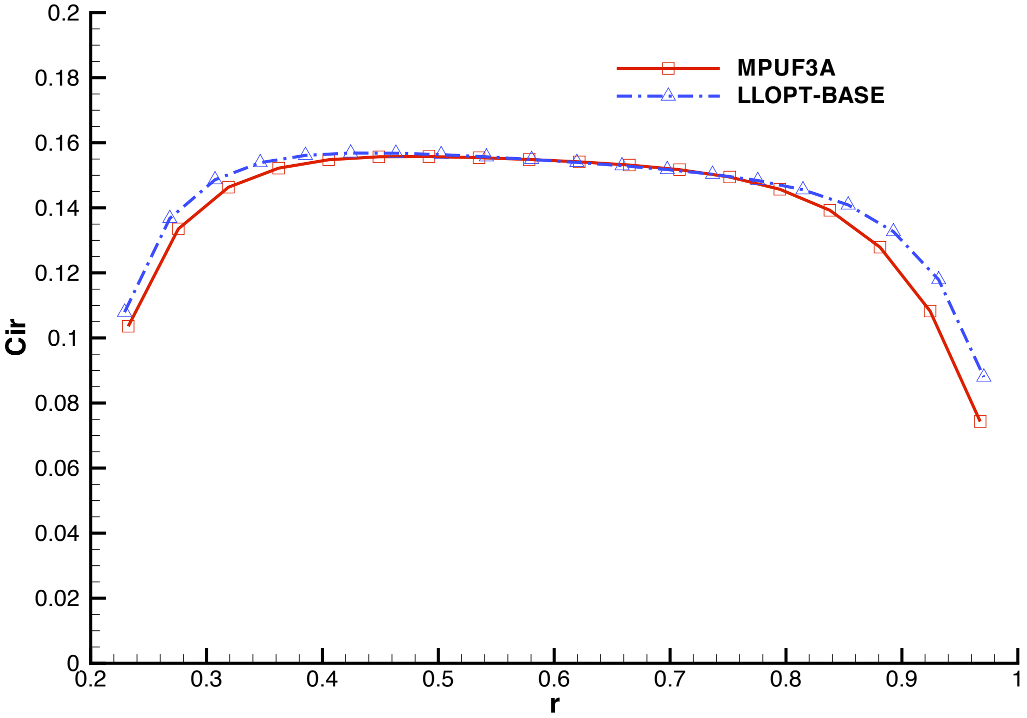

Fig. 4.51 Comparison of the circulation distribution form MPUF-3A and LLOPT-BASE

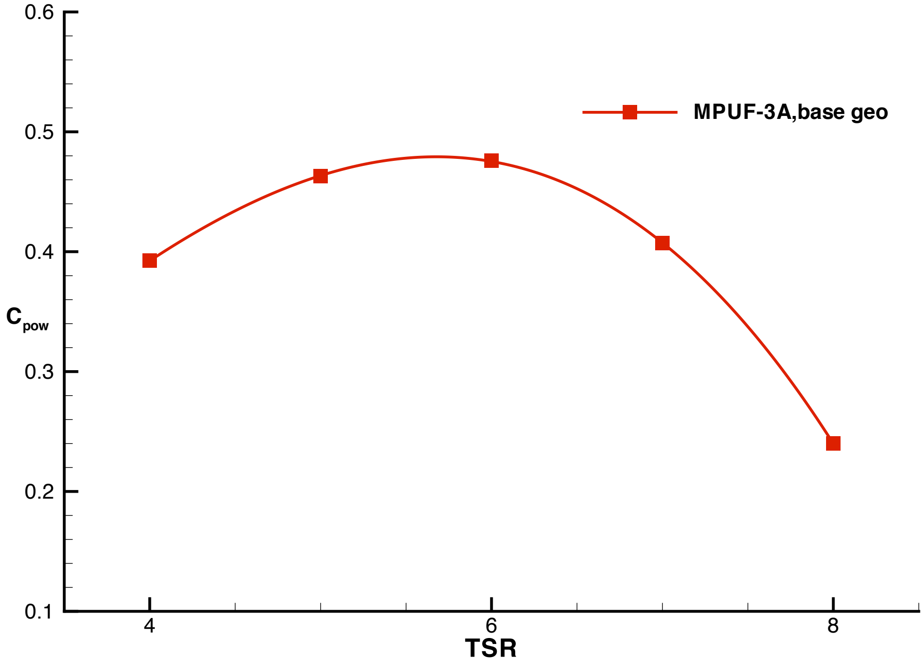

Fig. 4.52 Power coefficient (inviscid) for the base turbine over a range of *TSR*.

4.3.3.3 Geometry refinement by CAVOPT-BASE

CAVOPT-BASE method, which couples MPUF-3A with a nonlinear optimization method, is adopted to improve the turbine blade design. The base geometry is generated from the resulting circulation distribution given by LLOPT-BASE. The normalized pitch (P/D), chord length(c/D) and camber (f/D) are selected as the three geometric parameters to produce a performance database. The three multipliers (x_1, x_2 and x_3), which correspond to normalized pitch, chord length and camber, are range from 0.9 to 1.1, and the constraint for *CPMIN* is inactivated in this fully wetted design case. The design result gives C_{pow}=0.520 when x_1=0.91, x_2=1.08 and x_3=1.07. The chord and camber increase, while the pitch decreases. The viscous effect, which is not considered in this design procedure, can be included in MPUF-3A by applying a friction coefficient over the blade. According to (Comstock, 1967), the friction coefficient C_f is calculated based on the Reynolds number Re:

$$C_f = \frac{0.075}{(\log_{10} \mathrm{Re} - 2)^2} \tag{4.4}$$

Re is determined based on the chord of the section at r=0.7R, which gives C_f=0.0068. A viscous performance database for turbines operating at *TSR*=6.0 is then generated. The same ranges of the three multipliers are adopted for the viscous database. The design result from CAVOPT-BASE gives C_{pow}=0.434 when x_1=0.9, x_2=1.02 and x_3=1.07. The viscous design C_{pow} is reduced by 16.5% when compared to that of the inviscid design. The results indicate that the extra power and the extra viscous loss due to larger chord length are balanced, and the chord length from the viscous design is less than that of the inviscid design, as plotted in Fig. 4.53. Note that a fully viscous design can be carried out via incorporating the viscous effects in LLOPT and LLOPT-BASE.

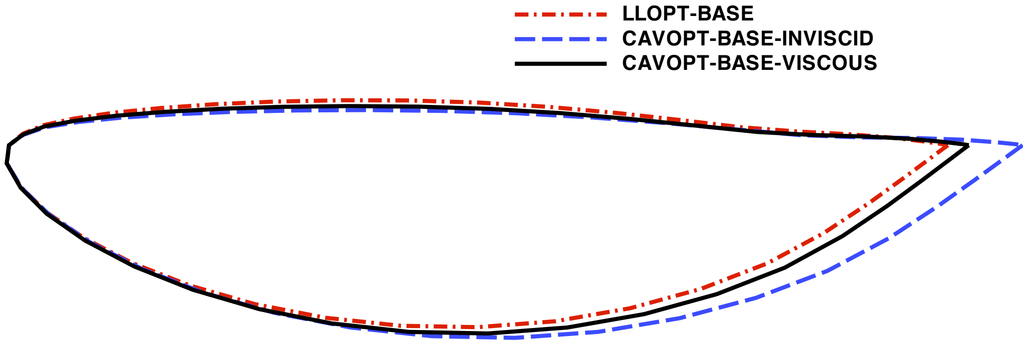

Fig. 4.53 Comparison of the section profiles at *r*=0.2*R*

Chapter 5

Results of Design Methods for Propellers

The optimum circulation distribution of propeller is generated via LLOPT, in which the torque coefficient is minimized for a specified thrust coefficient. The database searching method CAVOPT-BASE is utilized for the design of propeller with a N4148 base geometry. The nonlinear optimization method CAVOPT-3D, which start with a random assumed blade geometry, is also applied in automatically producing the optimum propeller geometry by minimizing torque coefficient as well as reducing or eliminating cavitations for a given thrust coefficient.

5.1 OPTIMUM CIRCULATION DISTRIBUTION

In this section, LLOPT is applied on propellers and the results are compared directly with those of (J. E. Kerwin, 2001). A five bladed propeller with r_h/R equal to 0.2 is investigated. The viscous effect is ignored and the thrust coefficient (C_T=$2T/\rho V^2 A_0$) is given at 0.512. By following a similar procedure of LLOPT for turbines, the optimum circulation can be produced in an iterative way. More details of the LLOPT method for propellers and the updating scheme can be found in (J. E. Kerwin, 2001). Fig. 5.1 shows several typical optimum circulation distributions of a propeller for different advance ratios (*J)* and those compare very well with those shown in (J. E. Kerwin, 2001). As is indicated in Fig. 5.1, the circulation distribution will become uniform except for the tip and root parts when *J* is small enough, i.e., J=0.1. Notice that an almost uniform circulation distribution can also produce a maximum efficiency for turbines when *J* is small enough (Xu, 2009).

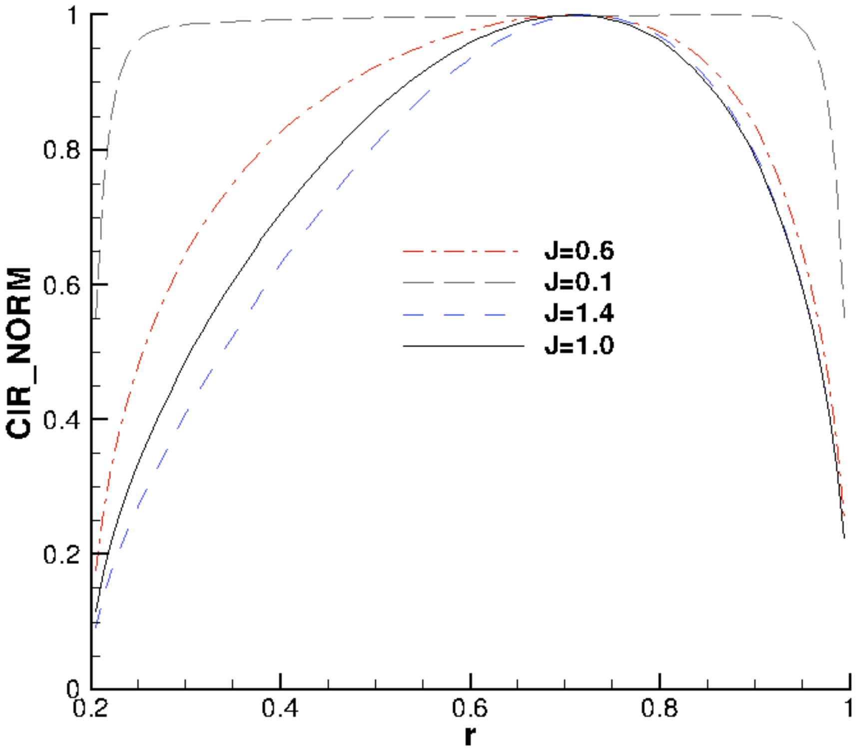

Fig. 5.1 Distribution of circulation with different advance ratio J when C_T=0.512, should be compared directly with Fig. 45 of (J. E. Kerwin, 2001). Note: IR_NORM is the normalized circulation, which has same definition as $\bar{\Gamma}$)

The propeller efficiency η is defined as $\eta = TV/\omega Q$, where T is the thrust and Q is the torque. The procedure of generating the efficiency when J and C_T are given can be found in (J. E. Kerwin, 2001). The effect of different discretization numbers (*m*) of blades on the propeller performance is investigated and the variation of efficiency for different *m* are shown in Table 5.1 and Fig. 5.2. As pointed out in (J. E. Kerwin, 2001), the propeller efficiency to the limit of J=0 is $\eta = 2\big/(1+\sqrt{1+C_T}) = 0.897$, which is the same as that by using actuator disk theory.

Table 5.1 Efficiencies with different discretization number (*m*) at different *J*

J	0	0.1	0.6	1	1.4
η (m=10)	0.9	0.890086	0.863967	0.824556	0.763928
η (m=100)	0.9	0.892115	0.864447	0.825141	0.76456

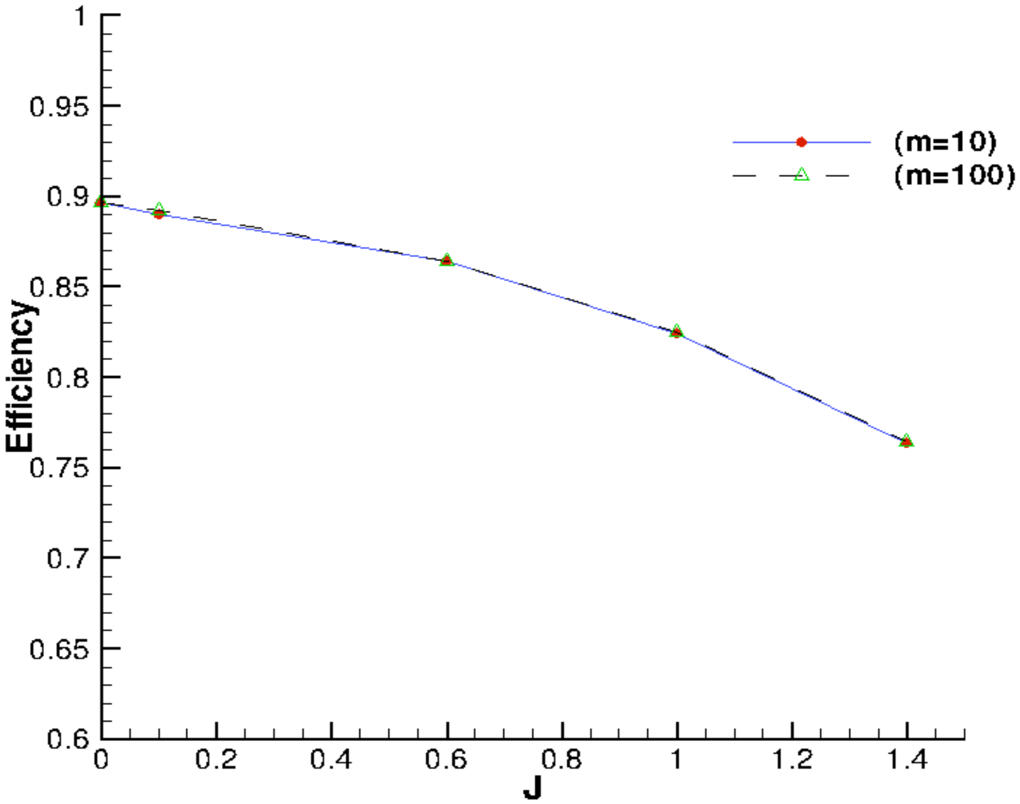

Fig. 5.2 Variation of propeller efficiency with advance ratio *J* (m=10 & m=100), should be compared with Fig. 46 of (J. E. Kerwin, 2001)

As shown in Fig. 5.2, the propeller efficiency approaches the actuator disk theory result when the advance ratio *J* approaches zero. The difference between cases with different discretization number *m* is small, which indicates that small number of *m* is adequate to accurately predict the propeller efficiency via using LLOPT. Additionally, in the case of propellers, LLOPT is sufficient in determining the optimum circulation distribution without resorting to LLOPT-BASE, which has to be applied in the case of turbines.

5.2 APPLICATION OF CAVOPT-BASE TO PROPELLERS

The CAVOPT-BASE developed in (Deng, 2005; Kinnas, et al., 2005) coupled MPUF-3A with a nonlinear optimization method. In this research, CAVOPT-BASE is coupled with the boundary element method (PROPCAV). A fully wetted case and a cavitating case are investigated using the modified CAVOPT-BASE and the N4148 propeller as the base geometry.

In designing a propeller, the pitch, chord and camber are chosen to be the parameters that are utilized to produce a 10×10×10 performance database.

$$\begin{aligned}
(P/D)_{design} &= (P/D)_{base} \times x_1 \\
(c/D)_{design} &= (c/D)_{base} \times x_2 \\
(f/c)_{design} &= (f/c)_{base} \times x_3
\end{aligned} \tag{5.1}$$

where x_1, x_2 and x_3 are three coefficients for adjusting the corresponding three parameters.

5.2.1 Fully wetted case

In this fully wetted case, a propeller with K_T=0.15 and the advance ratio of J=1.0 is designed. The runs are performed as fully wetted. A *CPMIN* constraint (*CPMIN*≤3) is applied here in order to avoid cavitation when σ_n=3.0. The optimization problem can be expressed as follows, and the ranges of x_1, x_2 and x_3 are specified:

$$\begin{aligned}
&\text{minimize} && K_Q(x) \\
&\text{subject to} && K_T = 0.15 \\
& && C_{P\min}(x) \leq CPMIN(= 3.0) \\
& && 0.8 \leq x_1 \leq 1.5 \\
& && 0.8 \leq x_2 \leq 2.0 \\
& && 0.0 \leq x_3 \leq 3.0
\end{aligned} \tag{5.2}$$

The initial geometry of N4148 propeller is shown in Fig. 5.3. Fig. 5.4 shows the pressure distribution at different radii corresponding to the base geometry when subject to uniform inflow. Note that cavitation will occur at the leading edge if σ_n=3.0. The thrust coefficient (K_T) and torque coefficient (K_Q) for the original geometry are 0.023 and 0.00519, respectively, and the efficiency η=0.705. Each range of x_1, x_2 and x_3 is divided into 9 intervals, and a 10×10×10 performance database[4] is generated, in which the designed propeller geometry can be searched via minimizing the torque and by satisfying all constraints. The projected design geometry of propeller is shown in Fig. 5.5. Fig. 5.6 shows the corresponding pressure distribution at different radii, in which the *CPMIN* constraint is satisfied (max(C_{Pmin}=3.0) in this design case. The thrust and torque coefficients of the design geometry are K_T=0.15 and K_Q=0.02967, respectively, when x_1=1.182, x_2=0.829 and x_3=2.667. And the design efficiency is η=0.805. In this database, the optimal geometry, which satisfies the constraints, is the one with a smaller chord length, higher pitch and larger camber.

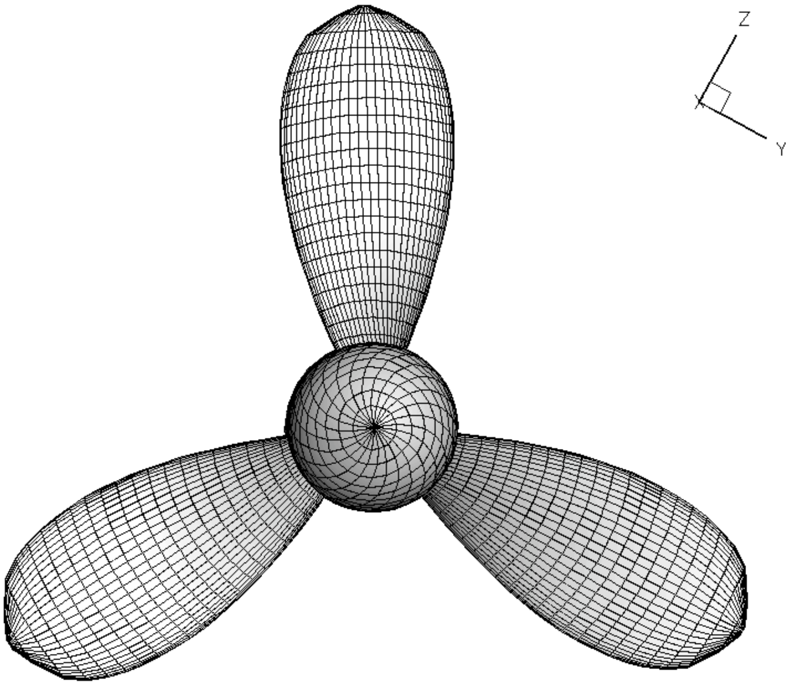

Fig. 5.3 Initial geometry for the propeller design in CAVOPT-BASE

---

[4] It only takes 10 minutes to generate the database when distributing the job to 10 CPUs and using 40×18 grid in PROPCAV. One CPU is Intel(R) Xeon(R) CPU with 2.4 GHz.

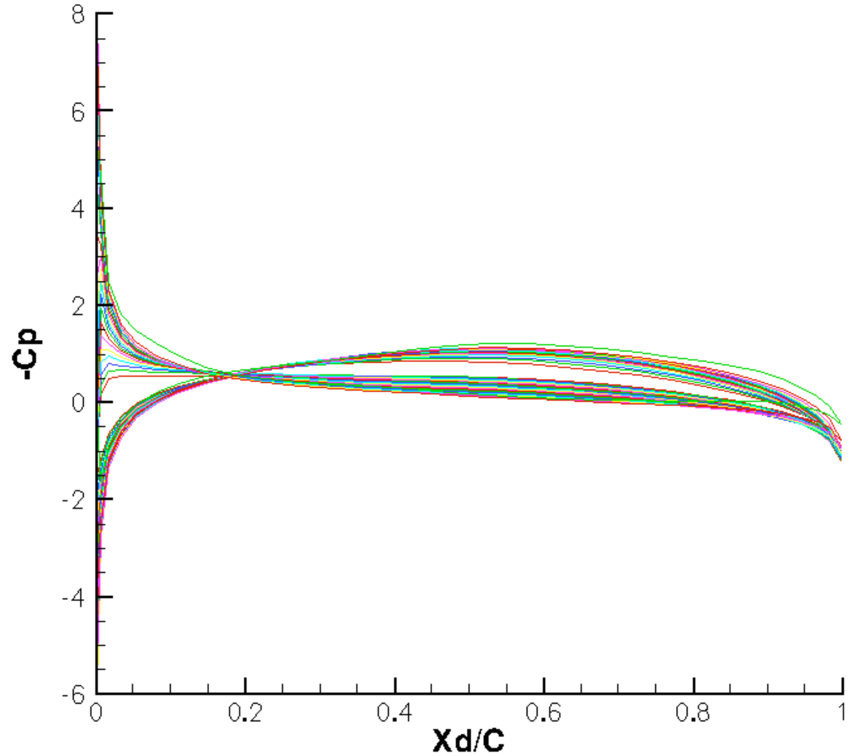

Fig. 5.4 Pressure distributions at different radii for the base geometry of turbine subject to uniform inflow

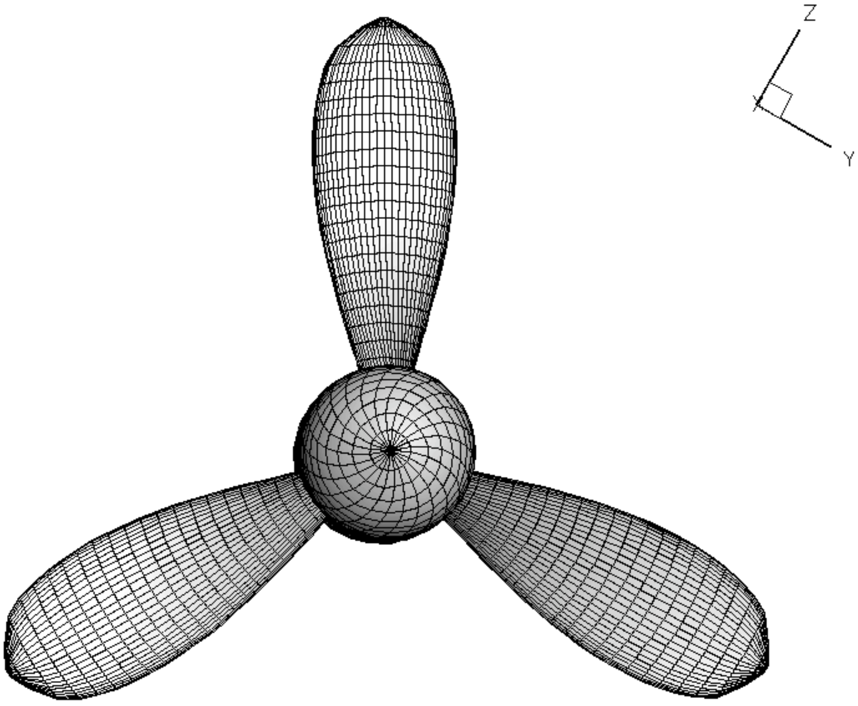

Fig. 5.5 Design geometry of propeller for the fully wetted case

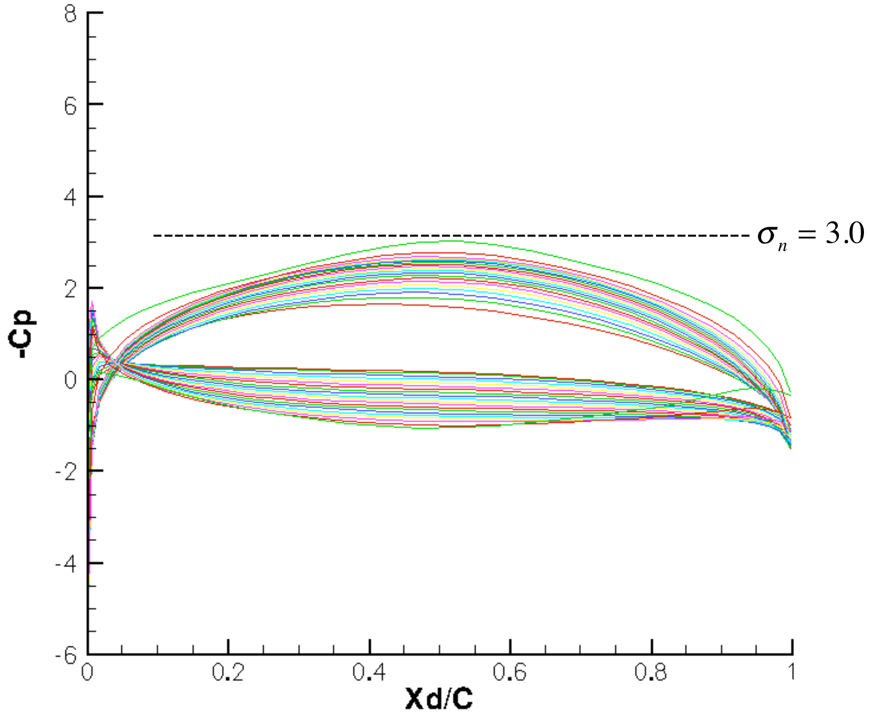

Fig. 5.6 Pressure distribution at different radii for the propeller geometry designed by CAVOPT-BASE, subject to uniform inflow.

5.2.1 Fully wetted at lower cavitation number

In a cavitating case with J_s=1.0 and K_T=0.15, the design geometry from the previous fully wetted case is adopted as the initial geometry. The cavitation number σ_n is chosen to be 2.5, which produces K_T=0.1519, K_Q=0.02984 and η=0.81. In order to design a propeller without any cavitation, a modified constraint of C_{Pmin} needs to be included. The optimization problem can, therefore, be expressed as follows:

$$\begin{aligned} &\text{minimize } K_Q(x) \\ &\text{subject to } \quad K_T = 0.15 \\ &\qquad\qquad C_{P\min}(x) \le CPMIN(= 2.5) \\ &\qquad\qquad 0.8 \le x_1 \le 1.5 \\ &\qquad\qquad 0.8 \le x_2 \le 2.0 \\ &\qquad\qquad 0.0 \le x_3 \le 3.0 \end{aligned} \tag{5.3}$$

Notice that the value of *CPMIN* has been changed to 2.5, which can eliminate the cavitation in the designed case if the *CPMIN* constraint is satisfied. Fig. 5.7 shows the pressure distribution at different radii corresponding to the initial geometry when σ_n=2.5. The negative pressure coefficient (-*Cp*) cannot go beyond 2.5 since the occurrence of cavitation. The cavity pattern for the initial geometry is shown in Fig. 5.8. A performance database with same ranges of x_1, x_2 and x_3, and same size (10×10×10), is generated in CAVOPT-BASE. Fig. 5.9 shows the pressure distribution at different radii for the final design propeller with maximum C_{pmin} equal to 2.5. The design results are K_T=0.15 and K_Q=0.0302 with η=0.791 when x_1=1.012, x_2=1.235 and x_3=0.847. The cavitation has been successfully eliminated via adjusting the propeller geometry. The propeller design conditions and results from CAVOPT-BASE are tabulated in Table 4.4. Please note that the fully wetted propeller geometry at lower cavitation number, has lower efficiency and larger chord, as expected.

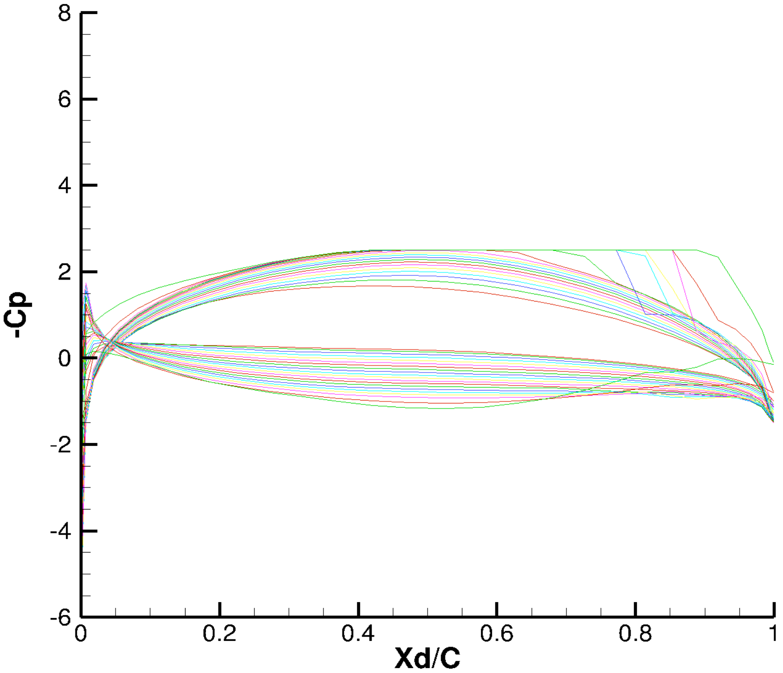

Fig. 5.7 Pressure distribution at different radii for the initial geometry of propeller in the fully wetted case at low cavitation number (σ_n=2.5).

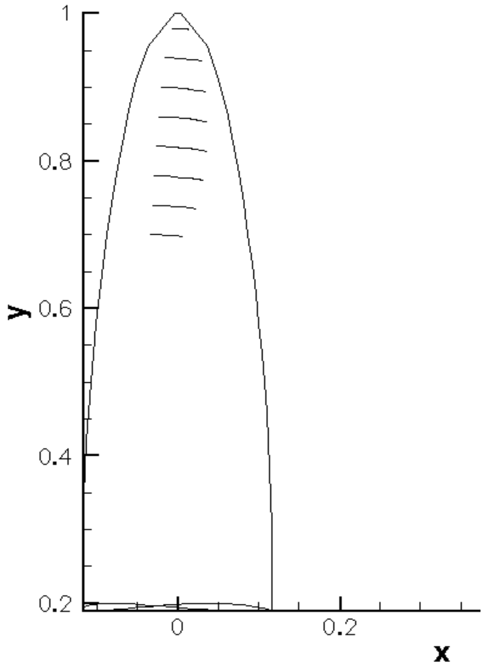

Fig. 5.8 Initial blade geometry of propeller and the corresponding cavity patterns for the fully wetted case at low cavitation number (σ_n=2.5).

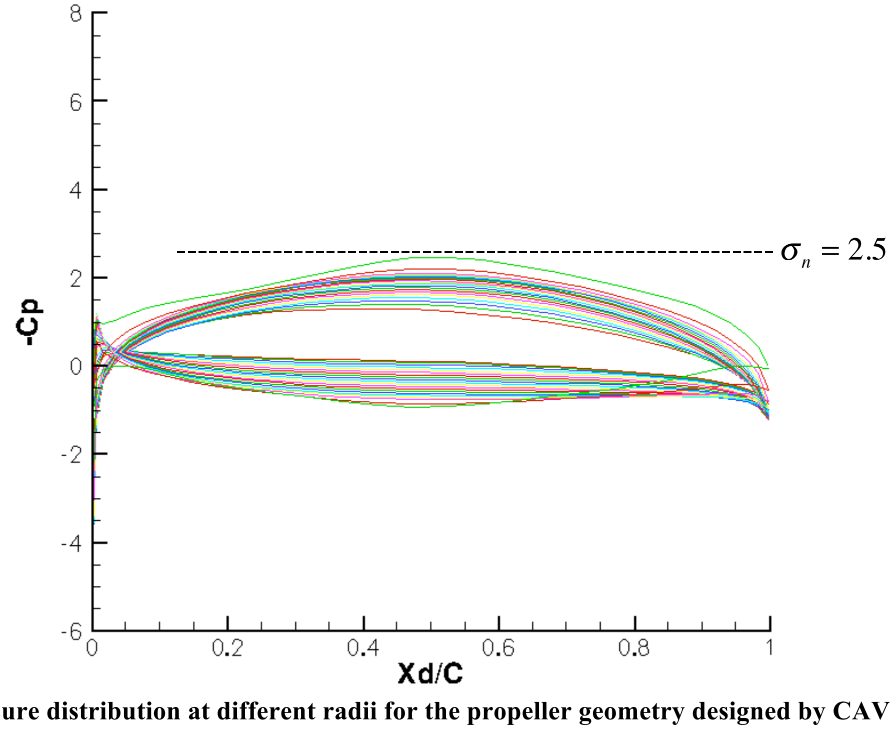

Fig. 5.9 Pressure distribution at different radii for the propeller geometry designed by CAVOPT-BASE.

Table 5.2 Two design cases by CAVOPT-BASE (for propellers)

	Fully wetted case	**Fully wetted-lower σ_n**
Design Parameters	P/D c/D f/c	P/D c/D f/c
Multipliers' Range	$0.8 \le x_1 \le 1.5$ $0.8 \le x_2 \le 2.0$ $0.0 \le x_3 \le 3.0$	$0.8 \le x_1 \le 1.5$ $0.8 \le x_2 \le 2.0$ $0.0 \le x_3 \le 3.0$
J	1.0	1.0
Design Multipliers	$x_1=1.182$ $x_2=0.829$ $x_3=2.667$	$x_1=1.012$ $x_2=1.235$ $x_3=0.847$
CPMIN	3.0	2.5
Original K_T K_Q η	0.023* 0.00519 0.705	0.1519** 0.02984 0.810
Design K_T K_Q η	0.15 0.0297 0.804	0.15 0.0302 0.791

5.3 APPLICATION OF CAVOPT-3D TO PROPELLERS

CAVOPT-3D originally developed in (Mishima & Kinnas, 1996) coupled an older version of MPUF-3A with a nonlinear optimization method. During the past 13 years, MPUF-3A has been improved and a new version (v3.0) has been released in 2010 (L. He, S. H. Chang, & S. A. Kinnas, 2010). In this research, CAVOPT-3D is modified to couple the most recent version of MPUF-3A with the nonlinear optimization method. Design cases for both non-skewed and skewed propellers are investigated by the new CAVOPT-3D in this section. In the design procedure, a coarse grid (20×9) is adopted and the wake alignment and the thickness-loading coupling are applied in the MPUF-3A.

---

* K_T is wrong due to arbitrary initial geometry.

** K_T is somewhat larger than 0.15 due to the presence of partial cavitation.

5.3.1 Non-skewed propeller design

In the early years, cavitation was undesirable in the design of propellers due to the issues that were stated in Section 1.4. Nowadays, moderate cavitation is allowed in the design of propellers in order to get better efficiency. The objective of the design method CAVOPT-3D is to minimize the torque coefficient K_Q, as well as to reduce or eliminate the cavitation when given a certain thrust coefficient. In this section, a 3-blade non-skewed cavitating propeller cases with cavitation number σ_n=2.5 and Froude number Fr=5.0 are investigated, and the modified NACA66 thickness form is adopted. In order to limit the cavitation under a certain amount, a new inequality constraint (CA $\leq$ 0.3) is applied in the optimization, where CA is the maximum value of ratio of the cavity area with respect to the total blade area.

Thus, the optimization problem can be expressed as follows:

$$\begin{aligned} &\textit{problem}: \\ &\quad \text{minimize} \quad \mathrm{K}_Q \\ &\quad \text{subject to:} \quad \mathrm{K}_T = 0.2 \\ &\quad \qquad\qquad\quad\ \mathrm{CA} \leq 0.3 \end{aligned} \tag{5.3}$$

The projected design blade geometry and the cavity pattern (shown for 4 blade locations) of the propeller subject to uniform inflow are shown in Fig. 5.10. Fig. 5.11 illustrates the corresponding pitch, chord and maximum camber distributions[*] for the design propeller. The final design results are K_T=0.2 and K_Q=0.050, which produces η=0.764. The hydrostatic effect on the cavitation can be seen by comparing the top and bottom cavity patterns in Fig. 5.10. Another design case is carried out in order to design a cavitating 3-blade propeller when subject to non-uniform inflow. The velocity contour of

---

[*] The entire camber distribution is determined in CAVOPT-3D. However, only the maximum camber is presented in the results of this work.

the non-uniform inflow is shown in Fig. 5.13. Fig. 5.14 shows the projected design propeller geometry and cavity patter for 4 time steps. The corresponding pitch, chord and maximum camber distributions for the design propeller are shown in Fig 5.15. As can be seen from Fig. 5.11 and Fig. 5.15, the propeller chord length when subject to non-uniform inflow increases appreciably when compared to the design results from the uniform inflow case. The thrust and torque coefficients for this case are K_T=0.2, and K_Q=0.0442, respectively, and the efficiency is η=0.864. It should be noted that the efficiency is increased since the volumetric mean of the inflow wake is 14% smaller than the ship speed. The convergence history for these two cavitating cases are shown in Fig. 5.12 (uniform) and Fig. 5.16 (non-uniform), both of which have strong oscillations in reaching the final design geometry.

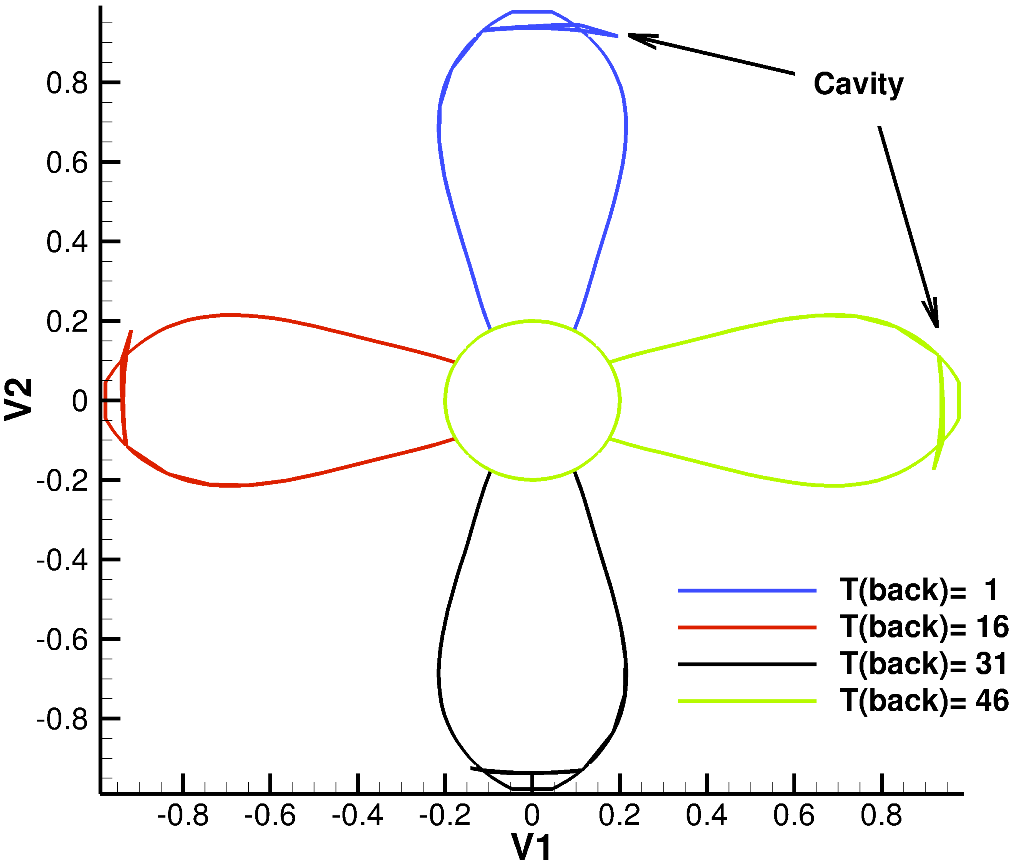

Fig. 5.10 Designed projected blade geometry and cavity pattern at different time steps for the cavitating case (uniform inflow, 0 skew, CA≤0.3)

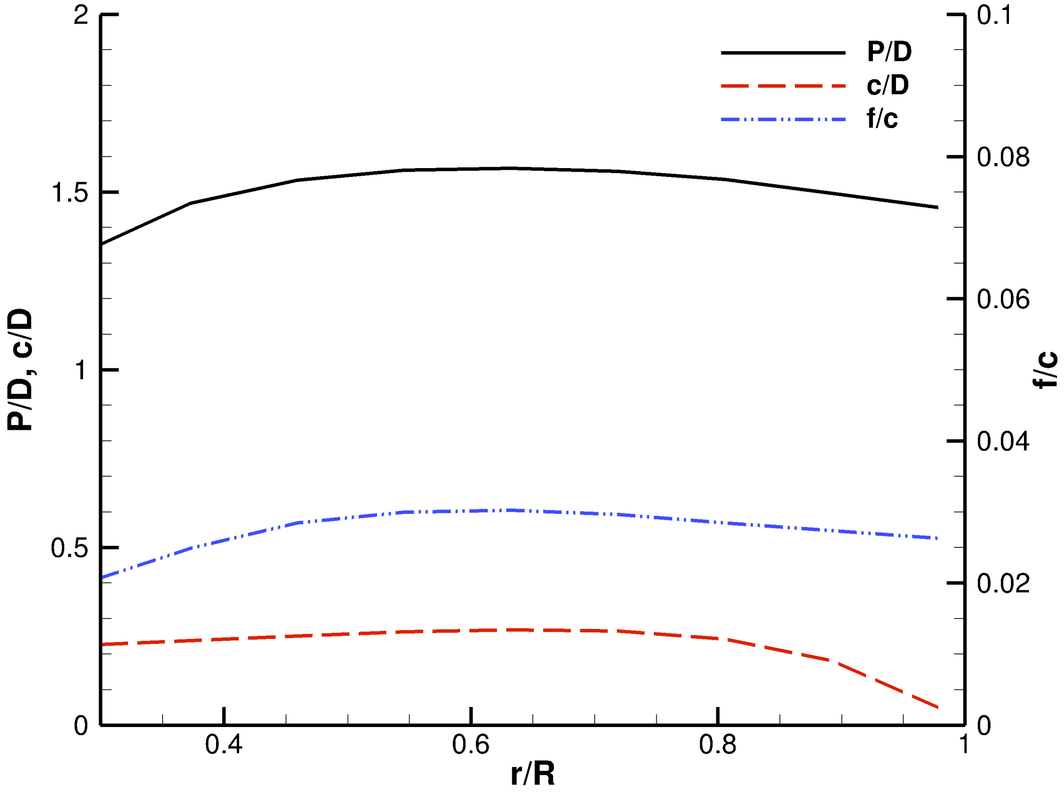

Fig. 5.11 Designed pitch (P/D), chord (c/D) and maximum camber (f/c) distributions for the cavitating case (uniform inflow, 0 skew, CA≤0.3)

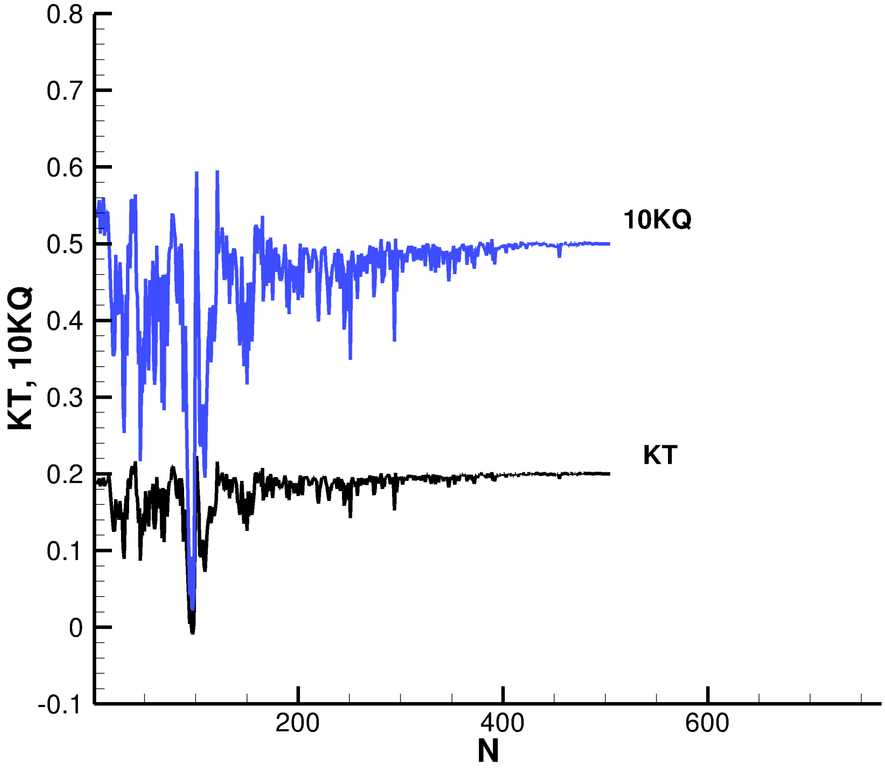

Fig. 5.12 Convergence history for the cavitating case (uniform inflow, 0 skew, CA≤0.3)

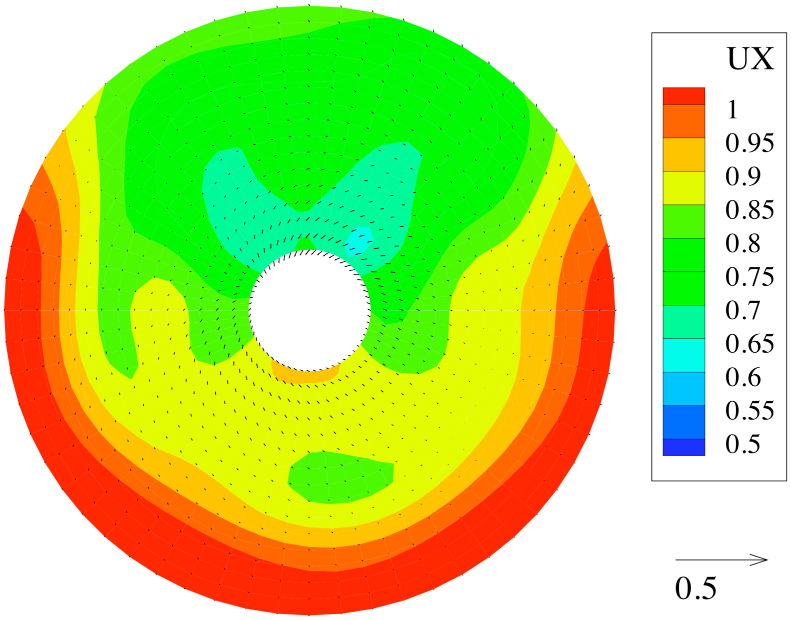

Fig. 5.13 Velocity contour of the non-uniform inflow

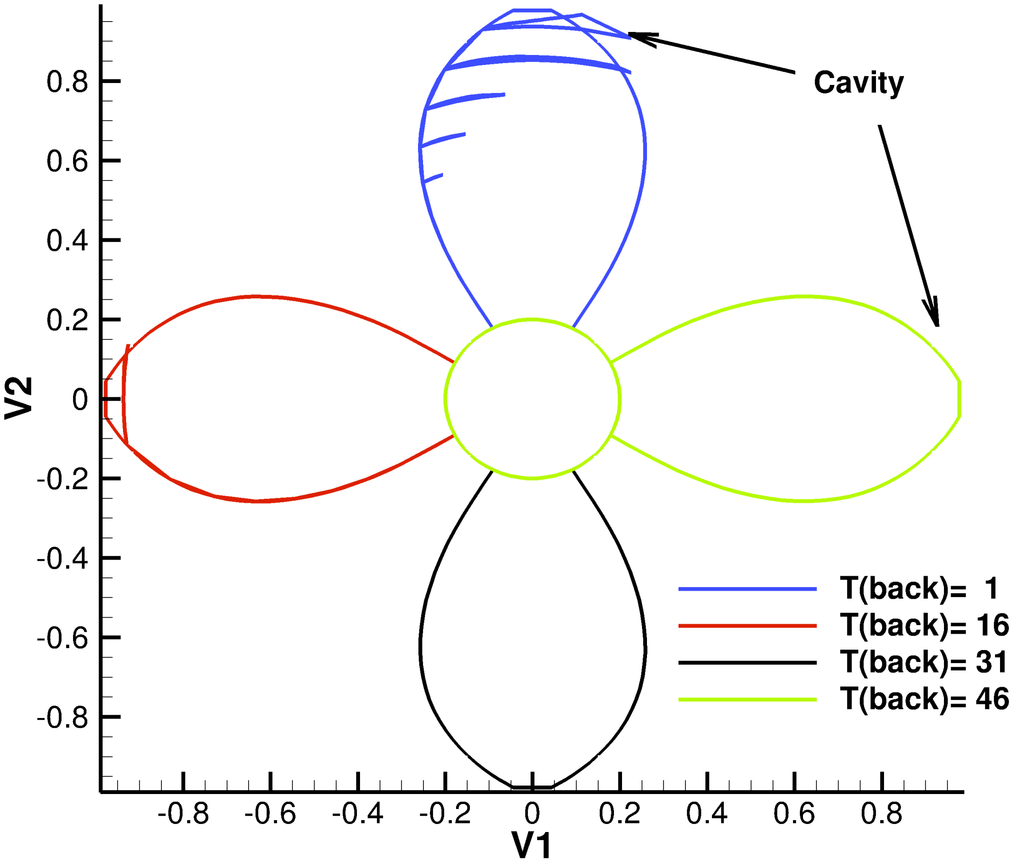

Fig. 5.14 Designed projected blade geometry and cavity pattern at different time steps for the cavitating case (non-uniform inflow, 0 skew, CA≤0.3)

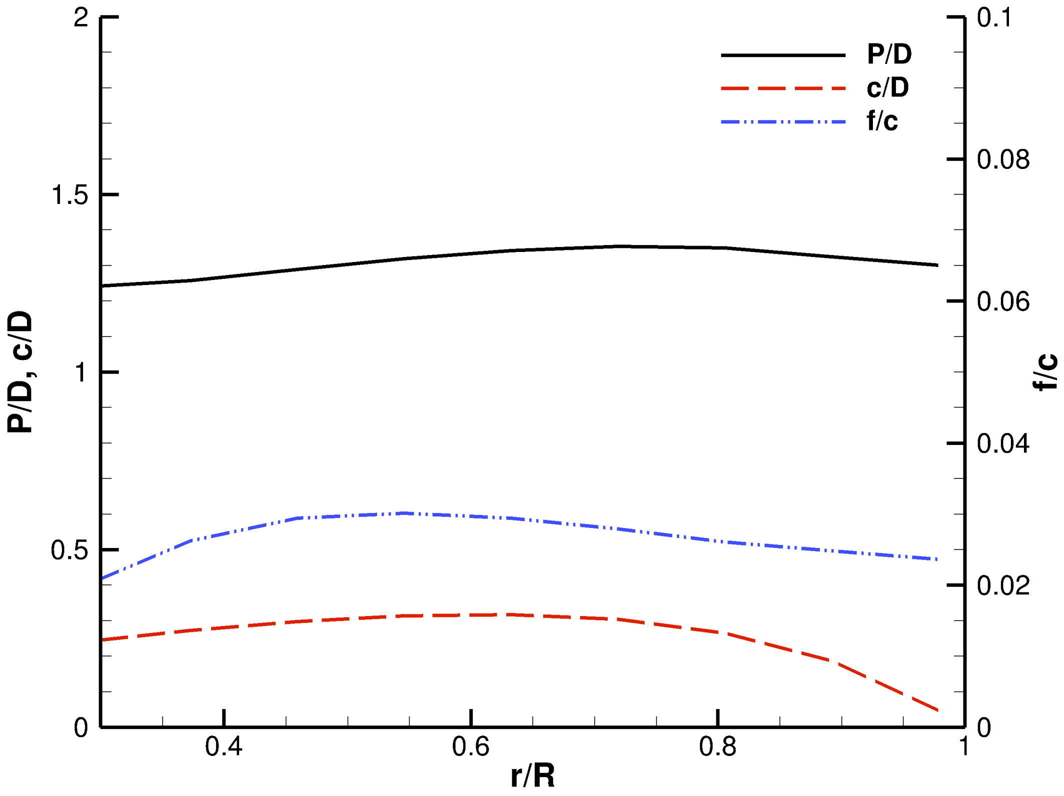

Fig. 5.15 Designed pitch (*P/D*), chord (*c/D*) and maximum camber (*f/c*) distributions for the cavitating case (non-uniform inflow, 0 skew, CA≤0.3)

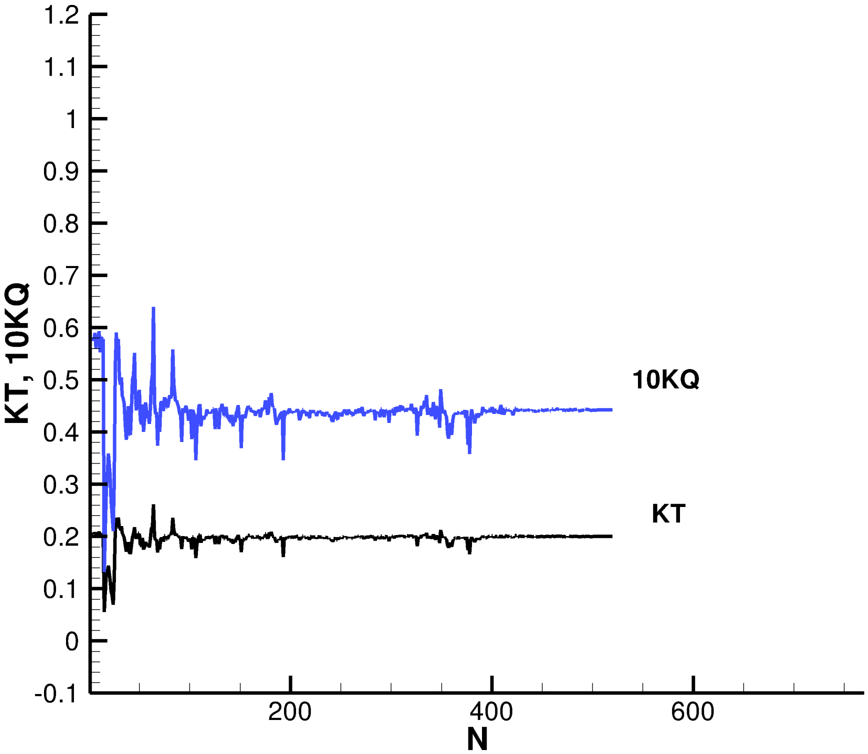

Fig. 5.16 Convergence history for the cavitating case (non-uniform inflow, 0 skew, CA≤0.3)

5.3.2 Skewed propeller design

Skewed propellers, which can reduce the ship vibration and extend the propeller service life by decreasing the blade cavitation erosion, are very common these days. The definition of the skewness is illustrated in Fig. 3.11. A spanwise skew distribution and a thickness distribution as those of a *P5168* propeller are utilized in the propeller design. The modified NACA66 thickness form is adopted. In this research, a 5-bladed cavitating skewed propeller, operating at J=1.0, is designed by CAVOPT-3D with an equality constraint on K_T and an inequality constraint on CA. The specific problem can be addressed as follows:

$$\begin{aligned}&\textit{problem}:\\&\quad \text{minimize} \quad \mathrm{K}_Q\\&\quad \text{subject to:} \quad \mathrm{K}_T = 0.35\\&\qquad\qquad\qquad\ \mathrm{CA} \le 0.3\end{aligned} \tag{5.4}$$

In this design case, the inflow is uniform, the cavitation number σ_n=2.5 and the Froude number Fr=5.0. The converged blade geometry and the corresponding trailing wake is shown in Fig. 5.17 (only the key blade is shown) and the designed pitch (P/D), chord (c/D) and maximum camber (f/c) distributions are shown in Fig. 5.19. The convergence history is illustrated in Fig. 5.20, which indicates that the equality constraint is satisfied at the last iteration, i.e., K_T=0.35, and the converged K_Q is 0.0886. Therefore, the efficiency of the design propeller is η = 0.629. Due to the inequality constraint on CA, the cavitation is allowed in the design procedure, and the cavity patterns of the design propeller at different time steps are shown in Fig. 5.18.

A propeller, which is subjected to the same non-uniform inflow as that in Fig. 5.13, is also designed in this section. The thrust coefficient K_T and torque coefficient K_Q are 0.35 and 0.0812, respectively, and the efficiency is η =0.686. As mentioned in section 5.3.1, the propeller efficiency increases as a result of the decrease of volumetric mean of the inflow wake.

Another two cavitating cases (uniform inflow and non-uniform inflow) with looser CA constraint (CA≤0.6) and the same working conditions are also investigated in this research. The final cavity patterns at different time steps for the design propeller subject to uniform inflow are shown in Fig. 5.24. Fig. 5.25 shows the corresponding designed pitch (P/D), chord (c/D) and maximum camber (f/c) distribution. By comparing Fig. 5.24 with Fig. 5.18, it can be found that the looser CA constraint leads to more cavity on the final designed propeller. As is mentioned in 5.3.1, the efficiency of the propeller can increase by allowing more cavitation on the propeller blades. The converged K_T and K_Q for the higher CA case, which has uniform inflow, are 0.35 and 0.08475, respectively, and the corresponding efficiency is $\eta = 0.657$, which is higher than that of the case with CA≤0.3 and uniform inflow ($\eta = 0.629$). The results for the propeller design with CA≤0.6 and non-uniform inflow are shown in Fig. 5.27~5.29. The K_T and K_Q for this case are 0.35 and 0.077, respectively. And the efficiency is 0.723, which is higher than that of the smaller CA constraint case (CA≤0.3 and non-uniform inflow). The design conditions and all design results for propellers via CAVOPT-3D are tabulated in Table 5.3.

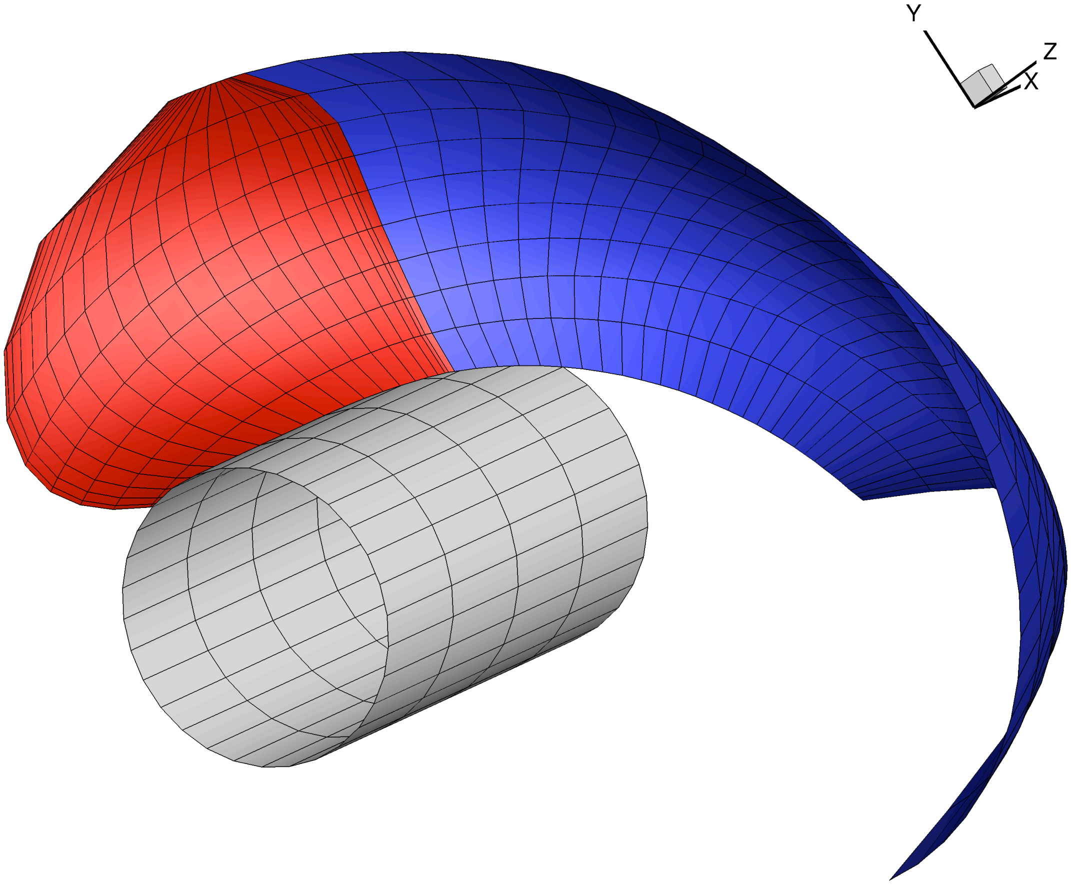

Fig. 5.17 Converged key blade geometry and trailing wake for the skewed propeller design (uniform inflow, K_T=0.35, CA≤0.3)

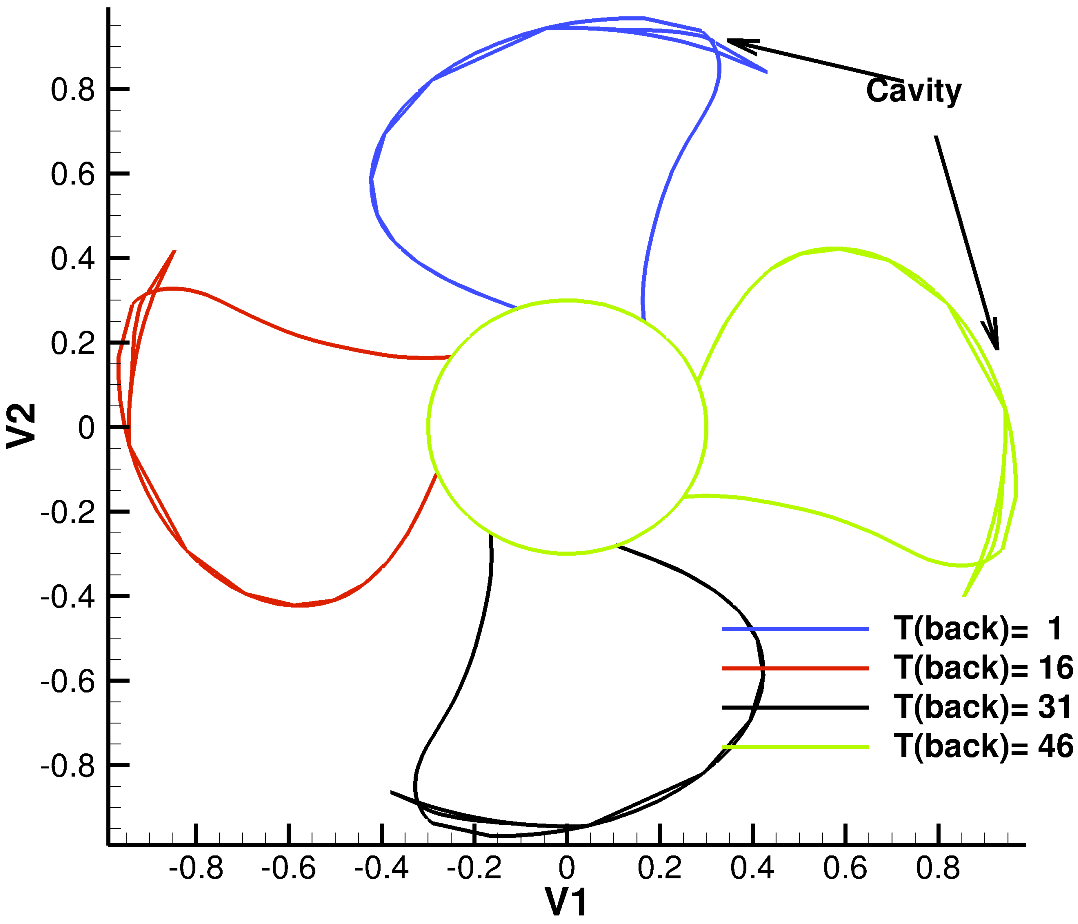

Fig. 5.18 Designed projected blade geometry and cavity patterns at different time steps for the cavitating skewed propeller case (Uniform inflow, K_T=0.35, CA≤0.3)

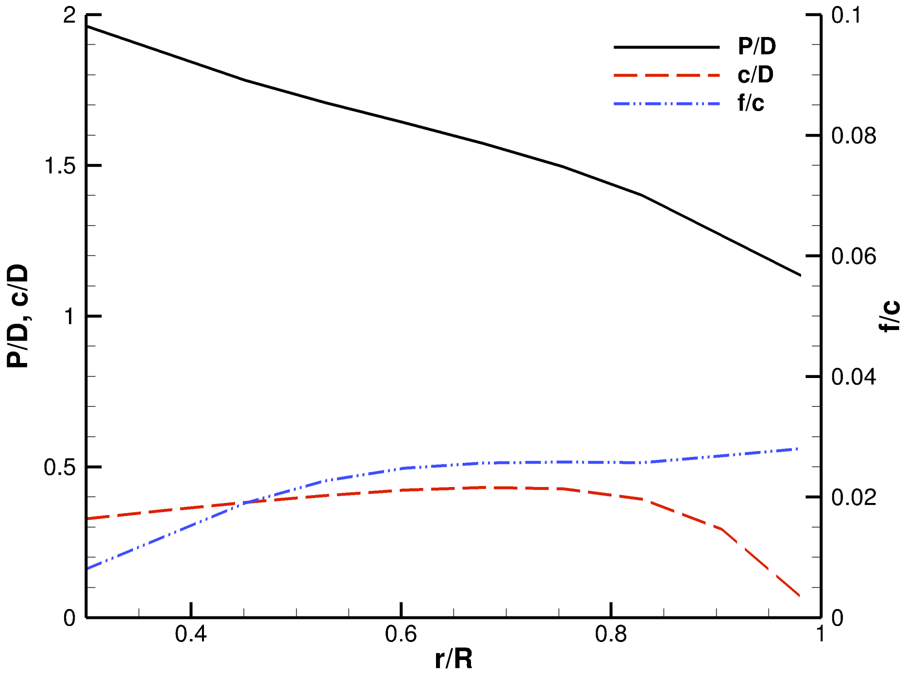

Fig. 5.19 Designed pitch (*P/D*), chord (*c/D*) and maximum camber (*f/c*) distributions for the cavitating skewed propeller. (Uniform inflow, K_T=0.35, CA≤0.3)

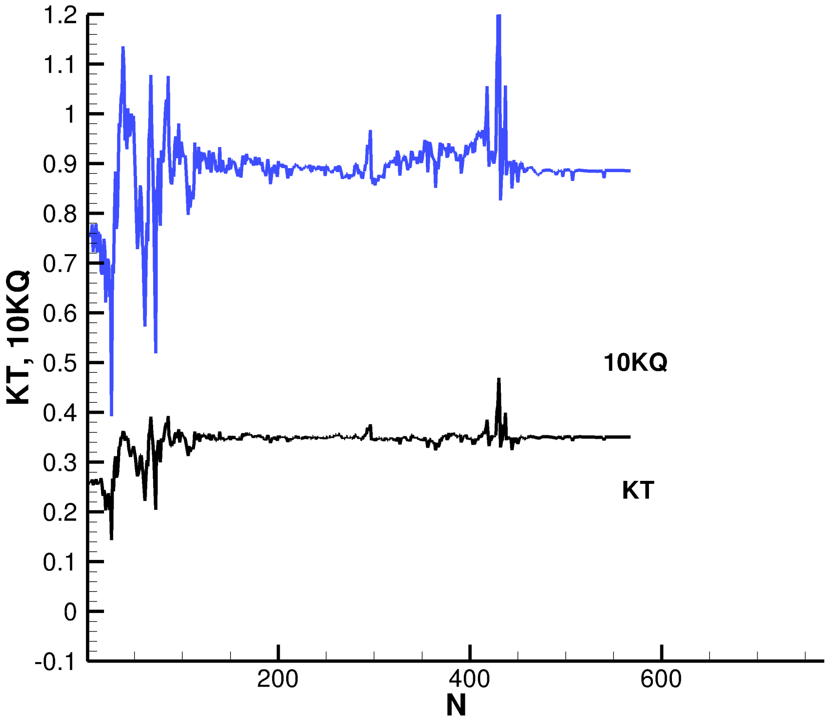

Fig. 5.20 Convergence history for the design of a cavitating skewed propeller by using CAVOPT-3D coupled with MPUF-3A (v3.0) (Uniform inflow, K_T=0.35, CA≤0.3)

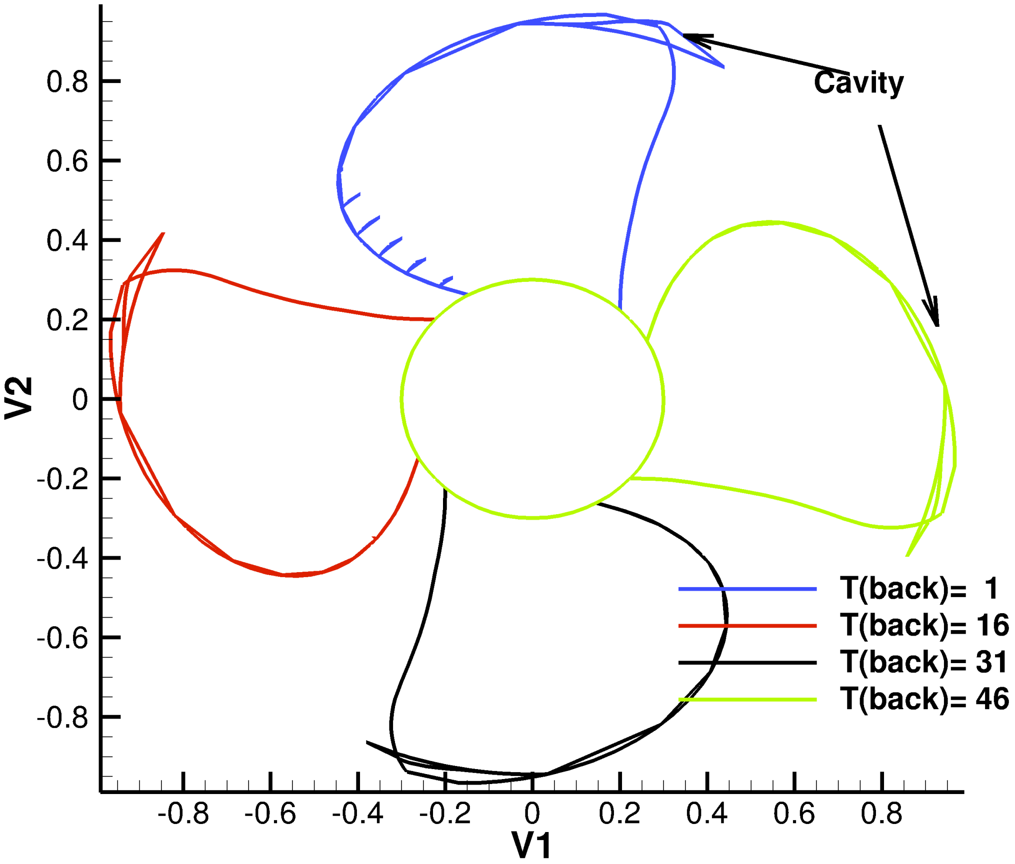

Fig. 5.21 Designed projected blade geometry and cavity patterns at different time steps for the cavitating skewed propeller case (Non-uniform inflow, K_T=0.35, CA≤0.3)

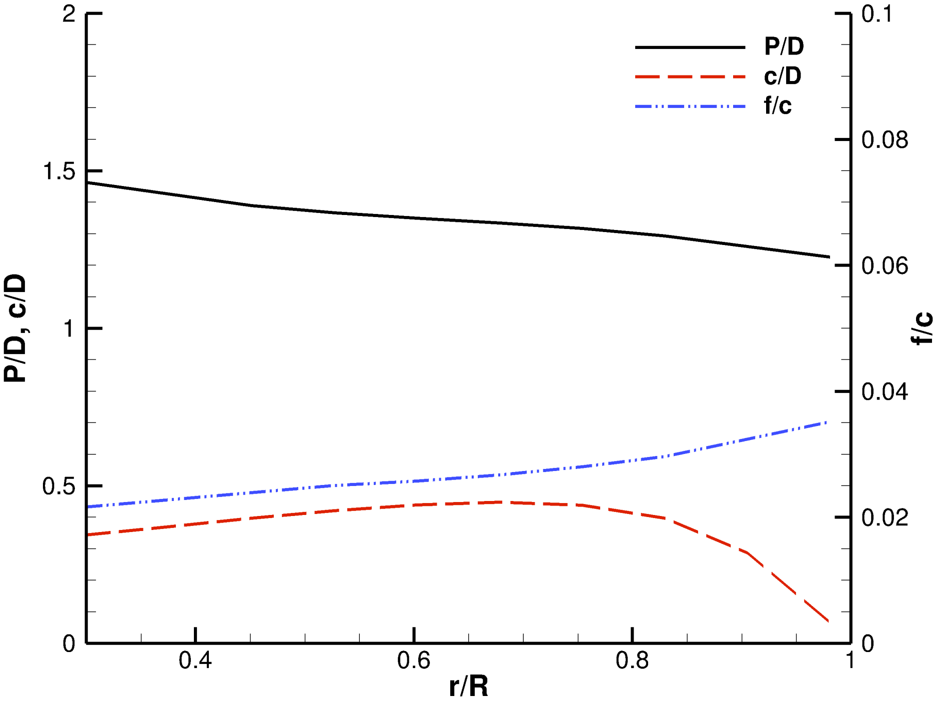

Fig. 5.22 Designed pitch (*P/D*), chord (*c/D*) and maximum camber (*f/c*) distributions for the cavitating skewed propeller. (Non-uniform inflow, K_T=0.35, CA≤0.3)

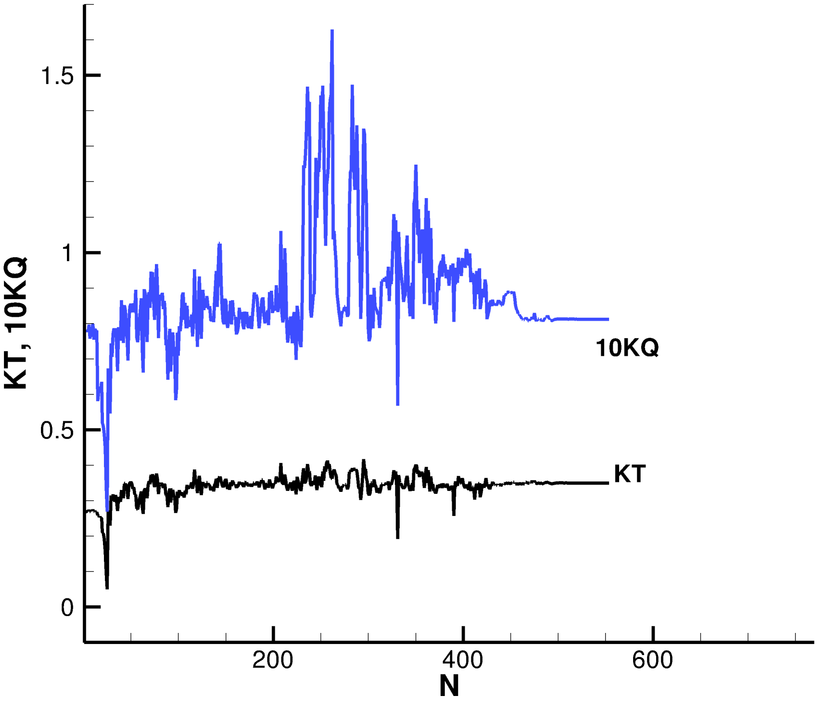

Fig. 5.23 Convergence history for the design of a cavitating skewed propeller by using CAVOPT-3D coupled with MPUF-3A (v3.0) (Non-uniform inflow, K_T=0.35, CA≤0.3)

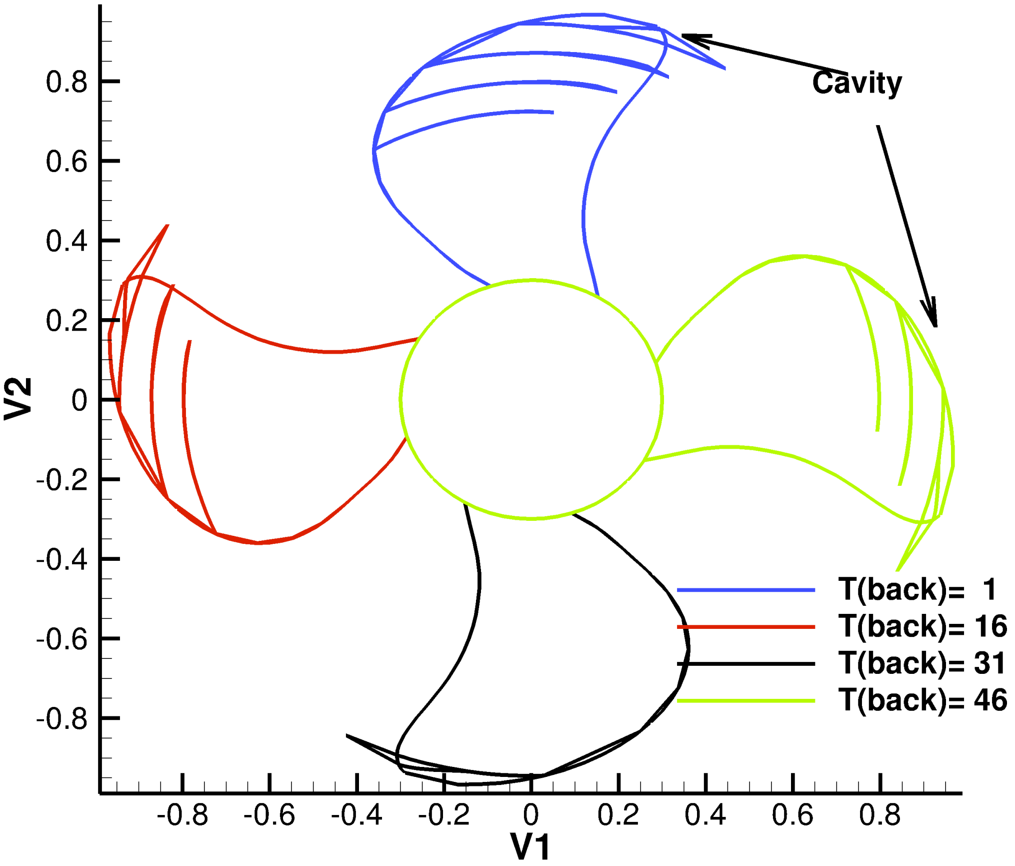

Fig. 5.24 Designed projected blade geometry and cavity patterns at different time steps for the cavitating skewed propeller with high CA (Uniform inflow, K_T=0.35, CA≤0.6)

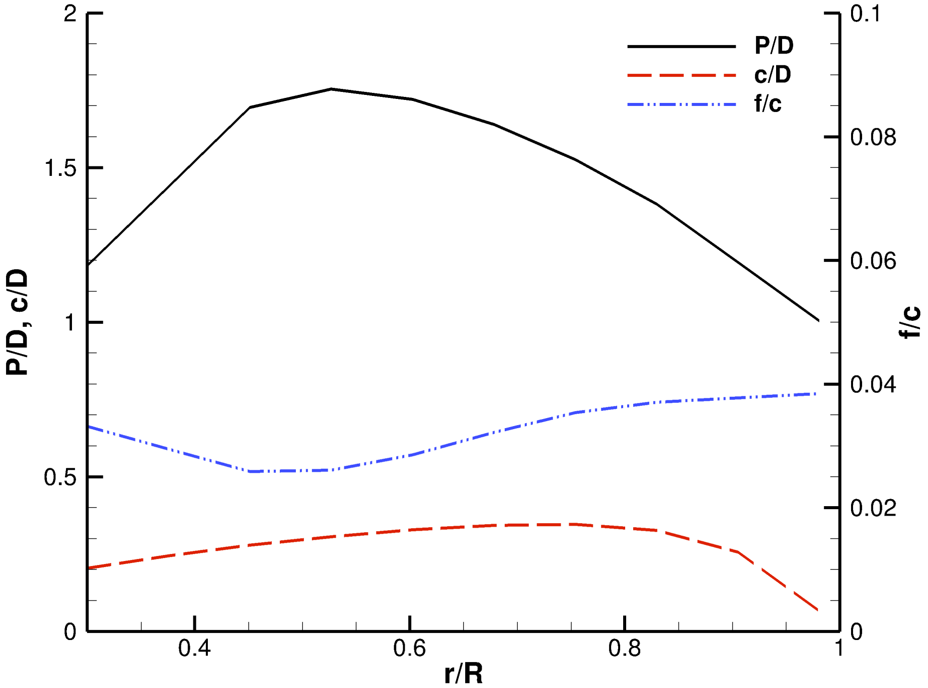

Fig. 5.25 Designed pitch (*P/D*), chord (*c/D*) and maximum camber (*f/c*) distributions for the cavitating skewed propeller. (Uniform inflow, K_T=0.35, CA≤0.6)

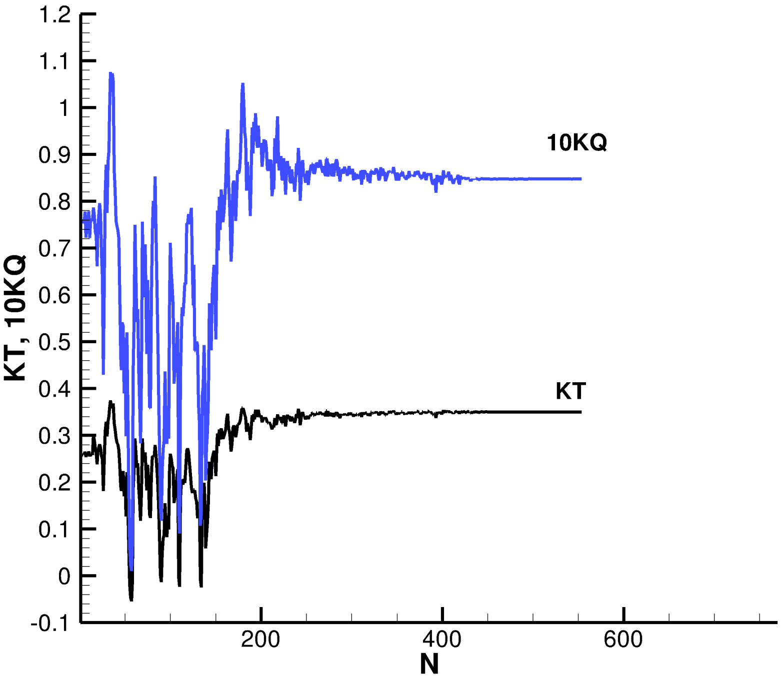

Fig. 5.26 Convergence history for the design of a cavitating skewed propeller by using CAVOPT-3D coupled with MPUF-3A (v3.0) (Uniform inflow, K_T=0.35, CA≤0.6)

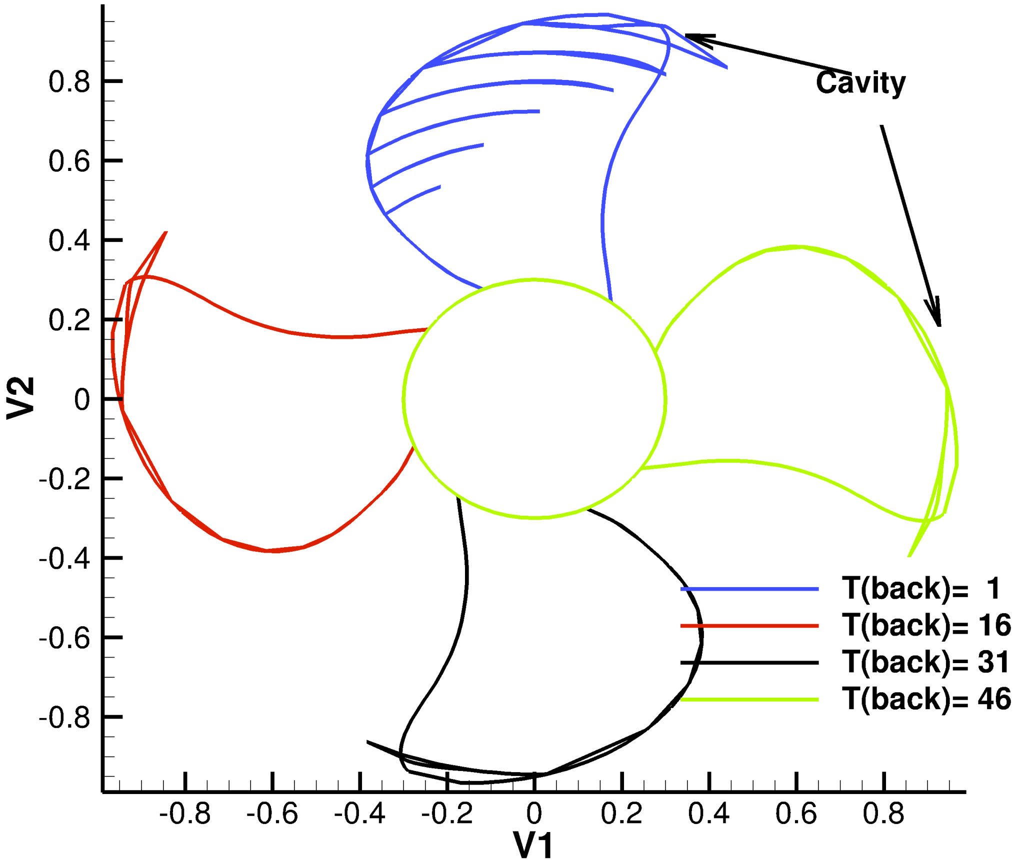

Fig. 5.27 Designed projected blade geometry and cavity patterns at different time steps for the cavitating skewed propeller with high CA (Non-uniform inflow, K_T=0.35, CA≤0.6)

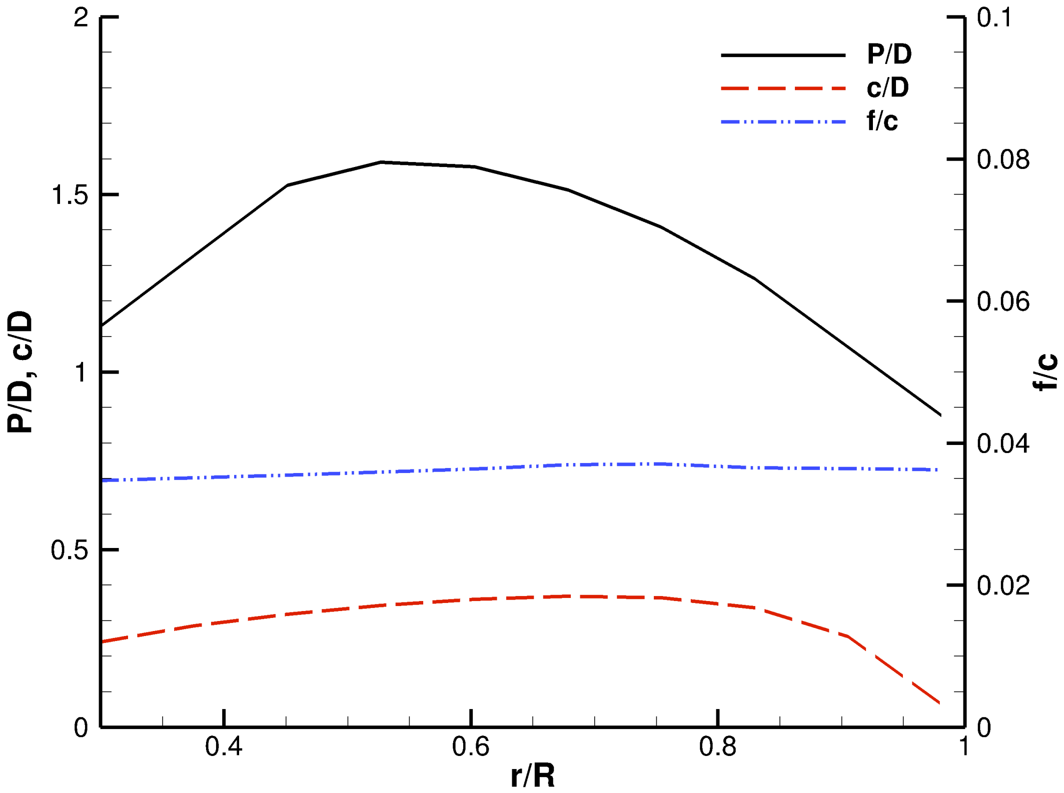

Fig. 5.28 Designed pitch (*P/D*), chord (*c/D*) and maximum camber (*f/c*) distributions for the cavitating skewed propeller. (Non-uniform inflow, K_T=0.35, CA≤0.6)

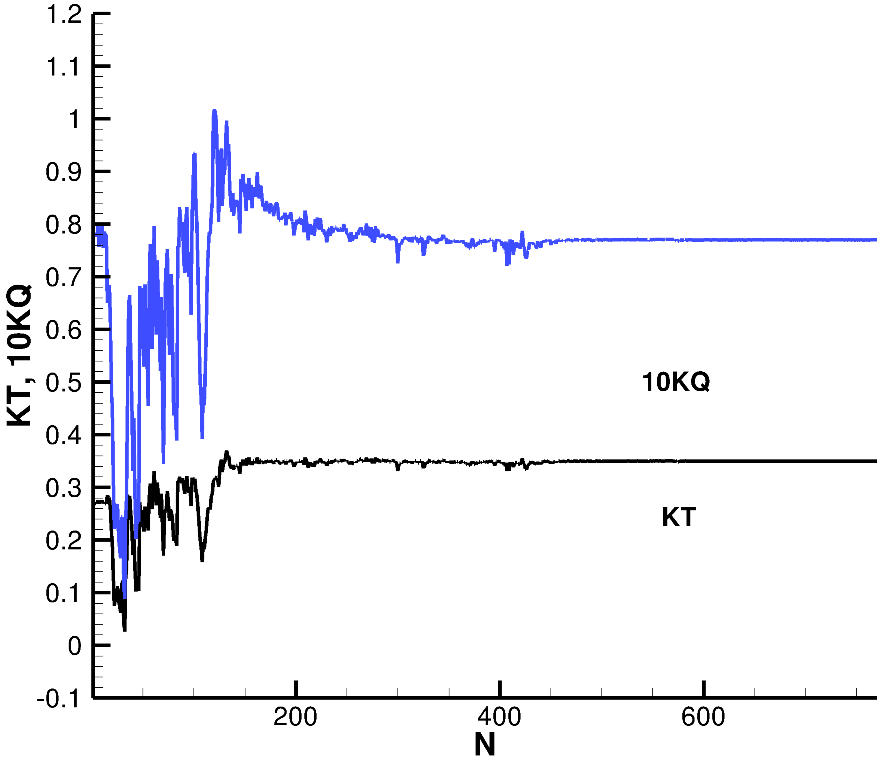

Fig. 5.29 Convergence history for the design of a cavitating skewed propeller by using CAVOPT-3D coupled with MPUF-3A (v3.0) (Non-uniform inflow, K_T=0.35, CA≤0.6)

Table 5.3 Four propeller design cases by CAVOPT-3D coupled with MPUF-3A (v3.0)

	Non-skewed (uniform)	**Non-skewed (non-uniform)**	**Skewed (uniform, CA=0.3)**	**Skewed (nonuniform, CA=0.3)**	**Skewed (uniform CA=0.6)**	**Skewed (nonuniform, CA=0.6)**
J	1.2	1.2	1. 0	1.0	1.0	1.0
σ_n Fr	2.5 5.0	2.5 5.0	2.5 5.0	2.5 5.0	2.5 5.0	2.5 5.0
Blade Number	3	3	5	5	5	5
CA≤	0.3	0.3	0.3	0.3	0.6	0.6
Design K_T K_Q η	0.200 0.0500 0. 764	0.2 0.0442 0.864	0.35 0.0886 0.629	0.35 0.0812 0.686	0.35 0.0848 0.657	0.35 0.0770 0.723

Chapter 6

Conclusions and Recommendations

6.1 CONCLUSIONS

A lifting line optimization method (LLOPT), is developed to design a single tidal turbine and a contra-rotating tidal turbine. For a single tidal turbine, the results of LLOPT cannot approach the Betz limit with decreasing advance ratio and increasing number of blades. Another method, LLOPT-BASE, is then developed to achieve an improved circulation distribution, one that not only results to a more efficient turbine, but also produces results which approach the Betz limit with decreasing advance ratio and increasing number of blades. The inability of LLOPT to recover the Betz limit is attributed to the assumption that the vortex horseshoe influence coefficients are independent of the vortex strengths. This assumption is not valid since the vortex strengths affect the wake shape, and thus the influence coefficients of the horseshoes. Nevertheless, when LLOPT is applied to a contra-rotating tidal turbine, the Betz limit can be reached as the advance ratio J approaches zero.

Three numerical analysis methods, a boundary element method PROPCAV, a vortex lattice method MPUF-3A and a RANS solver FLUENT are applied to predict the performance of tidal current turbines. The results from these methods were found to be in reasonable agreement with the experimental measurements. However, it takes up to 5 hours for FLUENT to finish the fully wetted analysis, while 1 minute and 5 minutes are enough for PROPCAV (blade pitch wake alignment) and MPUF-3A (unsteady wake alignment), respectively. A coupled viscous/potential flow method is also utilized in order to predict the performance of a marine current turbine subject to non-uniform inflow.

A database-searching design method CAVOPT-BASE is applied to maximize the power coefficient of a turbine as well as to reduce or to eliminate the cavitation amount. It should be noted that the increase of the efficiency of the turbine might lead to an increase of thrust coefficient. This increase in thrust coefficient could be avoided by adding an additional constraint that specifies the maximum thrust coefficient for the design case. The effectiveness of the design method naturally depends on the accuracy of the results from the predictive methods (used in creating the database) and on the size of the database.

A more advanced design method (CAVOPT-3D) is modified to work for turbine cases. In this method, the final optimized turbine geometry can be reached without generating a turbine performance database. The method can automatically search for the most efficient turbine geometry by using second order Taylor expansions of results predicted by MPUF-3A.

A design procedure for turbine blades is proposed in this research. A base blade geometry is generated by combining a given section profile and the circulation distribution from LLOPT-BASE. The base geometry is analyzed via a vortex lattice method (MPUF-3A). A performance database for a base turbine geometry is generated to produce a more efficient turbine geometry via using CAVOPT-BASE. As is shown by the numerical results in this thesis, this design procedure works well for designing a tidal turbine. The CAVOPT-BASE optimization procedure can also consider the viscous effect by applying a friction coefficient on the blade in MPUF-3A. In addition, when designing a turbine in shallow water, the cavitation can be reduced or eliminated by adding a constraint on the minimum pressure in CAVOPT-BASE.

Some propeller design cases are also investigated in this research by coupling CAVOPT-BASE with the latest version of PROPCAV (v3.0), and CAVOPT-3D with the latest version of MPUF-3A (v3.0). Both fully wetted propeller designs and cavitating propeller designs are produced by CAVOPT-BASE in Section 5.2. In Section 5.3, CAVOPT-3D is used to design non-skewed and skewed propeller blades, and the influence of the inflow wake and of the maximum allowable back cavitation constraint (CA) on the performance of the designed propellers is shown.

6.2 RECOMMENDATIONS

An important issue with the potential flow method is the occurrence of flow separation at large angle of attack. For turbines with low pitch angles, the potential flow methods (MPUF-3A and PROPCAV) will over predict the thrust and power coefficients due to the ignorance of flow separation. A numerical model, which includes the flow separation effects, could make the vortex lattice method and the boundary element method provide predictions, which are closer to experiments.

In this research, the viscous effect is included by exerting a friction coefficient, C_f, over the fully wetted blade surface. A more efficient and accurate alternative is to couple the potential flow methods with an integral boundary layer solver as was done in (Sun & Kinnas, 2008).

The viscous/potential flow method, which was used in this thesis to study the performance of turbines subject to a non-uniform current, is also very useful for future studies, such as the effect of yaw angle and of the free surface on the turbine performance. Additionally, this method can be applied in the case of turbines where one is operating downstream of the other (contra-rotating turbine), in a similar way as in the case of podded propulsors with for and aft propellers (Kinnas, et al., 2009). The method can also be extended to analyze the performance of a turbine farm, including the interactions among turbines.

For the CAVOPT-BASE method, more design constraints can be added and a larger database can be generated in order not to miss blade geometries with higher efficiency. The method can also be extended to include the effect of non-uniform inflow, as was done in (Deng, 2005) in the case of propellers.

CAVOPT-3D has the advantage of automatically producing the optimum design geometry without generating a performance database. More design cases, with additional constraints, must be tested for both turbines and propellers. Design cases with finer grid (20×18) should also be performed in the future in order to assess the effect of the grid on the final optimum blade geometry.

Appendix A

Influence coefficients for the lifting line theory

In evaluating the influence of the wake on the blades, imagine a helicoidal coordinate system, with one coordinate along the wake helix, one coordinate along the blade (radial), and the third normal to the first two. Far downstream, the wake flow will be independent of the helicoidal coordinate, thus it becomes a two-dimentional problem. This problem was solved by Kawada and Lerbs, independently, and the resulting potential was expressed in terms of infinite sums of modified Bessel functions. By applying the highly accurate asymptotic formulas for the sums of Bessel functions, Wrench developed the following closed form approximations for the induced velocities:

For $r_c < r_v$:

$$\begin{aligned} \overset{=}{u}_a(r_c) &= \frac{Z}{4\pi r_c}(y - 2Zyy_0F_1) \\ \overset{=}{u}_t(r_c) &= \frac{Z^2}{2\pi r_c}y_0F_1 \end{aligned} \qquad \text{(A.1)}$$

For $r_c > r_v$:

$$\begin{aligned} \overset{=}{u}_a(r_c) &= \frac{Z^2}{2\pi r_c}yy_0F_2 \\ \overset{=}{u}_t(r_c) &= \frac{Z}{4\pi r_c}(1 - 2Zy_0F_2) \end{aligned} \qquad \text{(A.2)}$$

where

$$F_1 \approx -\frac{1}{2Zy_0}\left(\frac{1+y_0^2}{1+y^2}\right)^{0.25}\left\{\frac{1}{U^{-1}-1}+\frac{1}{24Z}\left[\frac{9y_0^2+2}{\left(1+y_0^2\right)^{1.5}}+\frac{3y^2-2}{\left(1+y^2\right)^{1.5}}\right]\ln\left(1+\frac{1}{U^{-1}-1}\right)\right\}$$

$$F_2 \approx -\frac{1}{2Zy_0}\left(\frac{1+y_0^2}{1+y^2}\right)^{0.25}\left\{\frac{1}{U-1}-\frac{1}{24Z}\left[\frac{9y_0^2+2}{\left(1+y_0^2\right)^{1.5}}+\frac{3y^2-2}{\left(1+y^2\right)^{1.5}}\right]\ln\left(1+\frac{1}{U-1}\right)\right\} \tag{A.3}$$

And

$$U=\left\{\frac{y_0\left(\sqrt{1+y^2}-1\right)}{y\left(\sqrt{1+y_0^2}-1\right)}\exp\left(\sqrt{1+y^2}-\sqrt{1+y_0^2}\right)\right\}^Z$$

$$y=\frac{r_c}{r_v\tan\beta} \tag{A.4}$$

$$y_0=\frac{1}{\tan\beta}$$

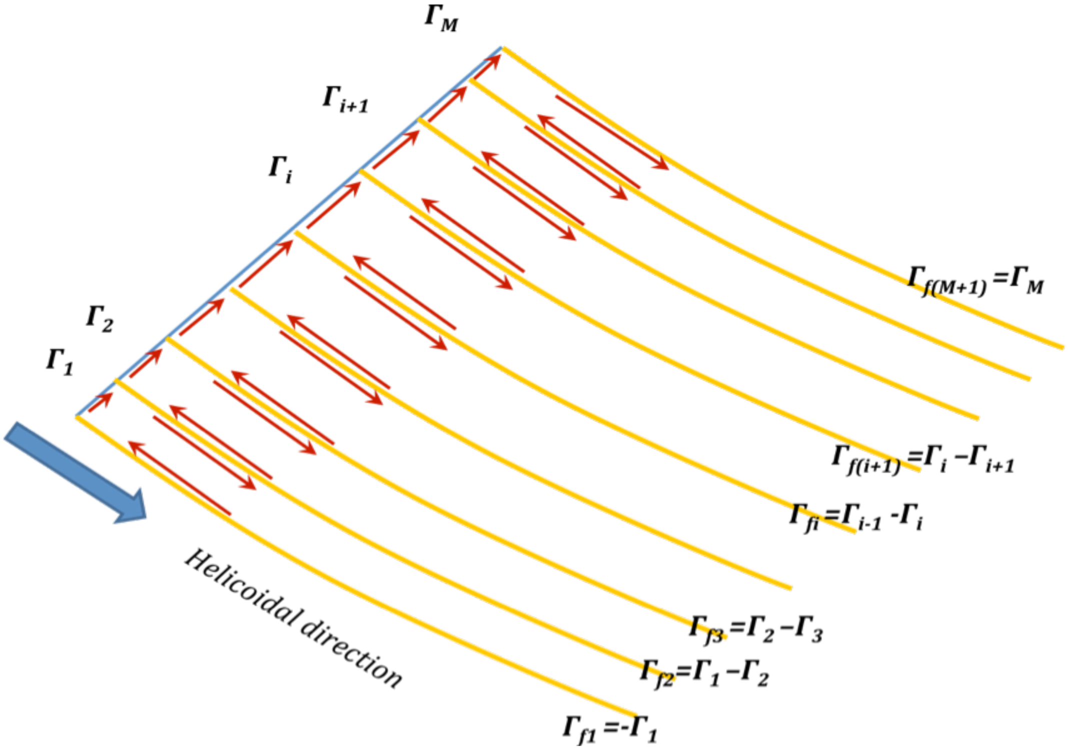

Fig. A.1 Discritized vortex horseshoes of the wake for the key blade

The wake of the key blade can be discretized into M horseshoes as is shown in Fig. A.1. The induced velocities expressed in equation A.1 and A.2 are the velocities induced by a helix circulation tube with unit strength. Given these equations, the axial induced velocity $\bar{u}_a(m,n)$ and the tangential induced velocity $\bar{u}_a(m,n)$ at the m^{th} control point by a helical "horseshoe" vortex surrounding the n^{th} control point could be expressed as follows:

$$\begin{aligned} \bar{u}_a(m,n) &= \bar{\bar{u}}_a\left(r^c_m; r^v_{n+1}\right) - \bar{\bar{u}}_a\left(r^c_m; r^v_n\right) \\ \bar{u}_t(m,n) &= \bar{\bar{u}}_t\left(r^c_m; r^v_{n+1}\right) - \bar{\bar{u}}_t\left(r^c_m; r^v_n\right) \end{aligned} \tag{A.5}$$

Appendix B

Lifting line optimization method for contra-rotating turbines

In a contra-rotating turbine case, not only must the self-induced velocities be calculated, but also the interaction velocities between components. Here, the self-induced velocity is calculated by the same method as is shown in the Appendix A.

B.1 Optimum method for a contra-rotating turbine

For a contra-rotating turbine, efficiency is defined as follows

$$\eta = \frac{P_{mechanical}}{P_{wind}} = \frac{Q_1\omega_1 + Q_2\omega_2}{\rho\pi R^2 \frac{V^3}{2}} \tag{B.1}$$

Where Q_1 and Q_2 denote the torques for the front and back turbines respectively, ω_1 and ω_2 denotes the angular speeds for two turbines.

Figure B.1 shows a combined velocity and force diagram for one component of a contra-rotating turbine. The axial and tangential induced velocity on component j are given by

$$\begin{aligned} u^*_{a_j}(m) &= \sum_{k=1}^{2} u_{a_{j,k}}(m), \qquad & j = 1,2 \\ u^*_{t_j}(m) &= \sum_{k=1}^{2} u_{t_{j,k}}(m), \qquad & j = 1,2 \end{aligned} \tag{B.2}$$

where

$$\frac{u_{a_{j,k}}(m)}{V} = \sum_{n=1}^{M_k} \overline{\Gamma}_k(n)\overset{=*}{u}_{a_{J,K}}(m,n), \qquad m = 1,\ldots,M_j \qquad \text{j,k=1,2}$$
$$\frac{u_{t_{j,k}}(m)}{V} = \sum_{n=1}^{M_k} \overline{\Gamma}_k(n)\overset{=*}{u}_{t_{j,k}}(m,n), \qquad m = 1,\ldots,M_j \qquad \text{j,k=1,2} \tag{B.3}$$

M_k is the element number for component *k*. $\overline{\Gamma}_k(n)$ is the normalized circulation at element n on component k. $\overset{=*}{u}_{a_{J,K}}(m,n)$ and $\overset{=*}{u}_{a_{J,K}}(m,n)$ are the normalized axial and tangential induced velocities on control point m (on component *j*) from *n*th horseshoe (on component *k*). Thus they are self-induced velocities whenever *j=k*, otherwise they are the interaction velocities. $V_j^*(r)$ and β_{i_j} are the total velocity and pitch angle after wake alignment, respectively.

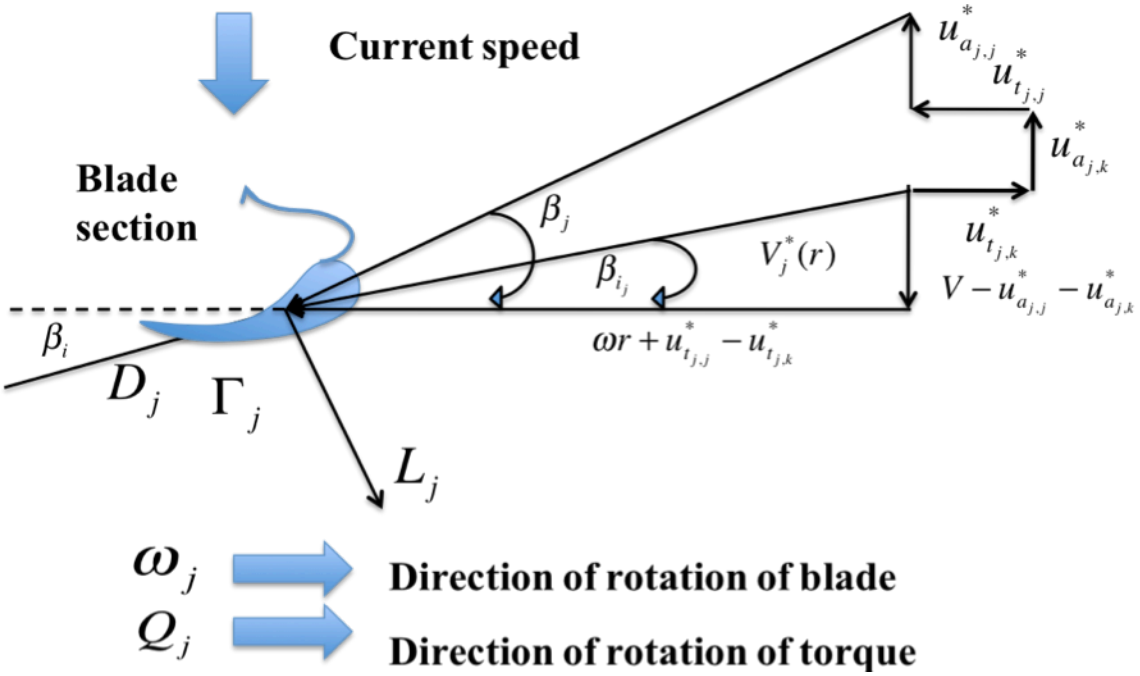

Fig. B.1 Combined velocity and force diagram for a component of a contra-rotating turbine

Following a similar procedure for a single turbine and ignoring the viscous effect, we can get the total power

$$P_{total} = \rho Z_1 \omega_1 \int_{r_{h1}}^{R_1} \Big[(V - u^*_{a_{1,1}} - u^*_{a_{1,2}}) \Gamma_1 \Big] r_1 dr_1 + \rho Z_2 \omega_2 \int_{r_{h2}}^{R_2} \Big[(V - u^*_{a_{2,2}} - u^*_{a_{2,1}}) \Gamma_2 \Big] r_2 dr_2 \tag{B.4}$$

In the discretized form, the length scale is normalized by R_1. We have the expression for Q as follows

$$\begin{aligned}
Q &= \rho Z_1 \omega_1 \sum_{m=1}^{M_1} \Big[V - u^*_{a_{1,1}}(m) - u^*_{a_{1,2}}(m) \Big] r_1(m) \Gamma_1(m) \Delta r_1 \\
&\quad + \rho Z_2 \omega_2 \sum_{m=1}^{M_2} \Big[V - u^*_{a_{2,2}}(m) - u^*_{a_{2,1}}(m) \Big] r_2(m) \Gamma_2(m) \Delta r_2 \\
&= \rho Z_2 V^2 R_1^3 \omega_1 \sum_{m=1}^{M_1} \left[1 - \frac{u^*_{a_{1,1}}(m)}{V} - \frac{u^*_{a_{1,2}}(m)}{V} \right] \frac{r_1(m)}{R_1} \frac{\Gamma_1(m)}{V R_1} \frac{\Delta r_1}{R_1} \\
&\quad + \rho Z_1 V^2 R_1^3 \omega_2 \sum_{m=1}^{M_2} \left[1 - \frac{u^*_{a_{2,2}}(m)}{V} - \frac{u^*_{a_{2,1}}(m)}{V} \right] \frac{r_2(m)}{R_1} \frac{\Gamma_2(m)}{V R_1} \frac{\Delta r_2}{R_1} \\
&= \rho Z_1 V^2 R_1^3 \overline{\Delta r_1} \omega_1 \sum_{m=1}^{M_1} \left[1 - \frac{u^*_{a_{1,1}}(m)}{V} - \frac{u^*_{a_{1,2}}(m)}{V} \right] \bar{r}_1(m) \bar{\Gamma}_1(m) \\
&\quad + \rho Z_2 V^2 R_1^3 \overline{\Delta r_2} \omega_2 \sum_{m=1}^{M_2} \left[1 - \frac{u^*_{a_{2,2}}(m)}{V} - \frac{u^*_{a_{2,1}}(m)}{V} \right] \bar{r}_2(m) \bar{\Gamma}_2(m) \\
&= \rho Z_1 V^2 R_1^3 \overline{\Delta r_1} \omega_1 \sum_{m=1}^{M} \left[1 - \sum_{n=1}^{M_1} \bar{\Gamma}_1(n) \overset{=}{u}_{a_{1,1}}(m,n) \text{-} \sum_{n=1}^{M_2} \bar{\Gamma}_2(n) \overset{=}{u}_{a_{1,2}}(m,n) \right] \bar{r}_1(m) \bar{\Gamma}_1(m) \\
&\quad + \rho Z_2 V^2 R_2^3 \overline{\Delta r_2} \omega_2 \sum_{m=1}^{M_2} \left[1 - \sum_{n=1}^{M_2} \bar{\Gamma}_2(n) \overset{=}{u}_{a_{2,2}}(m,n) \text{-} \sum_{n=1}^{M_1} \bar{\Gamma}_1(n) \overset{=}{u}_{a_{2,1}}(m,n) \right] \bar{r}_2(m) \bar{\Gamma}_2(m)
\end{aligned} \tag{B.5}$$

In order to obtain maximum P_{power} with respect to $\bar{\Gamma}_j(m)$, simply first-order necessary condition is applied. After first derivation and let it be 0, We get $\frac{\partial P_{power}}{\partial \bar{\Gamma}_1} = 0, \frac{\partial P_{power}}{\partial \bar{\Gamma}_2} = 0$

That is

$$\begin{aligned}
&\sum_{n=1}^{M1}\left[\bar{r}_1(i)\overset{=}{u}_{a_{1,1}}\left(i,n\right)+\bar{r}_1(n)\overset{=}{u}_{a_{1.1}}\left(n,i\right)\right]\bar{\Gamma}_1(n)\\
&\quad+\sum_{n=1}^{M2}\left[\bar{r}_1(i)\overset{=}{u}_{a_{1,2}}\left(i,n\right)+\frac{\omega_2}{\omega_1}\frac{Z_2}{Z_1}\frac{\Delta r_2}{\Delta r_1}\bar{r}_2(n)\overset{=}{u}_{a_{2.1}}\left(n,i\right)\right]\bar{\Gamma}_2(n)=\bar{r}_1(i)\\
&\sum_{n=1}^{M2}\left[\bar{r}_2(i)\overset{=}{u}_{a_{2,2}}\left(i,n\right)+\bar{r}_2(n)\overset{=}{u}_{a_{2.2}}\left(n,i\right)\right]\bar{\Gamma}_2(n)\\
&\quad+\sum_{n=1}^{M1}\left[\bar{r}_2(i)\overset{=}{u}_{a_{2,1}}\left(i,n\right)+\frac{\omega_1}{\omega_2}\frac{Z_1}{Z_2}\frac{\Delta r_1}{\Delta r_2}\bar{r}_1(n)\overset{=}{u}_{a_{1.2}}\left(n,i\right)\right]\bar{\Gamma}_1(n)=\bar{r}_2(i)
\end{aligned}\tag{B.6}$$

This is a linear system with $M_1 + M_2$ equations. Any linear system solver can be used here. When the distribution of circulation has been generated, the efficiency for the contra-rotating turbine can be calculated by $\eta_{total}=\eta_1+\eta_2$, in which η_1 and η_2 can be calculated by a similar procedure as that for a single turbine.

B.2 Procedures of circulation distribution calculation for a contra-rotating turbine

Step 0, Let $\tan\beta_{i_1} = \dfrac{V}{\omega_1 r_1}, \tan\beta_{i_2} = \dfrac{V}{\omega_2 r_2}$, compute $\overset{=*}{u}_{a_{j,k}}\left(m,n\right)$ and $\overset{=*}{u}_{t_{j,k}}\left(m,n\right)$, let k = 0.

Step 1, Solve the M_1+M_2 linear system (equ B.6)

Step 2, Compute $\dfrac{u_{a_{j,k}}(m)}{V}$ via $\dfrac{u_{a_{j,k}}(m)}{V} = \sum_{n=1}^{M_k}\bar{\Gamma}_k(n)\overset{=*}{u}_{a_{J,K}}(m,n)$; compute $\dfrac{u_{t_{j,k}}(m)}{V}$ via

$$\frac{u_{t_{j,k}}(m)}{V} = \sum_{n=1}^{M_k}\bar{\Gamma}_k(n)\overset{=*}{u}_{t_{j,k}}(m,n)$$

Step 3, Update $\tan\beta_i$ at control points via

$$\tan\beta_{i_1} = \frac{V - u_{a_{1,1}} - u^*_{a_{1,2}}}{\omega_1 r_1 + u_{t_{1,1}} - u^*_{t_{1,2}}} = \frac{1 - \frac{u^*_{a_{1,1}}}{V} - \frac{u^*_{a_{1,2}}}{V}}{\frac{\omega_1 r_1}{V} + \frac{u^*_{t_{1,1}}}{V} - \frac{u^*_{t_{1,2}}}{V}}, \tan\beta_{i_2} = \frac{V - u_{a_{2,2}} - u^*_{a_{2,1}}}{\omega_2 r_2 + u_{t_{2,2}} - u^*_{t_{2,1}}} = \frac{1 - \frac{u^*_{a_{2,2}}}{V} - \frac{u^*_{a_{2,1}}}{V}}{\frac{\omega_2 r}{V} + \frac{u^*_{t_{2,2}}}{V} - \frac{u^*_{t_{2,1}}}{V}},$$

if $\dfrac{u^*_{t_{j,k}}}{V} > 0$; or via

$$\tan\beta_{i_1} = \frac{V - u_{a_{1,1}} - u^*_{a_{1,2}}}{\omega_1 r_1 - u_{t_{1,1}} + u^*_{t_{1,2}}} = \frac{1 - \frac{u^*_{a_{1,1}}}{V} - \frac{u^*_{a_{1,2}}}{V}}{\frac{\omega_1 r}{V} - \frac{u^*_{t_{1,1}}}{V} + \frac{u^*_{t_{1,2}}}{V}}, \tan\beta_{i_2} = \frac{V - u_{a_{2,2}} - u^*_{a_{2,1}}}{\omega_2 r_2 - u_{t_{2,2}} + u^*_{t_{2,1}}} = \frac{1 - \frac{u^*_{a_{2,2}}}{V} - \frac{u^*_{a_{2,1}}}{V}}{\frac{\omega_2 r}{V} - \frac{u^*_{t_{2,2}}}{V} + \frac{u^*_{t_{2,1}}}{V}},$$

if $\frac{u^*_{t_{j,k}}}{V} < 0$.

Step 4, Update $\tan\beta_i$ at vortex points via interpolation and extrapolation[5].

Step 5, Compute $\overset{=*}{u}_{a_{j,k}}(m,n)$ and $\overset{=*}{u}_{t_{j,k}}(m,n)$, let k= k+1; goto step 1.

Stop criteria

Any standard nonlinear programming stop criteria will be applicable. Here, simply $\left\|\Gamma_{k+1} - \Gamma_k\right\| < \varepsilon$ was used.

Appendix C

Data for the section that is used in the design procedure

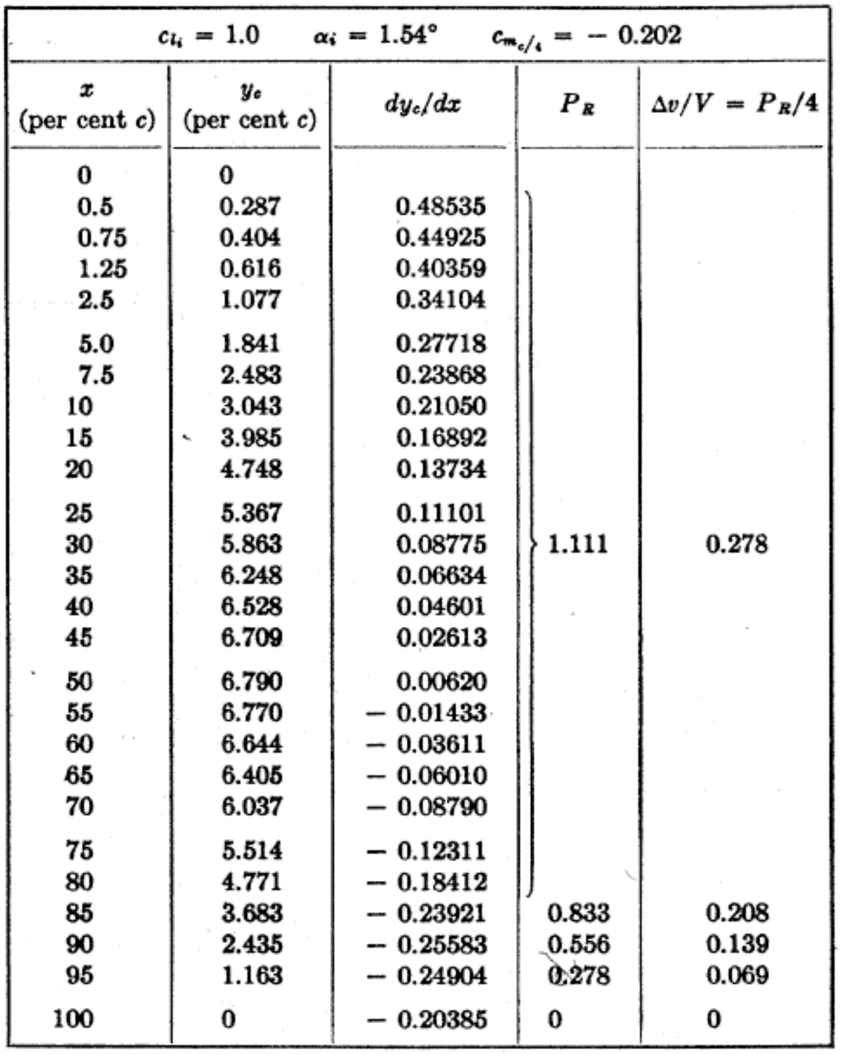

$c_{l_i} = 1.0$ $\alpha_i = 1.54°$ $c_{m_{c/4}} = -0.202$

x (per cent c)	y_c (per cent c)	dy_c/dx	P_R	$\Delta v/V = P_R/4$
0	0			
0.5	0.287	0.48535	1.111	0.278
0.75	0.404	0.44925		
1.25	0.616	0.40359		
2.5	1.077	0.34104		
5.0	1.841	0.27718		
7.5	2.483	0.23868		
10	3.043	0.21050		
15	3.985	0.16892		
20	4.748	0.13734		
25	5.367	0.11101		
30	5.863	0.08775		
35	6.248	0.06634		
40	6.528	0.04601		
45	6.709	0.02613		
50	6.790	0.00620		
55	6.770	− 0.01433		
60	6.644	− 0.03611		
65	6.405	− 0.06010		
70	6.037	− 0.08790		
75	5.514	− 0.12311		
80	4.771	− 0.18412		
85	3.683	− 0.23921	0.833	0.208
90	2.435	− 0.25583	0.556	0.139
95	1.163	− 0.24904	0.278	0.069
100	0	− 0.20385	0	0

Fig. C.1 Data for NACA Mean Line a=0.8

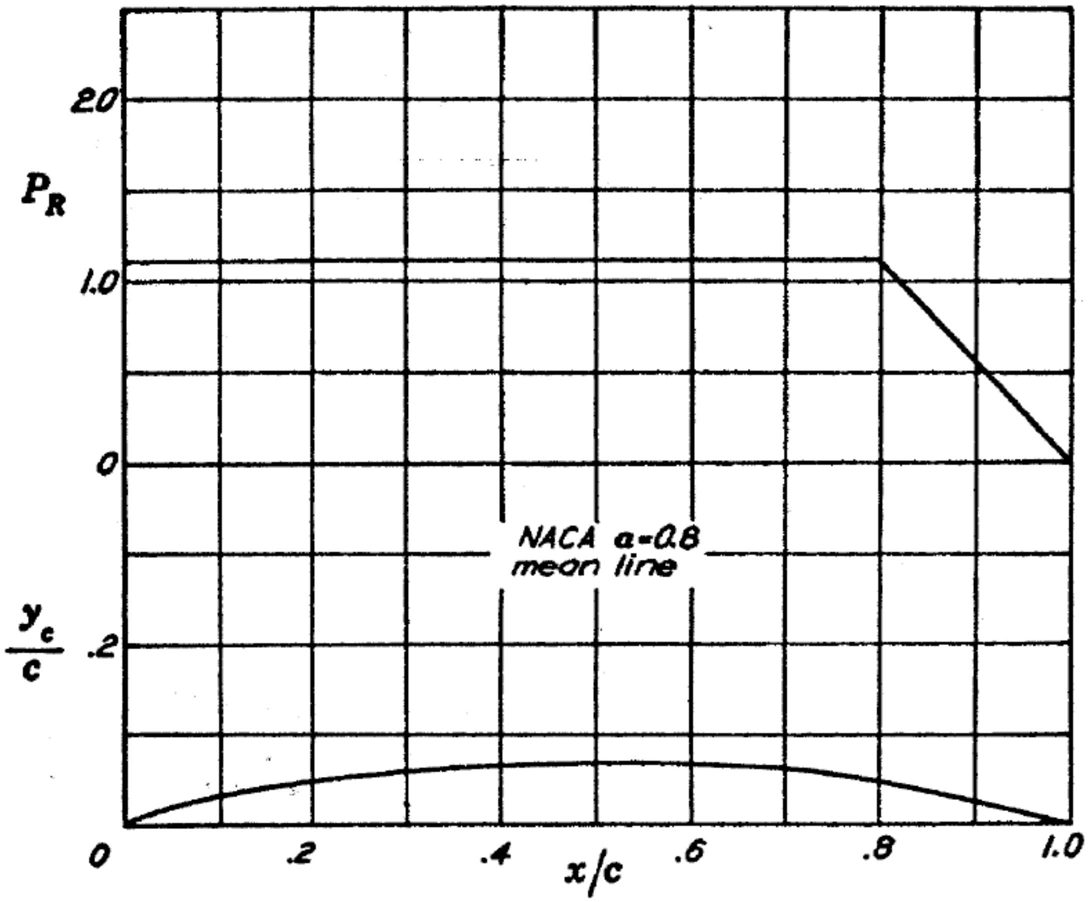

Fig .C.2 NACA Mean Line a=0.8 camber form

References

Abbott, I., & Von Doenhoff, A. (1959). *Theory of wing sections: including a summary of airfoil data*: Courier Dover Publications.

ANSYS. Inc (2009). ANSYS FLUENT 12.0: Theory Guide.

Bahaj, A. S., Batten, W. M. J., & McCann, G. (2007). Experimental verifications of numerical predictions for the hydrodynamic performance of horizontal axis marine current turbines. *Renewable Energy, 32*(15), 2479-2490. doi: 10.1016/j.renene.2007.10.001

Bahaj, A. S., Molland, A. F., Chaplin, J. R., & Batten, W. M. J. (2007). Power and thrust measurements of marine current turbines under various hydrodynamic flow conditions in a cavitation tunnel and a towing tank. *Renewable Energy, 32*(3), 407-426. doi: 10.1016/j.renene.2006.01.012

Baltazar, J., & de Campos, J. A. C. F. (2008). *Hydrodynamic Abalysis of Horizontal Axis Marine Current Turbine with a Boundary Elemnet Method*. Paper presented at the 27th Int. Conf. on Offshore Mechanics and Arctic Eng., Estoril, Portugal.

Baltazar, J., & de Campos, J. A. C. F. (2009). *Unsteady analysis of a horizontal axis marine current turbine in yawed inflow conditions with a panel method*. Paper presented at the First International Symposium on Marine Propulsors, Trondheim, Norway.

Barnsley, M. J., & Wellicome, J. F. (1990). Final report on the 2nd phase of development and testing of a horizontal axis wind turbine test rig for the investigation of stall regulation aerodynamics: Carried out under ETSU Agreement E. 5A/CON5103/1746.

Batten, W. M. J., Bahaj, A. S., Molland, A. F., & Chaplin, J. R. (2008). The prediction of the hydrodynamic performance of marine current turbines. *Renewable Energy, 33*(5), 1085-1096. doi: 10.1016/j.renene.2007.05.043

Batten, W. M. J., Bahaj, A. S., Molland, A. F., Chaplin, J. R., & Sustainable Energy Res, G. (2007). Experimentally validated numerical method for the hydrodynamic design of horizontal axis tidal turbines. *Ocean Engineering, 34*(7), 1013-1020. doi: 10.1016/j.oceaneng.2006.04.008

Betz, A. (1920). Das Maximum der theoretisch möglichen Ausnu¨tzung des Windes durch Windmotoren. *Zeitschrift fu¨r das gesamte Turbinenwesen, 26*, 307-309.

Blunden, L. S., & Bahaj, A. S. (2007). Tidal energy resource assessment for tidal stream generators. *Proceedings of the Institution of Mechanical Engineers Part a-Journal of Power and Energy, 221*(A2), 137-146. doi: 10.1243/09576509jpe332

Breslin, J., Van Houten, R., Kerwin, J. E., & Johnsson, C.-A. (1982). *Theorecical and experimental propeller-induced hull pressures arising from intermittent blade cavitation, loading, and thickness*. Paper presented at the Trans. SNAME.

Burton, T., Sharpe, D., Jenkins, N., & Bossanyi, E. (2001). *Wind energy: handbook*: John Wiley and Sons.

Clarke, J. A., Connor, G., Grant, A. D., Johnstone, C., & Ordonez-Sanchez, S. (2008, 19-25 July). *Contra-rotating marine current turbines: Performance in field trials and power train developments*. Paper presented at the the 10th World Renewable Energy Congress, Glasgow.

Comstock, J. P. (1967). *Principles of naval architecture*: Society of Naval Architects and Marine Engineers.

Deng, Y. (2005). *Performance Database Interpolation and Constrained Nonlinear Optimization Applied to Propulsor Blade Design*. MS Thesis, The University of Texas at Austin, Austin, TX.

Epps, B. P., Stanway, M. J., & Kimball, R. W. (2009). *OpenProp: An open-source Design Tool for Propellers and Turbines*. Paper presented at the Society of Naval Architects and Marine Engineers Propeller/Shafting '09 Symposium, Williamsburg, VA.

Fine, N. E. (1992). *Nonlinear Analysis of Cavitating Propellers in Nonuniform Flow*. PhD, Massachusetts Institute of Technology, Boston.

Fine, N. E., & Kinnas, S. A. (1993). A Boundary-Element Method for the Analysis of the Flow around 3-D Cavitating Hydrofoils. *Journal of Ship Research, 37*(3), 213-224.

Greeley, D. S., & Kerwin, J. E. (1982). *Numerical methods for propeller design and analysis in steady flow*. Paper presented at the Trans. SNAME.

Griffin, P. E. (1998). *Computational techniques for the analysis and design of cavitating propeller blades*. M.S., The University of Texas at Austin, Austin.

Griffin, P. E., & Kinnas, S. A. (1998). A design method for high-speed propulsor blades. *Journal of Fluids Engineering, 120*, 556-562.

He, L. (2010). *Numerical Simulation of Unsteady Rotor/Stator Interaction and Application to Propeller/Rudder Combination*. PhD, The University of Texas at Austin, Austin.

He, L., Chang, S., & Kinnas, S. A. (2010). MPUF-3A (Version 3.0) User's Manual: Ocean Engineering Group, The University of Texas at Austin.

He, L., & Kinnas, S. A. (2009). *A Method for the Prediction of Rotor/Stator Interaction-Applications to 2-D Hydrofoils and Propeller*. Paper presented at the Society of Naval Architects and Marine Engineers Propeller/Shafting '09 Symposium, Williamsburg, VA.

Kerwin, J. E. (2001). *Hydrofoils and Propellers (13.04 Lecture Notes)*: Massachusetts Institute of Technology.

Kerwin, J. E., Kinnas, S. A., Lee, J.-T., & Shih, W.-Z. (1987). *A surface panel method for the hydrodynamic analysis of ducted propellers*. Paper presented at the Transactions of Society of Naval Architects & Marine Engineers.

Kerwin, J. E., & Lee, C. S. (1978). *Prediction of Steady and Unsteady Marine Propeller Performance by Numerical Lifting-Surface Theory*. Paper presented at the Trans. SNAME.

Kinnas, S. A. (1991). Leading-edge corrections to the linear theory of partially cavitating hydrofoils. *Journal of ship research, 35(1)*, 15-27.

Kinnas, S. A. (1992). A General-Theory for the Coupling between Thickness and Loading for Wings and Propellers. [Article]. *Journal of Ship Research, 36*(1), 59-68.

Kinnas, S. A., Chang, S.-H., Yu, Y.-H., & He, L. (2009). *A Numerical Method for Predicting the Performance of Podded and Ducted Propellers*. Paper presented at the Society of Naval Architects and Marine Engineers Propeller/Shafting '09 Symposium, Williamsburg, VA.

Kinnas, S. A., & Fine, N. E. (1989). *Theoretical prediction of the midchord and face unsteady propeller sheet cavitation*. Paper presented at the Proceedings of the Fifth International Conference on Numerical Ship Hydrodynamics, Hiroshima, Japan.

Kinnas, S. A., & Fine, N. E. (1993). A Numerical Nonlinear-Analysis of the Flow around 2-Dimensional and 3-Dimensional Partially Cavitating Hydrofoils. [Article]. *Journal of Fluid Mechanics, 254*, 151-181.

Kinnas, S. A., Griffin, P. E., Choi, J. K., & Kosal, E. (1998). *Automated design of propulsor blades for high-speed ocean vehicle applications*. Paper presented at the Trans. SNAME.

Kinnas, S. A., & Hsin, C. Y. (1992). Boundary Element Method for the Analysis of the Unsteady-Flow around Extreme Propeller Geometries. [Article]. *Aiaa Journal, 30*(3), 688-696.

Kinnas, S. A., Lee, H. S., Gu, H., & Deng, Y. (2005). *Prediction of performance and design via optimization of ducted propellers subject to non-axisymmetric inflows*. Paper presented at the 2005 Society of Naval Architects and Marine Engineers Annual Meeting, Houston, TX.

Kinnas, S. A., & Pyo, S. (1999). Cavitating propeller analysis including the effects of wake alignment. [Article]. *Journal of Ship Research, 43*(1), 38-47.

Kudo, T., & Kinnas, S. A. (1995). *Application of vortex/source lattice method on supercavitating propellers*. Paper presented at the In 24th American Towing Tank Conference, College Station, TX.

Lee, C. S. (1979). *Prediction of Steady and Unsteady Performance of Marine Propellers with or without Cavitation by Numerical Lifting Surface Theory*. PhD Thesis, Massachusetts Institute of Technology.

Lee, H. S. (2002). *Modeling of Unsteady Wake Alignment and Developed Tip Vortex Cavitation*. PhD, The University of Texas at Austin, Austin.

Lee, H. S., & Kinnas, S. A. (2004). Application of a boundary element method in the prediction of unsteady blade sheet and developed tip vortex cavitation on marine propellers. [Article]. *Journal of Ship Research, 48*(1), 15-30.

Lee, H. S., & Kinnas, S. A. (2005a). A BEM for the modeling of unsteady propeller sheet cavitation inside of a cavitation tunnel. [Article]. *Computational Mechanics, 37*(1), 41-51.

Lee, H. S., & Kinnas, S. A. (2005b). Unsteady wake alignment for propellers in nonaxisymmetric flows. [Article]. *Journal of Ship Research, 49*(3), 176-190.

Lee, H. S., & Kinnas, S. A. (2006). *Prediction of cavitating performance of ducted propeller*. Paper presented at the The sixth International Symposium on Cavitation, Wageningen, The Netherlands.

Lee, J.-T. (1987). *A Potential Based Panel Method for The Analysis of Marine Propellers in Steady Flow*. PhD, Massachusetts Institute of Technology, Boston.

Mishima, S., & Kinnas, S. A. (1996). A numerical optimization technique applied to the design of two-dimensional cavitating hydrofoil sections. [Article]. *Journal of Ship Research, 40*(1), 28-38.

Mishima, S., & Kinnas, S. A. (1997). Application of a Numerical Optimization Technique to the Design of Cavitating Propellers In Nonuniform Flow. *Journal of ship research, 41*(2), 93-107.

Sun, H. (2008). *Performance Prediction of Cavitating Propulsors Using a Viscous/Inviscid Interaction Method*. PhD Thesis, The University of Texas at Austin, Austin, TX.

Sun, H., & Kinnas, S. A. (2008). *Performance prediction of cavitating waterjet propulsors using a viscous/inviscid interactive method*. Paper presented at the Proceedings, 2008 SNAME Annual Meeting and Ship Production Symposium, Houston, TX.

Wrench, J. W. (1957). The circulation of propeller induction factors: David Taylor Model Basin.

Xu, W. (2009). A study of producing the maximum efficiency for the wind turbine and propeller *Civil, Architectural, and Environmental Engineering*. Austin, TX: The University of Texas at Austin.

Young, Y. L., & Kinnas, S. A. (2003). Analysis of supercavitating and surface-piercing propeller flows via BEM. [Article]. *Computational Mechanics, 32*(4-6), 269-280.

Young, Y. L., Motley, M. R., & Yeung, R. W. (2010). Three-Dimensional Numerical Modeling of the Transient Fluid-Structural Interaction Response of Tidal Turbines. *Journal of Offshore Mechanics and Arctic Engineering-Transactions of the Asme, 132*(1). doi: 011101

10.1115/1.3160536

Yu, Y. H. (2008). *Prediction of Flows around Ship-shaped Hull Sections in Roll Using an Unsteady Navier-Stokes Solver*. PhD Thesis, The University of Texas at Austin, Austin, TX.

Yu, Y. H., & Kinnas, S. A. (2009). Roll Response of Various Hull Sectional Shapes Using a Navier-Stokes Solver. [Article]. *International Journal of Offshore and Polar Engineering, 19*(1), 46-51.

Zan, K. (2008). A study of optimum circulation distributions for wind turbines *Civil, Architectural, and Environmental Engineering*. Austin, TX: The University of Texas at Austin.

Vita

Wei Xu was born in Shaoxing, Zhejiang Province, China in 1986. He graduated from Shaoxing No.1 Middle School in 2004. He received his Bachelor degree in Civil Engineering in 2008 at Zhejiang University in China. Since 2008, he continued his Masters program study in the Civil Engineering of the University of Texas at Austin. In his master program, he is a research assistant supervised by Prof. Spyros A. Kinnas

Permanent address (or email): wei.xu.8502@gmail.com

This thesis was typed with word by the author.